Surface chemistry of ruthenium

Stefan van Vliet

Surface chemistry of ruthenium

ACADEMISCH PROEFSCHRIFT

ter verkrijging van de graad van doctor
aan de Universiteit van Amsterdam
op gezag van de Rector Magnificus
prof. dr. ir. P.P.C.C. Verbeek
ten overstaan van een door het College voor Promoties ingestelde commissie,
in het openbaar te verdedigen in de Agnietenkapel
op woensdag 30 april 2025, te 13.00 uur

door Stefan Willem Johannes van Vliet
geboren te De Ronde Venen

Promotiecommissie

Promotor:	prof. dr. P.C.M. Planken	Universiteit van Amsterdam
Copromotor:	dr. R. Bliem	Universiteit van Amsterdam
Overige leden:	dr. N.J. van Druten	Universiteit van Amsterdam
	dr. K.I.E. Olsson	Universiteit van Amsterdam
	prof. dr. A.M. Brouwer	Universiteit van Amsterdam
	prof. dr. M.D. Ackermann	University of Twente
	dr. D. Stradi	ASML

Faculteit der Natuurwetenschappen, Wiskunde en Informatica

List of publications

This thesis is based on the following publications:

<u>Chapter 3:</u>

"Identifying silicides via plasmon loss satellites in photoemission of the Ru-Si system"
S. van Vliet, A. Troglia, E. Olsson, R. Bliem
Applied Surface Science 608, 155139 (2023)
https://doi.org/10.1016/j.apsusc.2022.155139
S. van Vliet: Investigation, Visualization, Methodology, Writing – original draft.
A. Troglia: Investigation, Methodology.
E. Olsson: Investigation, Writing – review & editing.
R. Bliem: Supervision, Writing – original draft, Writing – review & editing, Project administration.

<u>Chapter 4:</u>

"The Role of Cation Vacancies in the Initial Oxidation of Ru(0001)"
Stefan van Vliet, Jonathon Cottom, Emilia Olsson, Jörg Meyer, and Roland Bliem
Under review
XPS experiment, measurements, and analysis, sample preparation hypothesis, discussions, writing, research

<u>Chapter 5:</u>

"Advanced oxidation of Ruthenium"
S. van Vliet, R. Bliem
in preparation
XPS experiment, measurements, and analysis, sample preparation, hypothesis, discussions, writing, research

The author has also contributed to the following publications:

"Assembling Palladium and Cuprous Oxide Nanoclusters into Single Quantum Dots for the Electrocatalytic Oxidation of Formaldehyde, Ethanol, and Glucose"
Jasper Biemolt, Dylan van Noordenne, Jianwen Liu, Elise Antonetti, Manon Leconte, **Stefan van Vliet**, Roland Bliem, Gadi Rothenberg, Xian-Zhu Fu, Ning Yan
ACS Applied Nano Materials 3 (10), 10176-10182 (2020)
https://doi.org/10.1021/acsanm.0c02162
Performed XPS measurements and provided expertise within this area

"Investigation of copper nanoscale electro-crystallization under directed and non-directed electrodeposition from dilute electrolytes"
Mark Aarts, **Stefan van Vliet**, Roland Bliem, Esther Alarcon-Llado
CrystEngComm 23 (20), 3648-3653 (2021)
https://doi.org/10.1039/D1CE00143D
SvV conducted the XPS measurements. XPS measurements were analysed by SvV and RB. All authors reviewed and commented on the manuscript.

"The influence of corrosion on diamond-like carbon topography and friction at the nanoscale"
Fiona M Elam, Feng-Chun Hsia, **Stefan van Vliet**, Roland Bliem, Liuquan Yang, Bart Weber, Steve E Franklin
Carbon 179, 590-599 (2021)
https://doi.org/10.1016/j.carbon.2021.04.068
Formal analysis, Investigation, Writing – review & editing.

"Free-standing nanolayers based on Ru silicide formation on Si (100)"
Alessandro Troglia, **Stefan Van Vliet**, Görsel Yetik, Ibrahim El Wakil, Jamo Momand, Bart J Kooi, Roland Bliem
Physical Review Materials 6 (4), 043402 (2022)
https://doi.org/10.1103/PhysRevMaterials.6.043402
XPS experiment, measurements, and analysis, discussions

"Extreme-Ultraviolet Excited Scintillation of Methylammonium Lead Bromide Perovskites"
Maarten LS Van Der Geest, Lucie McGovern, **Stefan Van Vliet**, Hanya Y Zwaan, Gianluca Grimaldi, Jeroen De Boer, Roland Bliem, Bruno Ehrler, Peter M Kraus
The Journal of Physical Chemistry C 126 (30), 12554-12562 (2022)
https://doi.org/10.1021/acs.jpcc.2c02400
XPS experiment, measurements, and analysis, proposing the oxidation hypothesis and discussions

"Ultrathin, sputter-deposited, amorphous alloy films of ruthenium and molybdenum"
Görsel Yetik, Alessandro Troglia, Saeedeh Farokhipoor, **Stefan van Vliet**, Jamo Momand, Bart J Kooi, Roland Bliem, Joost WM Frenken
Surface and Coatings Technology 445, 128729 (2022)
https://doi.org/10.1016/j.surfcoat.2022.128729
AFM Analysis, Writing – review & editing

"Intercrystallite boundaries dominate the electrochemical corrosion behavior of polycrystalline diamond"
Chen Xiao, Fiona Elam, **Stefan van Vliet**, Roland Bliem, Simon Lépinay, Noushine Shahidzadeh, Bart Weber, Steve Franklin
Carbon 200, 1-9 (2022)
https://doi.org/10.1016/j.carbon.2022.08.038
Formal analysis, Writing – original draft

"Electrochemically-stimulated nanoscale mechanochemical wear of silicon"
Chen Xiao, **Stefan van Vliet**, Roland Bliem, Bart Weber, Steve Franklin
Friction, 1-11 (2023)
https://doi.org/10.1007/s40544-023-0764-4
methodology, formal analysis, data curation, and writing—review & editing.

"Femtosecond laser induced emission of coherent terahertz pulses from ruthenium thin films"
Cruciani, Lorenzo; **van Vliet, Stefan**; Troglia, Alessandro; Bliem, Roland; van Druten, Klaasjan; Planken, Paul
J. Phys. Chem. C 2023, 127, 46, 22662–22672
https://doi.org/10.1021/acs.jpcc.3c05525
XPS experiment, measurements, and analysis, proposing the oxidation hypothesis and discussions

"Direct Laser Patterning of Ruthenium Below the Diffraction Limit"
Lorenzo Cruciani, Marnix Vreugdenhil, **Stefan van Vliet**, Dries van Oosten, Ester Abram, Roland Bliem, Klaasjan van Druten, and Paul Planken
Appl. Phys. Lett. 124, 171902 (2024)
https://doi.org/10.1063/5.0205538
Conceptualization (supporting), Investigation (supporting), Writing - review & editing (equal)

"Coverage-dependent stability of Ru_xSi_y on Ru(0001): a comparative DFT and XPS study"
Jonathon Cottom, **Stefan van Vliet**, Jörg Meyer, Roland Bliem, and Emilia Olsson
Phys. Chem. Chem. Phys., 2024, 26, 28793-28799
https://doi.org/10.1039/D4CP04069D
Formal analysis, Investigation, validation, visualization, writing - review & editing

Submitted/accepted articles:

Chapter 4
"The Role of Cation Vacancies in the Initial Oxidation of Ru(0001)"
Stefan van Vliet, Jonathon Cottom, Emilia Olsson, Jörg Meyer, and Roland Bliem
Under review
XPS experiment, measurements, and analysis, sample preparation hypothesis, discussions, writing, research

Anticipated publications:

"Comparing RuO_2 reduction by atomic and molecular hydrogen using in situ photoemission"
Ester Perez Penco, **Stefan van Vliet,** and Roland Bliem
in progress
Experimental design, discussions

"B-doped MCD electrochemically etching"
Chen Xiao, **Stefan van Vliet**, Roland Bliem, and Bart Weber
in progress
XPS experiment, measurements, and analysis, discussions

Abbreviations

AFM	Atomic Force Microscopy
BE	Binding Energy
CM	Cabrera-Mott
DFT	Density Functional Theory
DS-G	Doniach-Sunjic line shape convoluted with a Gaussian curve
EELS	Electron Energy Loss Spectroscopy
EUV	Extreme Ultraviolet
FWHM	Full-Width at Half Maximum
GI-XRD	Grazing Incidence X-ray Diffraction
IMFP	Inelastic Mean Free Path
LEED	Low-Energy Electron Diffraction
ML	Monolayer
NAP-XPS	Near-Ambient Pressure X-ray Photoelectron Spectroscopy
PLD	Pulsed Laser Deposition
RGA	Residual Gas Analyzer
STM	Scanning Tunneling Microscopy
UHV	Ultra-High Vacuum
XPS	X-ray Photoelectron Spectroscopy
XRD	X-ray Diffraction

Contents

1

Introduction

1.1 Introduction to this thesis

You are reading the results of four years of PhD work at ARCNL. The research described in this thesis has been inspired by the challenges of a semiconductor equipment manufacturer, ASML. ASML made the daring step to introduce around 2019 Extreme UltraViolet (EUV) lithography, using radiation with a wavelength of 13.5 nm to write nanometer sized features for the most advanced chips.

This thesis deals with challenges in the field of materials, or more precisely with the stability of materials under the harsh conditions of an EUV lithography tool. The tools used in this thesis have been developed over many years to study in detail the structure and composition of surfaces of materials. By designing careful experiments and by probing the surface composition, one can study reactions both wanted and unwanted, both expected but also unexpected. In this sense the work of this thesis contributes to the body of knowledge needed to design and produce lithography tools that perform according to specifications and that, ideally, do not show wear.

In the remainder of this chapter, I will focus on the nature of surface science and introduce the content of this thesis.

1.2 Surface Science within Natural Philosophy

Historically science started with the drive to understand the workings of nature. This activity and drive were baptized natural philosophy. Upon our increased understanding of nature, natural philosophy subdivided in multiple specializations, among which are physics and chemistry[1]. At the start of our formal education in high school and even at university, chemistry and physics are taught to be distinct and very different, whereas at an advanced stage, these specializations increasingly overlap, for example in the study of materials. Especially when scaling down to the interaction of atoms and molecules, the differences between chemistry and physics become less clear in labelling certain effects: is it physics or chemistry? Overlap of these disciplines is apparent at the surfaces of solids, where the coexistence of chemical reactions and physical concepts creates a mixture of the sciences.

The surface of such a solid is more than the terminating layer of a bulk material. The abrupt end of the solid and the resulting lack of bonding partners causes significant changes to the atomic and electronic structure of materials, and thus to their physics and chemistry. Moreover, at the surface, materials interact with their surroundings. The modification of the surface electronic structure has a direct effect on chemical reactions at surfaces and for the same reason also on the properties of interfaces between different materials. At the surface reactions occur with air, and its individual constituents, such as nitrogen, oxygen, carbon dioxide, and many more molecules, even if they are only present in small trace quantities. Furthermore, surface atoms may react or rearrange upon reactions. All these complexities make the study of surfaces and their interactions challenging. As the Nobel laureate Wolfgang Pauli famously proclaimed: "God made the bulk, but surfaces were invented by the devil". To understand how these surfaces are different from the bulk, one must resort to advanced experimental techniques[2]. Additionally these advanced techniques are sensitive to impurities on a surface which may complicate drawing firm conclusions. Surface experimentalists pursued techniques to work atomically clean and to prepare surface samples starting from a single crystal with a specific structure and orientation. By only allowing selected purified gasses one can study individual gas surface reactions. Hence, by controlling the gas composition above a well-defined surface, individual reactions can be described in detail. With
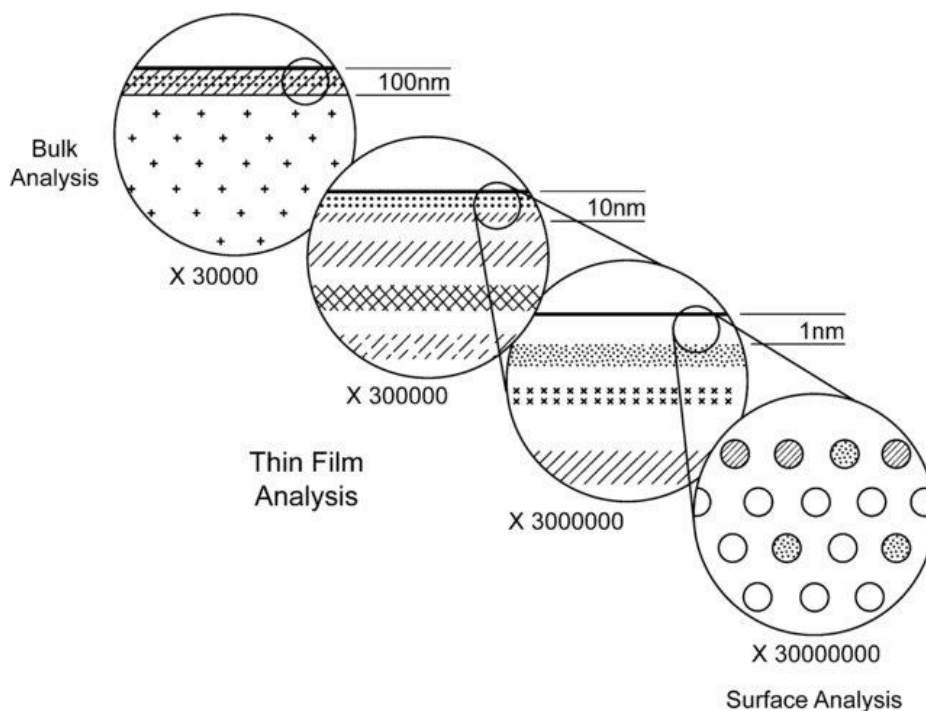

Figure 1-1 A depiction of the regimes of bulk, thin film, and surface analysis. Figure from reference. [2]

present-day technology pressures below 10^{-9} mbar can be achieved routinely, albeit with some effort and care by the experimentalist. At such a pressure, individual surface atoms do experience a gas phase collision about once every 15 minutes. In Table 1-1 the effect of different pressure on these collision rates is approximated.

Table 1-1 Approximated interaction at different pressure or vacuum; the time for a surface atom to interact with a gas atom, and the distance for a gas atom to interact with another gas atom.

	Surface atom – gas atom	Gas atom – gas atom
1 bar (1000 mbar) (ambient pressure)	1 000 000 000 per second	0.00008 mm
1 mbar	1 000 000 per second	0.08 mm
10^{-3} mbar	1000 per second	80 mm
10^{-6} mbar	1 per second	80 meter (larger than UHV chamber)
10^{-9} mbar	0.001 per second (once per 15 min)	80 000 meter (larger than UHV chamber)

As mentioned, EUV lithography provided the inspiration for many of the experiments performed in this thesis. Materials and their surfaces are challenged inside EUV lithography apparatuses due to the harsh conditions generated by EUV photons. The semiconductor roadmap demands continuous progress setting at each step new reference conditions for materials and surfaces. To sustain progress in lithography equipment, understanding of surface processes precedes steps to improve all applied materials.

Beyond understanding, control over surfaces and interface phenomena is also becoming important. Within lithography, computer chips are printed using light to produce the complex structures. Following the standard lithography equation ($CD=k_1\lambda/NA$, with CD being the critical dimension, λ the wavelength of light used, NA the numerical aperture of the lens seen from the wafer, and k_1 the coefficient that encapsulates how well a lithography apparatus approaches the limit of $k_1 = 0.25$), decreasing the wavelength used in lithography tools is an effective way to decrease this CD and hence the size of "makeable" device elements, such as transistors and conductive lines. With the move to the EUV wavelength (13.5 nm) more transistors became possible per computer chip, with currently about 10 billion (10^{10}) transistors in a single chip[3]. Also, the chemical reactions inside resist that are driven by EUV light

in comparison to previous generations of lithography are different[4]. Physical and chemical differences associated with the transition from previously used wavelengths of 365 nm, 248 nm, and 193 nm to 13.5 nm are numerous. Using EUV the photon energy became 91.8 eV. The interaction processes are fundamentally different. The earlier photon energies were not able to ionize most atoms or molecules, whereas 13.5 nm radiation can ionize everything. Figure 1-2 shows the efficiency of ionization by EUV, revealing a regular pattern and large differences in ionization efficiency, as expressed in the cross section[4,5]. These differences relate to the binding energies of the different electrons in each element. In the end, all elements absorb 13.5 nm, producing one or multiple electrons in the absorption step. As a consequence, the transition to 13.5 nm required radical changes in the lithography scanner. In particular, the strong interaction of EUV light with atoms and molecules makes vacuum a prerequisite for the whole tool.
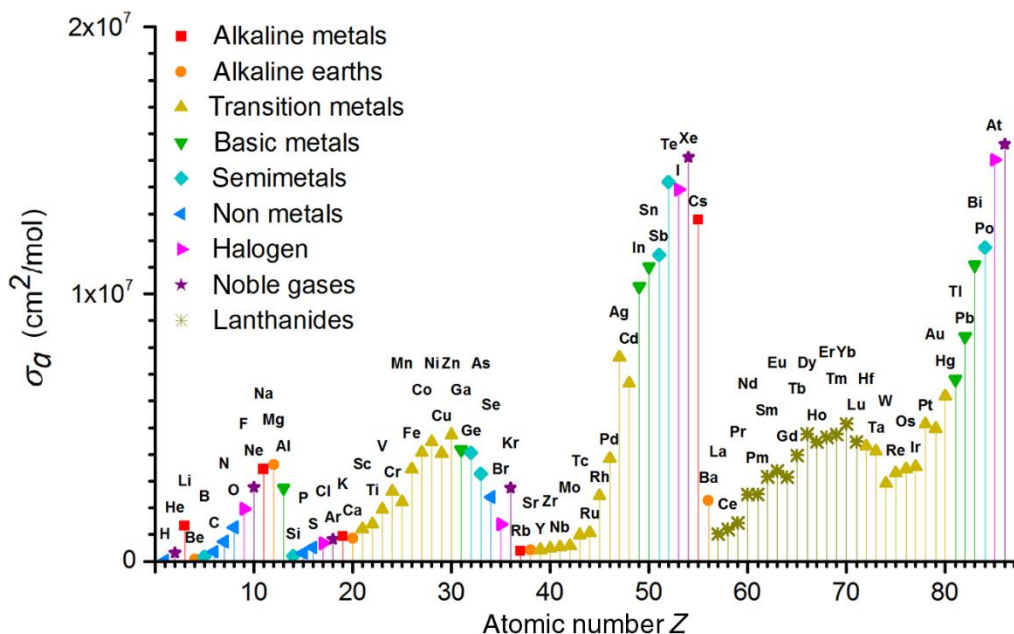
Figure 1-2 Atomic absorption cross section σ_a at EUV (λ =13.5 nm) of elements with atomic number Z from 1 to 86, plotted from tabulated data. Figure from reference.[4,5]

For a similar reason, using 13.5 nm photons in optical systems requires multilayer mirrors instead of lenses. Lenses are effectively opaque for 13.5 nm. The solution for mirrors involved very specifically designed thin layer structures, with approximately 6.5 nm thickness of double layers of a spacer (Si) and a metal (Mo) with ideally atomically sharp interfaces. The 13.5 nm radiation creates a standing wave pattern inside the mirror optimizing the reflection and minimizing the absorption. The multilayer mirrors used to guide and manipulate EUV light are an example of surface and interface properties optimized at the atomic scale[4,6]. In addition to low absorption, a high reflectivity requires a large difference in the index of refraction of the two used materials at this wavelength; molybdenum and silicon obey these conditions[6]. For a single bilayer, only a small fraction of the light is reflected. By using up to 70 of these bilayers, a reflection as large as 70% is achieved. Sharper interfaces will improve the reflection to the theoretical maximum of 74%, making it important to understand interface properties and how they affect sharpness and contrast[6].

1
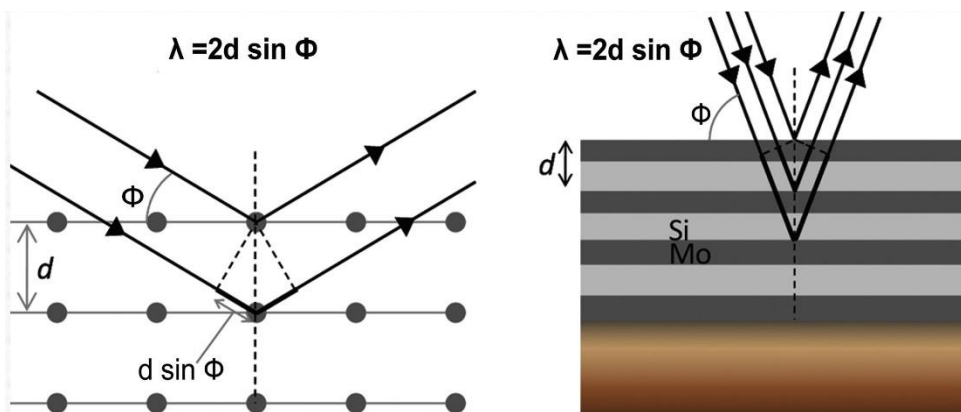
Figure 1-3 Schematic view of constructive interference from interfaces of a multilayer. Figure from reference.[6]

Even though these mirrors are situated in an as clean as possible vacuum, under EUV irradiation carbon can grow on these surfaces[7]. Carbon species are present in minute amounts in each vacuum system. Secondary electrons originating from the interaction of EUV irradiation with gaseous and surface atoms and molecules dissociate both hydrocarbons and water molecules[8]. The dissociated hydrocarbons result in carbon growth, decreasing the reflectivity of the mirrors. To counteract carbon growth a background gas of hydrogen is applied, transforming carbon atoms from the contamination into CH_4, a volatile carbon species that desorbs from the surface[9].
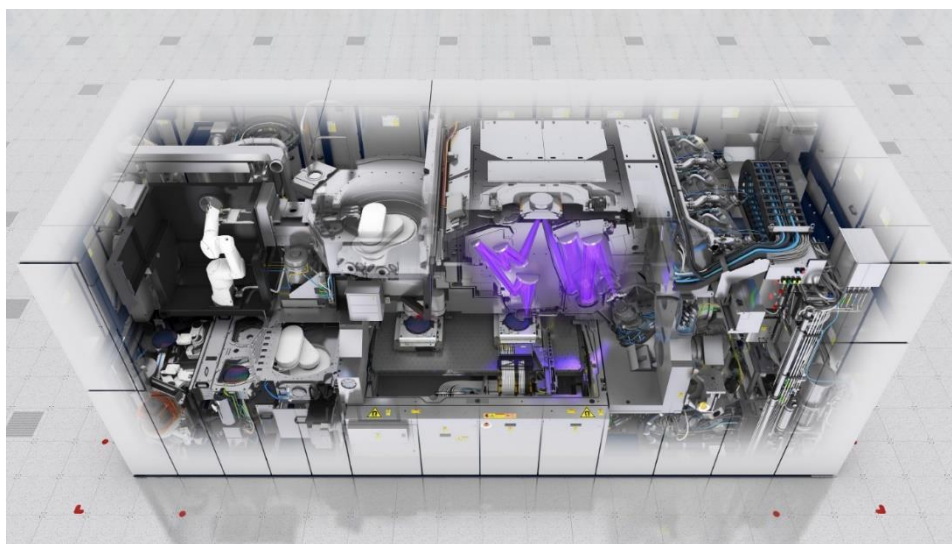
Figure 1-4 An overview of the EUV machine (Twinscan NXE:3400B) in operation, as seen from above. Image from ASML media library 2018.

The topmost layer of each EUV multilayer mirror experiences not only the highest intensity of EUV photons, but also represents the interface with the background gas. Understanding the individual interactions of the top layer with different gasses under these extreme conditions is important. Using advanced surface science techniques, questions concerning surface oxidation or other surface reactions can be answered. Beyond the field of lithography, insight in the properties of ruthenium can be extrapolated to catalysis[10–13], diffusion barriers[14], and others.

1.3   Oxidation of metals

Metals are essential parts of our modern-day lives. In their many uses, metals are exposed to widely different conditions ranging from vacuum and dry air to corrosive conditions. Understanding the oxidation of metals is essential for an application-specific material selection that helps extend the lifetime of metal components. The fundamental analysis of metal oxidation traces back to the early 1900s and it has been heavily studied for a broad range of applications[15–17].

In the following, the full process of oxide formation in metals will be discussed in steps. The different reaction steps and the form of the critical reagents will be described. The whole process is much more complex than a simple A + B → C reaction.

Figure 1-5 New metal screws, and old oxidized metal nails.

1.3.1   Thermodynamics and kinetics of oxidation reactions

The oxidation of metal can be predicted by combining thermodynamics and values on reaction energetics derived from either experiments or from theoretical calculations, with which the energetically most favorable state can be calculated. The Gibbs free energy is commonly used as thermodynamic potential in these calculations. With this the state of minimum energy can be calculated for each condition using the formation enthalpy, entropy, and temperature of the products[18,19]. If the final state has a smaller Gibbs energy than the initial state, the reaction is energetically favorable at the given conditions. When multiple different reaction outcomes are possible, the product(s) with the lowest Gibbs energy is

considered the energetically favored ground state. For a metal reacting with oxygen to form an oxide, the formula of the chemical balance is shown in equation 1-1. Most metals have different possible oxides. Theoretical calculations can predict the stability of each oxide at different temperatures and pressures.

$$xM + \frac{y}{2}O_2 \leftrightarrow M_xO_y$$

1-1

Where thermodynamics identifies the most energetically favorable state, kinetics determines how fast (and if at all) reactions proceed under a certain set of conditions. Kinetics is expressed in the form of a reaction rate, a combination of a rate constant, k, and the concentrations of the reactants, A and B, in first order with exponents n and m, as is shown in equation 1-2. The simple reaction of the type A + B → C follows a second order rate law, which is described by a parabolic curve as function of time if linear in both concentrations (n=m=1)[18]. For reactions with a potential barrier, the rate constant is described by the Arrhenius equation, shown in equation 1-3. In this formula, the Arrhenius constant A_r is the so-called pre-exponential factor, E_a is the activation energy of the reaction step, R is the gas constant, and T is the absolute temperature at which the reaction is taking place. The activation energy is sometimes called the effective activation barrier. Thermal fluctuations determine how frequently this barrier is overcome. Figure 1-6 shows an illustration of the characteristic energies involved in an oxidation reaction. The Gibbs free energy difference between products and reagents determines the favored final product, while the activation energy (E_a) is important for the reaction rate and thus determines the kinetics. If this energy barrier is too high to be overcome at the process conditions, the reaction, although thermodynamically favorable, is kinetically hindered and no products will form.

$$Rate = k[A]^n[B]^m$$

1-2

$$k = A_r e^{\frac{-E_a}{RT}}$$

1-3

Reactions intuitively accelerate by increasing the temperature. However, temperature can only tune the rate in such a simple way if a single reaction is considered[18]. As soon as two or more different reactions can occur, competition between these reactions complicates the temperature effect. Each of these reactions has its individual activation energy and Arrhenius constant. With different activation energies the ratio of products formed will depend on the temperature. If a reaction from the reactants towards a product is going via intermediate reactions in series, the slowest step will be rate-limiting.
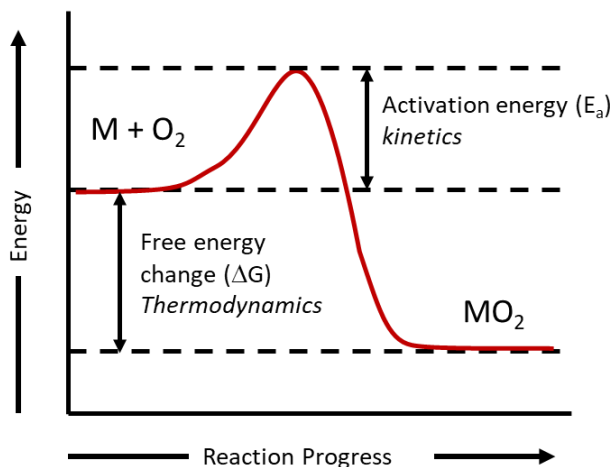
Figure 1-6 Illustrative sketch of thermodynamics and kinetics difference for a chemical reaction.

1.3.2   Elementary processes of oxidation

Oxidation reactions on surfaces are not fully described simply by a reaction equation involving a metal and oxygen molecules. Multiple overlapping steps can be distinguished from the initial state to the final oxide formed[17,20]. In Figure 1-7 the different steps for oxidation are schematically depicted. Firstly, the oxygen molecule impinges on the metal surface. The second step is the physical adsorption of the oxygen molecule on the metal surface. Thirdly, the oxygen molecule dissociatively chemisorbs on the metal surface, forming metal-oxygen atom bonds. The fourth step involves mobility of the oxygen atoms towards formation of a stoichiometric layer of oxide. This formation of an oxide, which is a phase change, is also referred to as nucleation. The fifth step is transporting oxygen or metal through the formed oxide layer to continue the chemical oxidation reaction, resulting in the growth of the oxide thickness.
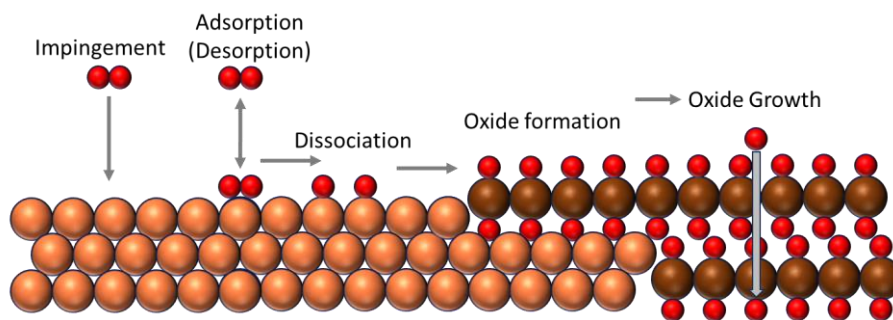
Figure 1-7 Schematic depiction of the steps in a simple model of metal oxidation.

Parameters such as temperature and pressure affect each step. For example, increasing the pressure will result in more collisions (impingement) of oxygen on the surface. As more oxygen impinges on the surface the adsorption and desorption balance can change based on the same reaction rate constants but multiplied by the changed concentration of oxygen in the gas phase and oxygen adsorbed on the surface. With an increase in oxygen adsorption, the probability of dissociation is, therefore, indirectly increased by the pressure. Temperature strongly affects the adsorption and desorption ratios; if oxygen desorbs at a high temperature, less atomic oxygen is available, limiting the formation of the oxide. However, the high temperature also enhances the rate of dissociation. Temperature can thus affect the oxide formation directly as it increases the specific reaction rate, but also indirectly by reducing the oxygen present on the surface for dissociation, decreasing the oxygen concentration available for the specific reaction.

Above we still treated the process as more or less homogenous. However in practice, it is more complex. First the dissociated oxygen reacts with the metal surface forming small oxide nuclei. The formation energetics of such oxide nuclei requires considering the sum of the surface free energy and the bulk free energy[21,22], similar to the description of crystallization of, for example, a homogeneous nanoparticle from the liquid phase. The crystallization of an oxide on a metal surface is influenced by additional parameters such as the mismatch of the lattices of the metal and the oxide. For a small oxide nucleus size the energy cost of forming a new boundary with undercoordinated atoms dominates, while with increasing radius of the nucleus the contribution of bulk free energy stabilizing the nucleus increases. At the so-called critical radius, the addition of an atom to the nucleus will lower its energy. Once this critical radius is exceeded, and the nucleus is stable and oxide formation can proceed[22,23]. When a nucleus remains below this critical size, the metal and oxygen are in a continuous process of forming and decomposing such nuclei without reaching the critical size, resulting in no oxide formation. We can conclude that a critical concentration of dissociated oxygen on the metal's surface is a prerequisite for oxide formation.

1.3 Oxidation of metals

As mentioned above, oxide formation requires mobility of the adsorbed oxygen atoms and/or of the metal atoms. This diffusion process must take place by oxygen atoms through the oxide to the metal buried below or by metal atoms through the oxide towards the surface[15,16,19,24]. Diffusion is described by Fick's first law, shown in equation 1-4, where j is the diffusion flux in concentration per time, D is the diffusion coefficient in area per time, $\frac{d\varphi}{dx}$ is the concentration gradient, φ the concentration of the diffusing species, and x is the spatial coordinate in this one-dimensional equation. The diffusion coefficient is dependent on several parameters with similarity to the earlier given Arrhenius equation. Equation 1-5 contains the pre-exponential coefficient D_0, the activation energy Q_d, the gas constant R, and the temperature T[17]. For diffusion to occur, the thermal energy has to allow an atom to overcome a periodic potential energy barrier. Equation 1-6 indicates the physical origin of the pre-exponential factor, where $2a$ is the distance between two potential minima for the diffusion to go between and v the attempt frequency[17,24,25]. In addition, the attempt frequency is affected by the size of the diffusing species, and by the interaction of charges, for example with an electric field. Extrinsic factors influencing the diffusion are oxide microstructure, defects, stoichiometry of the oxide, dissolution of oxygen and metal atoms inside the oxide or metal lattice, and temperature.

$$j = -D\frac{d\varphi}{dx} \tag{1-4}$$

$$D = D_0 e^{\left(\frac{-Q_d}{RT}\right)} \tag{1-5}$$

$$D_0 = 4a^2\,v \tag{1-6}$$

As an oxide is growing, the diffusion rate of oxygen atoms (or metal atoms) through the oxide changes. With the concentration on the surface maintained, as it depends on the dissociated oxygen, the concentration gradient decreases with increasing oxide thickness. In simple metal oxides, the diffusing species are either (partially) negatively charged oxygen ions or positively charged metal ions. From the many aspects that affect the diffusion of ions through the oxide, the size differences between metal ions and oxygen ions are considered dominant. In addition to the ion size, the structure of the oxide and the nature of the sites along the diffusion path are important for these diffusing ions. Besides the normal diffusion through the oxide structure, defects inside this structure can alter diffusion, either enhancing it or hindering it, for example by pinning atoms on the defect sites[24,26,27].

1.3.3 Reaction rate laws

Depending on the rate-limiting step and the state of the oxide, different rate laws describe the growth kinetics[28,29]. Figure 1-8 shows curve shapes representative of growth kinetics for different rate-laws. When oxygen adsorption is limiting, one observes a linear rate. When all adsorption sites are always occupied in the presence of high oxygen concentration, a so-called parabolic rate law is seen, which is rate limited by the ionic diffusion through the oxide, see equation *1-8*. A logarithmic growth rate is observed under conditions when the diffusion affected by a spatial electrical charge from electron tunneling through the oxide layer, see equation *1-9*[28]. And when the diffusion is dominated by the diffusion of ions by an electric field, it is described by an inverse logarithmic rate equation, see equation *1-10*.

Temperature strongly affects diffusion rates and is a stronger factor than adsorption and surface dissociation. As function of temperature one typically observes a transition from inverse logarithmic, via logarithmic, and parabolic to finally a linear rate law[28]. Each rate law has their corresponding rate-limiting step based on the characteristics of the metal and oxide.

Fast oxide growth is often described by the parabolic rate law, also known as Wagner's law[15], and is applicable for high temperatures and thicker overlayers; hundreds of nanometer to micrometers. The gradient in metal and oxygen concentration are the main drivers of the diffusion of metal and oxygen ions. As the diffusion of the ions is limiting, it can be modelled in an equation similar to Fick's first law, and the result is a parabolic growth rate[19]

For thin films and low temperatures, diffusion is slow, and internal electric fields affecting ion diffusion become increasingly important. In the very thin-film regime below 100 nm, quantum tunnelling effects become important as they start becoming an identifiable factor in these thin oxides. Cabrera and Mott[16] have introduced a model when the oxide growth is limited by ion diffusion controlled by an internal field. Their model was based on Wagner's model with the addition of an internal field applied through the oxide layer, resulting in a logarithmic or inverse logarithmic rate law[16].

$$X = k_l \cdot t \qquad \text{1-7}$$

$$X^2 = k_p \cdot t \qquad \text{1-8}$$

$$X = k_{log} \cdot \log(t) \qquad \text{1-9}$$

$$\frac{1}{X} = F - k_{inv} \cdot \log(t) \qquad \text{1-10}$$
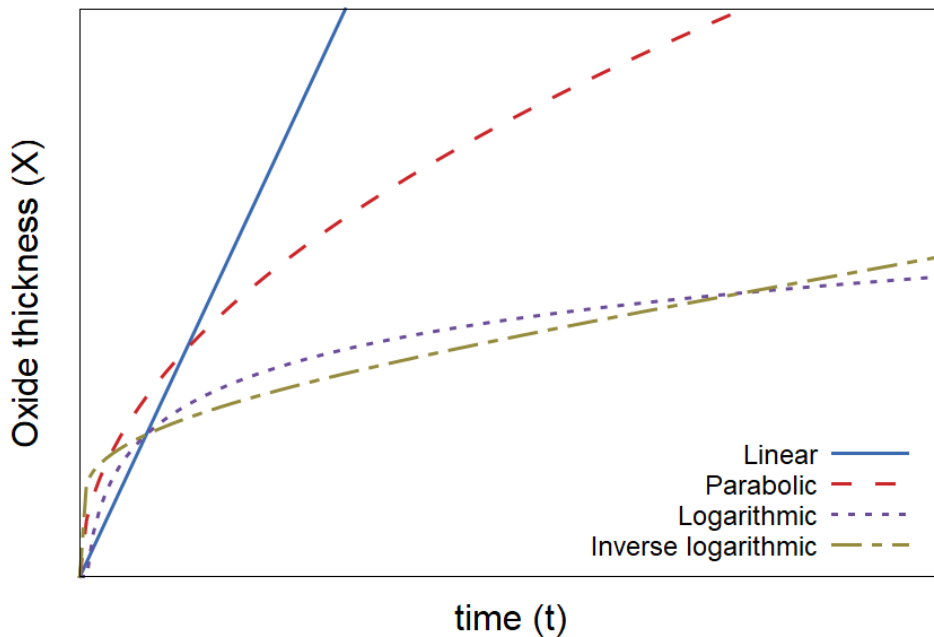
Figure 1-8 The four types of oxide growth kinetics, linear, parabolic, logarithmic, and inverse logarithmic are schematically presented in comparison to each other.

1.3.4 Metal oxidation model and the Mott potential

Mechanistic models on oxide growth are based on ions requiring the transfer of charge from the neutral metal to the neutral adsorbed oxygen molecule[30,31]. At low temperatures and thin layers, the internal fields can be the dominant force for ionic diffusion[17]. Below a thickness of 100 nm, the transfer of charges can also take place through insulating oxide layers. The potential difference between the interfaces on both sides of the oxide layer results in an electric field, this potential is named the Mott potential, V_m[16]. Ions experience an electric field between these two interfaces given by V_m/x, where x is the distance between the two interfaces[32]. When the oxide layer grows, the electric field decreases, slowing down growth. Ions created on the interfaces diffuse through the oxide via either vacancies or interstitial sites within the oxide lattice[16,17].
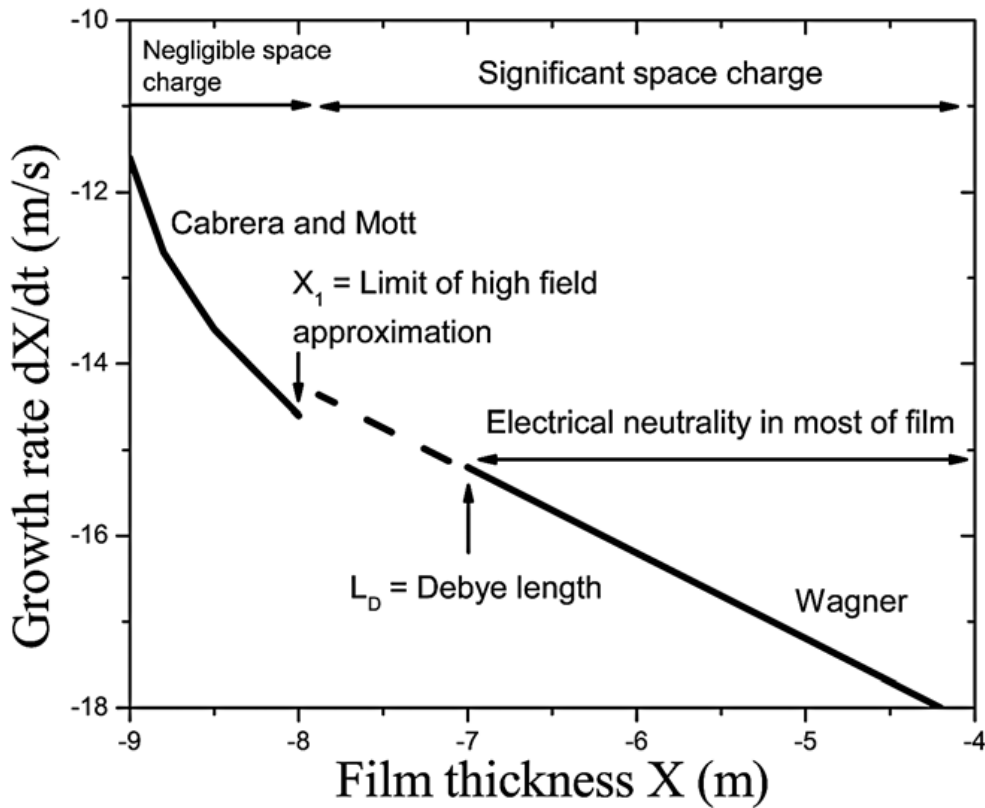
Figure 1-9 Logarithmic plot of growth rate of a hypothetical p-type oxide film as a function of its thickness, calculated using the theory of Cabrera and Mott when thin ($X < X_1$) and of Wagner when thick ($X > L_D$). Figure from reference.[30,31]

The concept of the Cabrera-Mott model (CM) is illustrated in a sketch in Figure 1-10. The electron at the metal Fermi level with a work function of Φ_0 tunnels through the oxide to an empty state of adsorbed oxygen with a work function of Φ_L. The electric field originates from the Mott potential, V_m, which is the difference between the work functions of the metal and the adsorbed oxygen, referred to as $\Delta\Phi$[16,17]. The Fermi level and the corresponding work function of both the metal and adsorbed oxygen are important to calculate the field generated. The oxide growth rate according to the CM model is shown in equation   1-11,   where x is   the thickness, t the time, Ω the volume of oxide formed per cation, n the number of cations per unit area, v the attempt frequency, W the rate limiting energy barrier, V_m the Mott potential, q the charge of the migrating cation, $2a$ the distance between two potential minima, k the Boltzmann constant, and T the temperature[16]. While the Mott potential is independent of the temperature, the CM model for oxide growth remains dependent on temperature due to the dissociation and diffusion processes[16,32].

1.3 Oxidation of metals
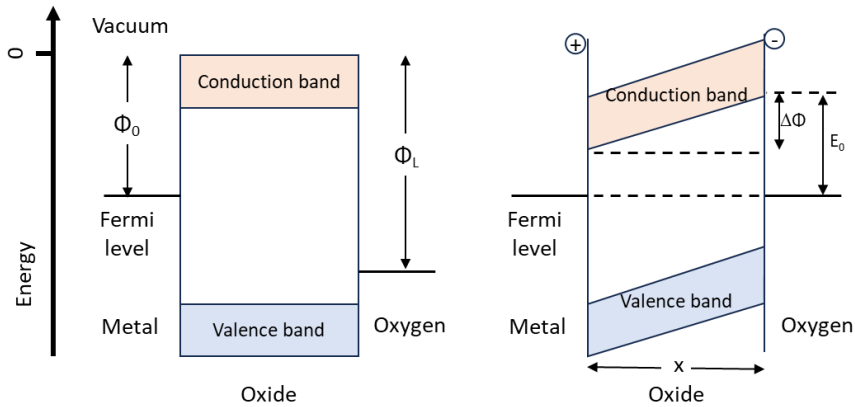
Figure 1-10 Schematic drawing of an energy-level diagram for metal oxidation following the Cabrera-Mott model. Left is before oxidation, right is during oxidation.

$$\frac{dx}{dt} = \Omega n v \, \exp\left(\frac{-W + qa\frac{Vm}{x(t)}}{kT}\right)$$

1-11

As diffusion of ions is affected by vacancies in the oxide and by interstitials, the abundance of defects at the experimental conditions impact diffusion and the resulting oxide growth[17]. While models like Wagner and CM are based on the formation of vacancies at both the interface between the metal and oxide, and between the oxide and the gas, other defects on the oxide/oxygen interface can result in additional dissociation, increasing the presence of active oxygen for the oxide growth[22,24,27]. Defects can also be a nucleation site for the initial oxide formation, impacting the start of oxide formation.

1.3.5 Surface dependent characteristics

From the description given in the previous paragraphs, it is evident that the surface is important for oxide growth. Dissociation probabilities of oxygen for example depend on the surface orientation, which is why dissociation differs between single-crystal, polycrystalline, and amorphous metal surfaces. Investigating the oxide growth on single crystals is a method to understand the oxidation routes in a controlled parameter set. Exploring the same element with different crystal orientations can give rise to different mechanisms and oxide growth rates. Facet-dependent oxidation studies have been performed for several metals, such as Cu[33,34], Al[35], Zr[36], Ni[37], Cr[37], Rh[38], W[39], and Pd[40]. While all of them show variations in oxide thickness between facets, there are common trends. Less densely packed surfaces, for example, often show a thicker final oxide thickness. On the close packed Al(111) and Cu(111) surfaces the oxide nucleation is limiting, while other crystal orientations of these metals do not display this limitation[33–35]. The differences between different crystal orientations can be attributed to a range of phenomena, including the structure of the chemisorbed oxygen layer, oxygen surface diffusion, surface energy, step edge density, and density of the metal and oxide. These trends indicate that diffusion plays an important role.
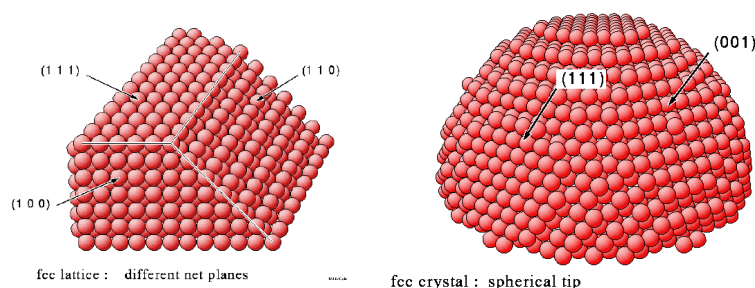
Figure 1-11 Left is a corner of a crystal shown with three orientations present. Right is a spherical tip shown with two orientations assigned. From the BALSAC picture gallery of Prof. K. Hermann, Fritz-Haber-Institut, Berlin.

Above, we collected arguments for single crystal oxidation. In practice, most materials are polycrystalline. Polycrystallinity adds orientation differences and interfaces. A polycrystalline surface often has a higher roughness. Each grain of a polycrystalline surface follows the oxidation of its respective crystal orientation[41]. Grain boundaries accelerate diffusion of oxygen at temperatures below the so-called Tammann temperature, roughly half the melting temperature[42]. Above this temperature the diffusion through bulk approaches the diffusion along grain boundaries.

1.3.6 Gas-phase dependent characteristics

Oxidation of surfaces is not restricted to exposure to oxygen gas. Other oxidizing environments exist. Atomic oxygen is even more reactive, and the combination of oxygen-containing species and electron beam exposure, exposure to plasma, and photon irradiation can enhance oxidation[43–45]. Exposure to atomic oxygen bypasses the dissociation of the molecular oxygen to atomic oxygen on the surface, increasing oxide growth[46]. Free electrons enhance the dissociation probability of oxygen, and surface charges may enhance ion diffusion through the oxide layer. The electron energy required to enhance the oxygen dissociation is approximately 5 eV, which matches the electron attachment of oxygen molecules to the surface[47]. In an oxygen plasma a combination of molecules, ions, atoms, and electrons are present and can interact with the surface. The electron induced dissociation of adsorbed oxygen and atomic oxygen dissociative attachment are identified as the predominant contribution for the oxide growth[48]. The facilitated dissociation can lead to kinetics that are typically seen in thermal oxidation at higher temperatures, as was observed for example for copper oxidation in oxygen plasma at room temperature[49].

Also other oxygen containing species can cause oxide growth. N_2O or NO_2 for example are considered even stronger oxidants than O_2, and hence resulting in a thicker oxide film[50]. H_2O can also act as oxidant, and is particularly relevant for electrochemistry[51], catalysis[52], and the EUV lithography industry. Dissociation of a water molecule on the surface results in OH^- and H^+, which can incorporate into an oxide layer as hydroxyls and protons[53]. In the case of beryllium, H_2O resulted in thicker final oxide, as well as a parabolic rate law for its oxide growth[54,55]. Water-induced oxidation may change the resulting oxide structure, showing a tendency towards more open oxide structures in the presence of water[56]. Clearly, water, which is a very persistent background gas in vacuum systems can be linked to a series of complex oxidation processes[57].

1.4   Oxidation of ruthenium

This thesis deals with surface reactions and predominantly with oxidation reactions on ruthenium. This element is a rare transition metal discovered in 1844 at Kazan State University and is placed in the periodic system in the platinum group. Ruthenium is present in small percentages of platinum ores, and once it is pure it is a shiny white colored metal. Ruthenium in the periodic system places it close to the noble elements, while maintaining reactivity with uncoupled electrons in its outer shell. In the following, selected literature on ruthenium and its oxidation is summarized.
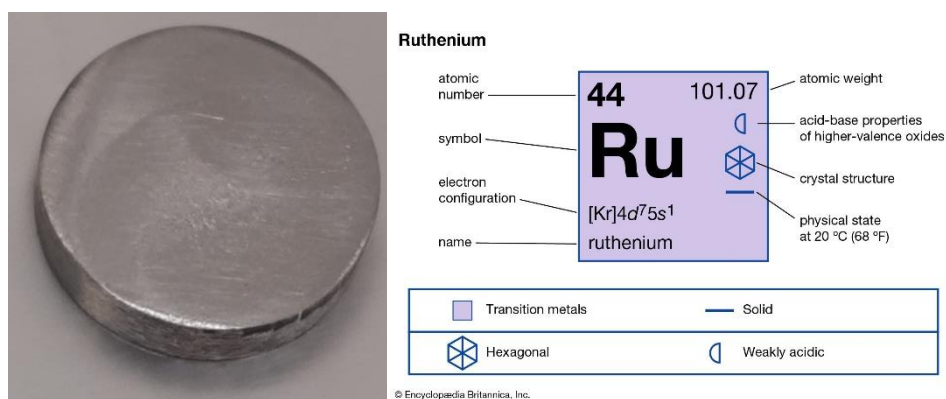
Figure 1-12 Left is a photo of a piece of ruthenium metal disk and right is an icon summarizing selected characteristics of the element ruthenium. The icon is from www.britannica.com.

Ruthenium has been studied for its resistance against oxidation. Due to the noble character of the ruthenium metal, it has been of interest for a broad range of applications. Thin ruthenium layers have been used as an oxidation barrier[3,58–64]. Apart from being an oxidation resistant barrier, ruthenium also functions as a diffusion barrier[14]. Furthermore ruthenium oxide is a catalyst for the oxygen evolution reaction, which generates molecular oxygen from water as reactant[65,66].

Exposing ruthenium to oxygen results in oxygen adsorbate structures which depend on the ruthenium crystal orientation and on the surface coverage with dissociated oxygen. After dissociation, chemisorbed oxygen atoms preferentially occupy the 3-fold hollow sites of the Ru(0001) hcp surface[65]. On Ru(0001), initially a (2 × 2) oxygen surface coverage is formed, followed by (2 × 1) and (1 × 1) superstructures for higher oxygen coverage[65,67–69]. At high coverage, both the sticking probability and

dissociation probability of added oxygen decreases. Different oxygen adsorbate structures are reported on less studied orientations of ruthenium, for example Ru(10$\bar{1}$0). Firstly, a c(2 × 4)-2O is formed, followed by a (2 × 1)p2mg-2O phase, similar to a (1 × 1) with a relaxation of a two atom repeat unit, corresponding to 0.5 and 1 monolayer of oxygen on the surface[70,71].

As described above, in many systems after a threshold concentration of atomic oxygen, nucleation of an oxide starts. However, no nucleation of the oxide on ruthenium terraces has been reported at low 10^{-6} mbar oxygen pressures[23,72] up to temperatures of 227°C. Above 307°C nucleation starts at double-step and multi-step edges of Ru(0001). And above 407°C nucleation on crystal terraces has been identified[73,74]. When a stable RuO_2 surface is formed, the further oxide growth is autocatalytic: oxide growth of RuO_2 accelerates after an initial layer of RuO_2 has been formed[72,75]. This observation is attributed to an enhancement of adsorption and dissociation of oxygen on the RuO_2 surface. The RuO_2 layer on Ru(0001) grows in the rutile structure and shows an orientational preference for the (110) plane at temperatures ranging from 277°C to 377°C[76–78]. At temperatures above 507°C, also the (100) and (101) RuO_2 crystal orientations have been observed[22]. The less commonly studied Ru(10$\bar{1}$0) surface predominantly grows RuO_2(100) at 327-387°C[79,80], but also RuO_2(111) and (101) have been reported to grow on Ru(10$\bar{1}$0)[80,81]. The changes in electronic structure and oxidation state with ruthenium oxidation are also clearly reflected in photoelectron spectra, showing changes in ruthenium core level energies[82–84] as well as the appearance of a characteristic satellite peak upon oxidation to rutile RuO_2[82,84,85].

Experimental and theoretical work of the initial oxidation of the Ru(0001) surface provides compelling evidence for the existence of an intermediate oxide phase between the metal and rutile oxide[76,86–90] which is converted to rutile RuO_2 at a critical thickness[22,91–93]. A scientific discussion about the existence and nature of this intermediate oxide has been going on for decades. Several different explanations and hypothesized structures have been reported. Due to the increased oxygen content without evidence of RuO_2, a subsurface oxygen phase was suggested by Böttcher *et al.* between 1999 and 2002[50,94,95]. In this model, the oxygen is dissolved in the ruthenium or between the first and second rows of ruthenium. Based on this model, Blume *et al.* proposed a transient surface oxide phase, also known as TSO[72,89,96,97]. This phase is neither ruthenium metal nor RuO_2 but a sub-stoichiometric ruthenium oxide phase. This phase has been reported in several publications from 2004 to 2007 by Blume and more recently by Cai *et al.* in 2015 in a DFT study[68]. A different proposed structure of this intermediate phase originates from DFT calculations from Reuter *et al.* in 2002, suggesting a trilayer structure of O-Ru-O[78,91,92]. This trilayer structure is proposed to form following a first layer of

oxygen on the surface, followed by a second layer underneath the ruthenium surface atoms, which retain an arrangement close to the original ruthenium metal surface. The oxygen atoms are binding to the ruthenium from the top and the bottom, forming an O-Ru-O layer, which is decoupled from the ruthenium layers underneath. Possible additional trilayers grown underneath the first one are weakly bound to each other. Similar structures were found in other platinum group elements[98–100]. This structure has been heavily discussed in the literature[89,91,95]. The caveat of the ruthenium trilayer model, however, is that conclusive structural evidence could neither be obtained with diffraction techniques such as surface X-ray diffraction[76], LEED[86] nor with real-space methods such as low-energy electron microscopy[74,88,94] and scanning tunneling microscopy[23,60,74,75,81,101,102]. While these studies report details on the transition from a flat Ru(0001) layer to RuO_2(110) via a nanostructured phase[87] and a coexistence of different facets at different conditions[86], the details of the transition and the intermediate phase remain elusive[22,23,73,74,76,103]. This intermediate oxide grows via a modified pathway, where first a finite layer is grown, the intermediate oxide, followed by the nucleation of the final oxide phase and the oxide growth of this final oxide. However, how this intermediate is involved in the further oxidation is still not well understood.
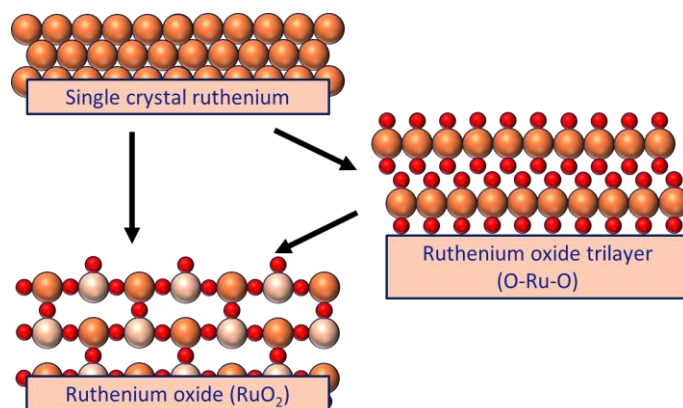
Figure 1-13 Schematic figure on the ruthenium oxidation towards the rutile oxide (RuO_2) and the alternative oxidation pathway via an intermediate oxide phase such as the proposed trilayer oxide.

Oxidation studies of ruthenium involved both single crystal and polycrystalline surfaces. For single crystal oxidation, specifically the Ru(0001) in the temperature range from 277 to 357°C with O_2 pressures above 10^{-5} mbar, a self-limited oxide thickness of 1.6 nm RuO_2 is grown[76,83,102]. Similarly, a 2.6 nm oxide grown at 350°C[103] and a 3.0 nm layer at 400°C were reported[104]. Other publications have investigated single crystal oxide growth reporting RuO_2 presence as well, but they stated having

similar thicknesses without explicitly reporting oxide thickness values[23,89,93]. The oxide growth on polycrystalline ruthenium is more complex due to the presence of grain boundaries and the coexistence of different crystal orientations. At low temperatures, oxide thicknesses have been grown to 1.0 nm at 150°C and 2.5 nm at 200°C[46]. A different report, on the other hand, mentions that no oxide growth has been identified below 227°C[59]. For higher temperatures, the reported thicknesses range from 2.5 nm at 450°C, 6 nm at 500°C, 11 nm at 550°C, to 17 nm at 600°C, showing significantly increased oxide thicknesses in comparison to single crystal expectations[105]. Based on the variety of influence factors on different polycrystalline ruthenium surfaces, the difference between scientific papers is challenging to quantify. However, the oxide thickness has been consistently reported to be higher for polycrystalline ruthenium films with respect to single-crystal ruthenium films.

The oxidation of ruthenium has also been investigated beyond thermally driven oxidation by molecular oxygen. Using atomic oxygen, adsorption happens at room temperature, compared to a reported onset of oxygen dissociation at 227°C[101]. Scanning tunneling microscopy shows the formation of oxide nuclei at step edges, whereas growth with molecular oxygen was found to occur at double or multi-step edges[73]. The final oxide thickness increased with exposure switching from molecular oxygen to atomic oxygen at the same conditions, from 2.5 nm to 3.0 nm at 200°C and 1.0 nm to 1.5 nm at 150°C[46]. Acceleration of the oxide growth was further reported using irradiation by an e-beam of 1 keV, and photons of 40.8 eV. However, these circumstances did not affect the final oxide thickness, contrary to what was seen with atomic oxygen exposure[104]. With a different ionizing radiation source, with a photon energy of 92 eV, the oxidation of a ruthenium surface is complex as well. A ruthenium layer exposed to 10^{-9} mbar water vapor and 92 eV photons showed an oxide layer between 1.0 and 1.5 nm in the exposed area, and only a 0.5 nm oxide layer outside the photon exposure area[58,71].

1.5 Outline of this thesis

In this thesis, the surface chemistry of ruthenium is investigated with a focus on the interaction with oxygen, water, and silicon applying *in situ* X-ray photoelectron spectroscopy, supported by electron diffraction and scanning probe microscopy.

The main surface characterization method used in this thesis, X-ray photoelectron spectroscopy, is presented in CHAPTER 2. First, the fundamentals of X-ray Photoelectron Spectroscopy (XPS) are explained, followed by the technological transition to near-ambient pressure XPS (NAP-XPS) for experiments at higher pressures. The NAP-XPS system at ARCNL can measure during gas exposures at pressures up to the mbar range. Figure 2-5 on page 36 shows an illustrative example of the high-resolution XPS spectra revealing not only atomic species but also their chemical surroundings.

The first case study focuses on the surface chemistry of combining the two elements ruthenium and silicon. Samples containing these two elements can be imagined as layered structures of ruthenium and silicon, separate patches of the elements, or as their compounds, ruthenium silicides. This difference is of great importance for the surface and material properties. The differentiation between the individual elements and the silicide phase is, however, notoriously difficult using XPS. In CHAPTER 3 the characteristic energy shift of plasmon loss features within XPS spectra is used to differentiate between elemental silicon on ruthenium and ruthenium silicide. The chemical sensitivity of the electron-energy loss causing these plasmon loss features allows using XPS to distinguish between growth models involving silicon on ruthenium. Figure 3-3 on page 48 shows a detailed view of the spectral feature which is established as fingerprint to distinguish ruthenium silicide from ruthenium metal in this work.

In CHAPTER 4, the initial oxidation step of ruthenium is investigated using a combination of experimental and computational techniques. During iterative NAP-XPS measurements, pristine single-crystal ruthenium surfaces were exposed to oxygen at elevated temperature, revealing a two-step oxidation mechanism. This is in line with literature reporting that before the thermodynamically stable ruthenium oxide grows at the surface, ruthenium first forms a thin intermediate oxide phase. The combination of experimental results with density functional theory (DFT) calculations leads to the conclusion that vacancies in the surface of this initial ruthenium oxide layer play an important role in the growth of the oxide. Upon reaching a certain thickness of approximately two layers, the intermediate oxide is hindered in growth. When a sufficient density of ruthenium vacancies on the surface is present, however, acceleration of the ruthenium oxide growth and formation of

the stable ruthenium dioxide phase is witnessed. In Figure 4-2 on page 60 the oxidation curve showing the kinetic hindrance followed by accelerated growth is reproduced.

Continuing the study on ruthenium, less commonly studied aspects of ruthenium XPS spectra and its surface chemistry are presented in CHAPTER 5. First, the role of the measurement range and additional spectral features for the correct determination of the peak shape and intensity is discussed, followed by a sub-chapter on the oxidation of polycrystalline ruthenium and its comparison to single-crystal ruthenium. In the final sub-chapter, the exposure of clean ruthenium and different thicknesses of ruthenium oxide to water is presented to explore the different surface chemistry induced by the presence of this oxidant. For the pre-oxidized samples we identify differences in stability depending on the oxide thickness in the presence of water. Figure 5-6 on page 89 shows the comparison between the oxide growth of polycrystalline and single crystalline ruthenium. The stability of a thin oxide exposed to water vapor is shown in Figure 5-11 on page 97.

1

2
Methods

The properties of surfaces differ from those of bulk materials in several respects and are defined by the crystal orientation, atomic arrangement, and local composition of the outermost layers[106]. The characterization of structure, stoichiometry, and electronic properties of surfaces requires specific surface-sensitive techniques, making use of local probes or particles with limited probing depths. Within this thesis, a broad range of analytical techniques are used, such as X-ray Photoelectron Spectroscopy (XPS), Atomic Force Microscopy (AFM), Low Energy Electron Diffraction (LEED), Residual Gas Analysis (RGA), and X-ray Diffraction (XRD). Moreover, several synthesis, surface preparation, and exposure methods are employed, namely pulsed laser deposition (PLD), sputter deposition, annealing, and gas exposure. In this chapter, the core technique of this thesis, XPS, will be elaborated on.

2.1   X-ray Photoelectron Spectroscopy

2

XPS is a technique to determine the chemical composition of surfaces. It is based on the photoelectric effect, first observed by Heinrich Hertz in 1887 and explained by Albert Einstein in 1905: A photon of sufficient energy ($h\nu$) excites a core electron to overcome the binding energy of the electron (E_b) and the work function of the surface (Φ). The remaining energy is carried by the photoelectron as kinetic energy (E_{kin}), shown below in Formula *2-1*[107,108].

$$E_{kin} = h\nu - E_b - \Phi \qquad\qquad \text{\textit{2-1}}$$

Figure 2-1 sketches the photoionization process by a photon of 1486.6 eV exciting a 1s electron, resulting in a photoelectron. The corresponding binding energy is characteristic of the photoionized orbital, allowing to determine which element the photoelectron originated from based on its kinetic energy.

Another effect that can occur in parallel to the photoelectric effect is the Auger process. On the right side of Figure 2-1 the Auger process is sketched. The starting point of an Auger transition is an atom with a hole in a core shell, independent of how it is created. An electron from a higher orbital fills the core-hole, freeing a large amount of energy. This energy is transferred to another electron in a less strongly bound orbital, which is emitted with a characteristic energy. The energy of the Auger electron is independent of the energy of the excitation source contrary to the case of photoelectrons[109,110].
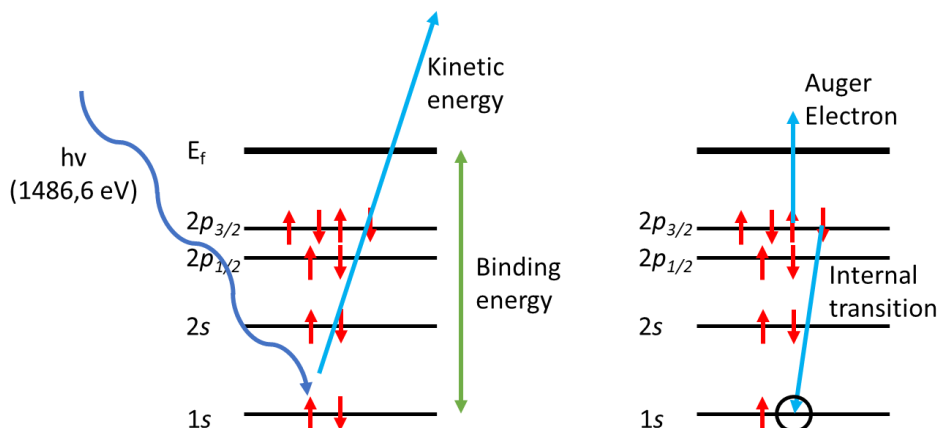
Figure 2-1 Schematic depiction of a photoelectron emission by X-ray excitation and Auger process.

The ability to measure these photoelectrons from samples requires a combination of complex instruments. The basic components of an XPS instrument are a light source, an electron energy analyzer, and an electron detector[107,109]. The light source for a laboratory XPS system is commonly an X-ray tube using the characteristic radiation of high-purity anode materials such as Al, Mg, or Cr. For the experiments in this thesis, Al Kα radiation with an energy of 1486.6 eV is used. For the analysis of the electron energy, an electrostatic analyzer, most commonly in hemispherical geometry is used. The electrons entering the analyzer are first focused and then accelerated or decelerated before entering the hemispherical analyzer, as illustrated in Figure 2-2[111]. An electrostatic field between the inner and outer hemisphere deflects the photoelectrons. Only electrons of a specific energy, also known as the pass energy, are transmitted to the detector. The photoelectrons arriving at the detector go through an electron multiplier, such as a microchannel plate (MCP). As the avalanche of electrons hits a phosphor screen, a light flash is detected by a CCD camera. From this CCD camera the intensity of the photoelectrons from the kinetic energy transmitted by the analyzer is collected[110].
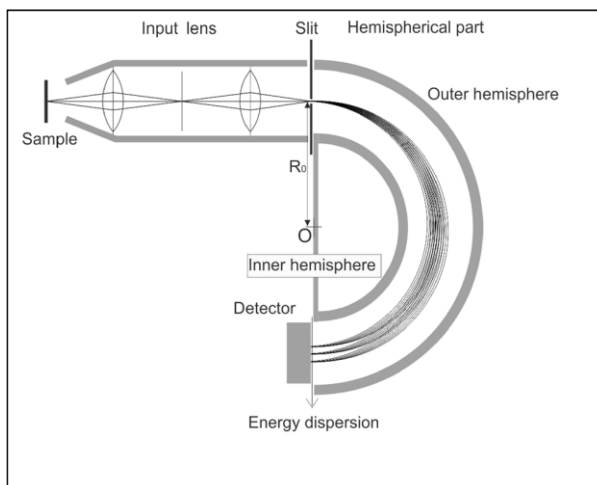
Figure 2-2 Schematic of an electrostatic analyzer, taken form Matsuda et al.[111]

The measured intensity of electrons as a function of different kinetic energy corresponds to an XPS spectrum. Typically the kinetic energy axis is converted to binding energy in XPS spectra. In Figure 2-3 a survey spectrum of an oxidized ruthenium single crystal is shown. Note that the BE axis is going from high to low, corresponding to an increase in the measured kinetic energy of the photoelectron. XPS spectra comprise of several characteristic features. The main features, the core-level photoelectron peaks occur at a characteristic binding energy for each element and orbital. In Figure 2-3, all peaks of the ruthenium and oxygen core level orbitals that can be excited with Al K radiation are identified. Besides the core-level photoelectron peaks, XPS survey spectra typically also contain Auger electron peaks, such as the oxygen KLL Auger peaks at approximately 980 eV and 1000 eV BE in Figure 2-3. Upon close inspection, also additional features such as satellite peaks and plasmon loss peaks can be identified at higher apparent binding energy (lower kinetic energy) than the main photoelectron peaks[109].

As the photoelectrons are generated, they travel through the solid phase before exiting at the surface to the vacuum. During this travel, the photoelectrons can scatter elastically and inelastically. While elastic scattering does not change their kinetic energy, inelastic scattering results in an energy loss. The inelastically scattered electrons no longer carry information on the emitting element, but can still be detected and contribute to the background intensity at lower kinetic energies. In the approximation of a homogeneous material, the probability of a photoelectron escaping from a certain depth without scattering follows the Beer-Lambert law, see
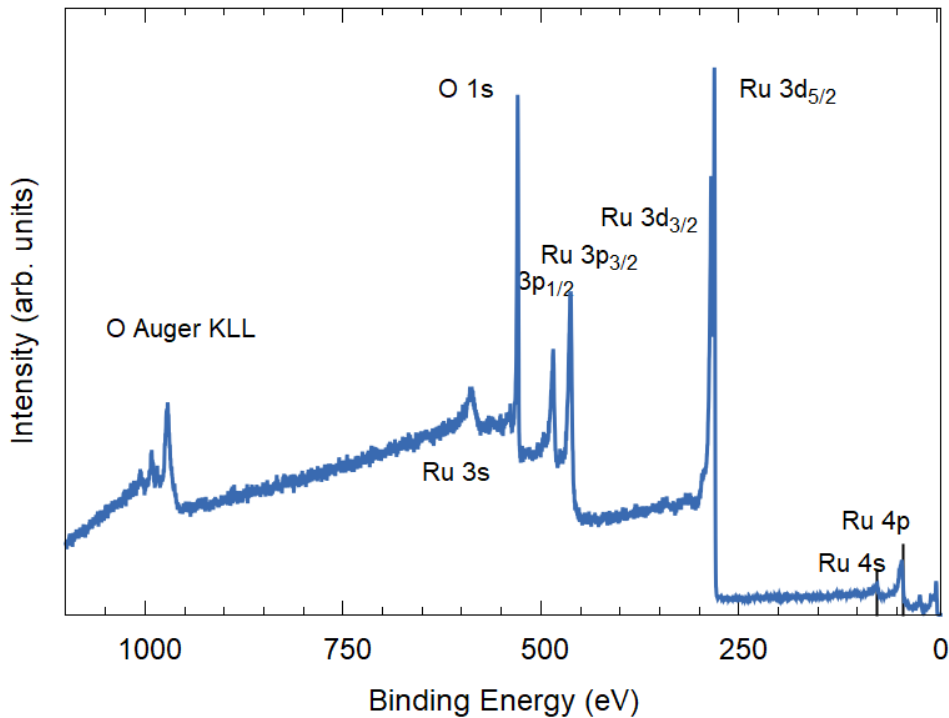
Figure 2-3 XPS Survey spectrum of an oxidized Ru(0001) single crystal

Formula 2-2. In this formula, the electron intensity is calculated by the exponential attenuation of the initial intensity I_0 of electrons generated at depth d, dependent on the inelastic mean free path (IMFP) λ of the photoelectron at a given kinetic energy and material[107]. The IMFP of electrons in solids shows a characteristic dependence on the kinetic energy, referred to as the "universal curve" based on its similar trend across a variety of materials, see Figure 2-4[112,113]. The material dependence of the IMFP can be approximated using the mass density, molecular weight, valence electron count, and the band gap[114]. Additionally, electrons emitted from a solid are attenuated by a gas phase, which further scatters electrons resulting in a decreased intensity[114].

$$I = I_0 exp\left(\frac{-d}{\lambda}\right)$$

2-2
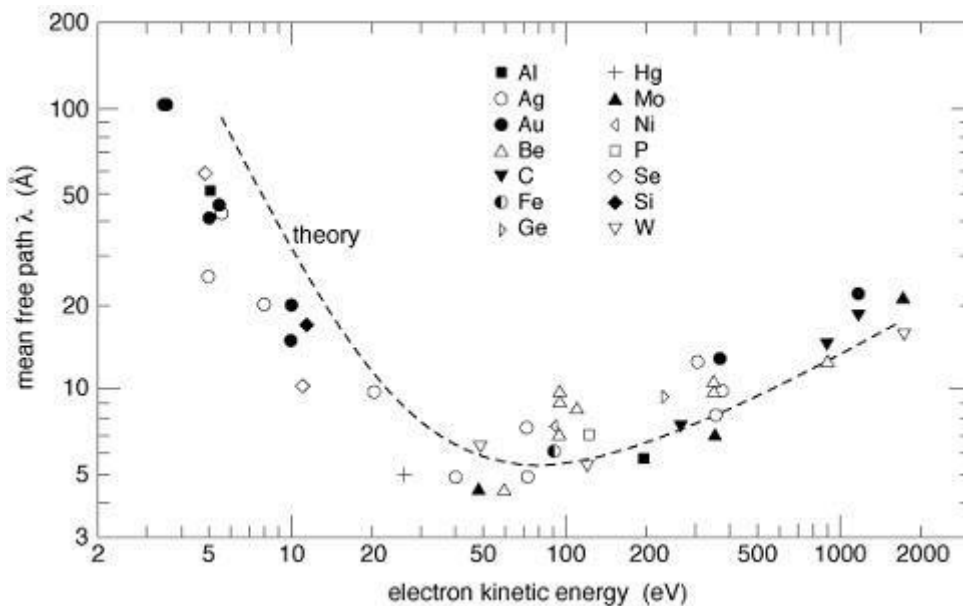
Figure 2-4 Electrons mean-free path universal curve in solids as a function of their energy, from Seah and Dench, graph made by Shokr.[112,113]

The intensity of photoelectrons in XPS depends on several factors, as is shown in Formula 2-3. Here, *I* is the intensity measured, *T* is the analyzer transmission function, D_e is the detector efficiency, *A* is the analyzed area, F_x is the flux of X-rays, $\Delta\Omega$ is the acceptance solid angle of the analyzer, *M* is the atomic density of the given element, λ is the IMFP of the analyzed photoelectrons, and $(d\sigma_x/d\Omega)$ is the differential photoionization cross section[109].

$$I = T\, D_e\, A\, F_x\, \Delta\Omega\, M\lambda\, (d\sigma_x/d\Omega) \qquad 2\text{-}3$$

Quantitative analysis of XPS spectra allows to determine atomic ratios between two elements in the surface region using the measured peak areas. The equation of the ratio of two elements is shown in Formula 2-4[109,115], where *n* is the atomic fraction,
I is the peak area, σ is the photoionization cross-section[116], λ is the IMFP of the photoelectron, and *T* is the detection efficiency. For most of the cases this equation can be simplified as the detector efficiency is the same when within analyzer specifications. If these factors are assumed to be equal, only the photoionization cross section and the probing depth need to be taken into account.

$$\frac{n_A}{n_B} = \frac{I_A/\sigma_A\lambda_A T_A}{I_B/\sigma_B\lambda_B T_B} = \frac{I_A/\sigma_A\lambda_A}{I_B/\sigma_B\lambda_B} \qquad \text{2-4}$$

The binding energy of the core-level electrons is dependent on their chemical environment. Changes in the electron binding energy can originate from different sources such as oxidation state, different molecular environments, and different lattice parameters. This effect is most commonly attributed to a change in screening of the positive charge of the nucleus by the valence electrons[117–119]. A lower valence electron density results in an increased electrostatic interaction of electrons with the nuclear potential and thus a higher binding energy. As example when a carbon atoms are oxidized, an increase of binding energy of the C 1s level is identified. When a carbon is bound to the more electronegative fluorine, further electron density is removed from the carbon, resulting in an even higher binding energy[117]. Other effects that can lead to core level shifts are surface charging, which adds potential that decelerates photoelectrons, and the Madelung constant, which can be considered as an electrostatic potential originating from the environment of the atom which can decrease the energy required to "eject" an electron from an orbital.

All orbitals, with the exception of s orbitals, appear as a doublet with two possible states at different binding energies[109]. This phenomenon is known as spin-orbit splitting. When considering the angular momentum quantum number L and the spin quantum number S=1/2, there are two possibilities of coupling them to obtain the total angular momentum J using J = |L + S| and J = |L − S|. For the s orbital, the only possible value of the total angular moment is 1/2, but for all other orbitals (L>0) two values are possible. For the p orbital, for example, J can be 3/2 and 1/2. The occupancy of electrons in the different split orbital is calculated by 2J+1, resulting in an occupancy ratio of the two spin-orbit split sub-orbitals of 2:1 for the p orbitals with J= 3/2 and 1/2. This ratio of orbital occupation also translates to the expected area ratio of the individual peaks of a spin-orbit split doublet peak.

Further characteristics of XPS peaks are their shape and line width, which is typically described using their full width at half-maximum (FWHM) after background subtraction. The line width and shape are defined by processes that can be divided into two categories, natural broadening and experimental broadening. The natural broadening of the XPS peaks originates from the finite core-hole lifetime, resulting in a Lorentzian broadening also known as the natural linewidth[120,121]. Besides the natural line width, also experimental factors lead to broadening, which is a convolution of several Gaussian shapes. The total broadening E_m is obtained by summing the squares of the individual contributions, as shown in Formula 2-5. The main points that are typically considered are broadening from the photon source, E_x, the natural energy distribution of electrons at that energy level, E_n, and the finite energy resolution of the analyzer, E_a[122].

$$E_m^2 = E_x^2 + E_n^2 + E_a^2 \qquad\qquad 2\text{-}5$$

From the literature the width of a monochromated Al Kα source line is reported as 0.25 eV[122]. The electrostatic analyzer contribution is dependent on several parameters. The finite energy resolution of an electrostatic analyzer is determined by the Formula   2-6. Where ΔE is the energy resolution, E_p is the pass energy of the electrons, d is the slit width, R_0 is the mean radius of the analyzer hemisphere, and α is the half angle of the electrons entering the analyzer. From this formula the effect of the different optimization options of an electron analyzer can be found, and how these scale with the broadening of the peak widths. With lower pass energy the intensity experimentally measured is decreasing. Optimal settings of the pass energy and slit setting can differ depending on the experiments[122].

$$\Delta E = E_p * \left(\frac{d}{2R_0} + \alpha^2 \right) \qquad\qquad 2\text{-}6$$

Moreover, the shape of the peak reflects the electronic structure of the sample, in particular whether a material is an insulator or metallic in nature. The peak shape of insulators and semiconductors is well described by the Voigt peak shape[123]. This Voigt peak shape is a convolution of a Cauchy-Lorentz distribution and a Gaussian distribution[124]. Materials with a metallic nature often require the use of asymmetric peak shapes, originating from the continuous distribution of electron energy losses that the photoelectron can undergo by exciting electrons close to the Fermi level. This asymmetric peak shape can be fitted using a Doniach-Sunjic line shape convoluted with a Gaussian curve (DS-G)[123,125].

In addition to peaks from photoelectrons and Auger electrons, features arising from discrete electron energy can also be identified in XPS spectra. The so-called satellite peaks are observed at lower kinetic energy than the photoelectrons and originate from a photoelectron losing energy by inducing an excitation in the material. Three common types of satellites are referred to as shake-up and shake-off features, as well as plasmon loss peaks. Shake-up satellites are generated when the outgoing electron interacts with a valence electron, exciting it to a higher energy level, often corresponding to an energy loss of a few eV. The shake-off satellite, on the other hand, is observed when a photoelectron excites a valence electron into the vacuum, reducing the initial photoelectron energy by a significant amount, more than the shake-up satellite. The shape and shift of these peaks can also be characteristic of the element, orbital, oxidation state, and chemical bonding environment. These satellites have for example been used to differentiate between different chemical environments of copper and iron, in cases where the main peaks were not suitable for characterization[126,127]. The third type, plasmon loss peaks are ascribed to the excitation of a collective oscillation of electrons present in the bulk or at the surface

of a solid, and these oscillations can be reasonably described for metals by a free electron gas model. As a photoelectron passes through a solid, it can excite these plasmon oscillations, losing a well-defined amount of kinetic energy in the process. The resulting plasmon loss peaks appear at higher binding energy in a range of 5 to 40 eV from the core level peak. Their peak shape is substantially broader than the associated core peaks[117,126,128].

2.2 Near-Ambient Pressure X-ray Photoelectron Spectroscopy (NAP-XPS)

A conventional XPS system is operated in a vacuum around 10^{-10} mbar. The study of surface processes and reactions involving elevated gas pressures is not possible during measurements (*in situ*). This limits a regular XPS system to an analysis before and after reactions and exposures; all information on processes occurring in between is lost. However, this limitation of XPS is technological rather than fundamental, and the development of advanced experimental equipment has enabled XPS to approach application conditions. To analyze surfaces at elevated pressures, two aspects of an XPS system need to be modified; the photon source and the electrostatic analyzer[129].

The mean free path of electrons in ambient environments is around 10^{-7} m. Even in the mbar range this mean free path remains at approximately 10^{-4} m, which is significantly shorter than the dimensions of the electron analyzers required to measure these electrons. Measurements are thus only possible if the pressure is kept low enough or the interaction distance of the electrons with high density of gas is minimized. With several differential pumping stages connected by small apertures, photoelectrons created under high pressure can still be collected on the detector. Electrostatic lenses can focus the photoelectron beam and allow for the use of several apertures starting close to the sample, where the measurement chamber is connected to the electron analyzer by a small opening in a conically shaped entrance piece[130]. Depending on the size of this pin-hole close to the sample different exposure pressures up to the range of tens of mbar can be achieved with minimal effect on the photoelectrons detected.

For the soft X-ray photon source, a different method of separating the two vacuum sub-systems has been developed. Between the photon source and the exposure chamber, vacuum sealing is provided by a thin membrane, which is partially transparent to soft X-rays but also mechanically stable and leak-tight. Silicon nitride is commonly used as material for this window.

2.2.1   XPS system at ARCNL

The XPS measurements in the present thesis were performed using a Scienta Omicron HiPP-3 spectrometer and an XM1200 monochromatic Al Kα source (1486.6 eV) separated by a SiN window from the measurement chamber. The HiPP-3 analyzer was used with a 0.8 mm aperture of the entrance cone and a slit setting of 1.0 mm.

On the NAP-XPS setup at ARCNL, gas exposure was performed via high-precision leak valves, allowing the exposure of a sample to a mixture of gasses during XPS measurement series. To increase the exposure range to high pressures beyond the operating range of the turbomolecular pump of the chamber, a gate valve with bypass construction were installed. The typical exposure range is from 10^{-9} mbar, up to 10^{-4} mbar, while with the bypass gate closed exposure pressure up to the mbar range can easily be achieved.

The gas composition of the exposures is essential and was measured by an residual gas analyzer, Extorr XT100M, which is installed on the first differential pumping stage of the system. From the combination of RGA with XPS, the gas composition and possible contaminants are linked to determine the effect of the exposures. The pressures of O_2, H_2, and H_2O measured by the RGA are calibrated against the pressures measured by the cold-cathode vacuum gauge in the XPS measurement chamber.

Sample heating was performed using a pyrolytic boron nitride heater filament for radiative heating of the back of the sample plate. The achievable temperature ranges from room temperature to 800°C. For temperature measurement, an N-type thermocouple is installed on the sample manipulator, and a pyrometer (Metis M311) in two color mode is used to determine the temperature of the sample surface.

The exposure gasses for this thesis are oxygen and water. The oxygen is dosed from a Messer CAN-Gas O_2 5.0 (Purity 99.999%). The water (EMSURE quality CAS:7732-18-5) was cleaned via several freeze-pump-thaw cycles.

2.3   XPS data analysis and peak fitting

With the system, typically four different types of XPS measurements are taken. Survey spectra, normal-resolution spectra for the quantification of element ratios, high-resolution spectra, and lastly time-resolved *in situ* spectra. The *in situ* spectra are measured in a sequence with alternating regions to identify the changes to different core level spectra as a function of exposure time. An overview of the standard parameters for XPS measurements is shown below.

Table 2-1 Standard XPS analyzer settings used in this thesis.

	Survey	Normal-resolution	High-resolution	*In situ*
Pass energy (eV)	500/300	300	100	100
Range (BE eV)	1150 to -5	~20	~20	~20
Step size (eV)	0.15	0.1	0.05	0.05
Acquisition time (ms)	59	235	235	59/118

The binding energy of the system was calibrated and the peak width measurements are performed to compare to literature peak fitting parameters. The standard peaks for binding energy calibration for all pass energies were Au $4f_{7/2}$ at 84.00 eV, and Ag $3d_{5/2}$ at 368.20 eV. The FWHM from Voigt peak shape for both Au $4f_{7/2}$ and Ag $3d_{5/2}$ have been measured to evaluate the Gaussian contribution of the different analyzer settings. The Au $4f_{7/2}$ was fitted using a fixed Lorentzian width of 0.33 eV, and Ag $3d_{5/2}$ was fitted with a Lorentzian width of 0.27 eV. With a pass energy of 100 eV, Au $4f_{7/2}$ has a Gaussian width of 0.54 eV, and Ag $3d_{5/2}$ of 0.56 eV. A broad range of slit settings and pass energies were cataloged, resulting in the optimized slit setting of 1.0 mm for the XPS measurements on this system.

The quantification of chemical species in XPS requires peak fitting. Multiple partially overlapping peaks can be present, requiring a deconvolution step, which is outlined here on the example of the Ru 3d region. For a reproducible and comparable fit, it is essential to apply constraints based on fundamental laws, literature, and reference samples. For the Ru 3d region, the spin-orbit split between Ru $3d_{5/2}$ and Ru $3d_{3/2}$ is kept constant, and the area ratio of these peaks is fixed to 1.5. The Gaussian width and asymmetry are constrained to be the same for both 5/2 and 3/2 peaks, while an increased Lorentzian width is allowed for the Ru $3d_{3/2}$ peak to account for Coster-Kronig broadening[131]. These parameters are optimized using a reference measurement of clean Ru(0001). Additional peaks were introduced upon partial and near complete oxidation of Ru(0001), using the same relative constraints between

their 5/2 and 3/2 peaks. The binding energy differences between metal and oxide peaks were optimized using multiple samples of different oxide thicknesses and constrained accordingly in all fits presented in this thesis. These constraints from detailed spectra are required to obtain comparable results in the time-dependent *in situ* spectra, which exhibit a markedly lower signal to noise ratio. An example of a fit is shown in Figure 2-5, with panel A displaying the Ru 3d region with individual fit components corresponding to ruthenium metal, ruthenium oxide, and the characteristic satellite of ruthenium dioxide with a rutile structure. In the O 1s XPS spectrum in panel B, the oxygen in the lattice and a second oxygen species, denoted as OH-Ru[82,84], are fitted. For Ru 3d metal and oxide as well as O 1s in the oxide DS-G peak shapes are used based on the metallic nature of Ru and RuO_2. For the Ru 3d satellite and OH-Ru species Voigt peak shapes are used.
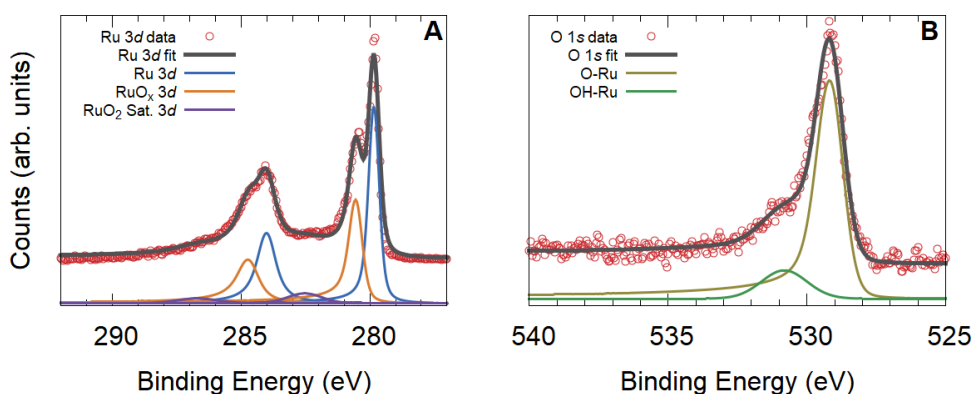

Figure 2-5 XPS of partially oxidized Ru(0001), (A) shows the Ru 3d spectrum with the species ruthenium metal, ruthenium oxide, and the ruthenium dioxide satellite, (B) shows the O 1s spectrum with the species of oxide lattice and hydroxide attached to ruthenium.

From the metal and oxide peaks in the Ru 3d region an approximate thickness of a Ru oxide overlayer on the metal substrate can be calculated. By assuming a homogeneous flat layer of oxide (species i) on top of the metal (species j), Equation *2-7* can be used to calculate the thickness *t* of such an overlayer. In this equation it accounts for IMFP, λ, emission angle, α, measured intensity, *I*, and atomic density, *M*. The superscript defines the material, with S for substrate and L for overlayer, and the subscript determines the photoelectron peak. In the present study of metal oxidation, ruthenium is defined as the substrate, S, and the ruthenium oxide as the overlayer, L. This equation allows for corrections for different probing depth based on different kinetic energy, different photoionization cross section, and the difference in density of the emitting layers. In Figure 2-6 on the left a schematic representation of the attenuation of photoelectrons created at different depths is shown. If the intensities of the metal and its oxide are measured as components of the same peak the kinetic energy of both photoelectron peaks is essentially the same

in this calculation. Thus, the Ru 3d photoelectrons generated in the metal and oxide have the same attenuation and photoionization cross section through the oxide overlayer. This allows simplification of the original formula and only use λ representing the IMFP through the oxide in the first part of equation *2-7*. In the center of Figure 2-6 the configuration of an overlayer on top of the substrate is displayed in the approximation of a homogeneous flat layer. Combining these two concepts illustrates the expected intensity measured by XPS for each of the different layers, shown on the right. Here the orange and blue areas represent the intensities measured for the overlayer and the substrate, respectively[132]. For this thesis the IMFP values of the different compounds are calculated using QUASES[133] as input for equation *2-7*. The experimental factors are determined to be λ·cos α = 2.226 nm for normal emission and $\frac{M^S \lambda_j^S}{M^L \lambda_i^L}$ = 1.675, with $M^{S,L}$, $\lambda_{i,j}^{S,L}$ corresponding to the atomic density of Ru in the substrate and the overlayer and the respective IMFP.

Figure 2-6 Schematic representation of the XPS overlayer determination: The left panel shows the decay of the measured intensity as a function of depth, the middle panel illustrates an overlayer of i on a bulk of j, and on the right their combination shows the signal arising from the overlayer in orange and the substrate in blue

$$t = \lambda \cos \alpha \ln \left(\frac{I_i^L}{I_j^S} \frac{M^S \lambda_j^S}{M^L \lambda_i^L} + 1 \right)$$

2-7

3

Identifying silicides via plasmon loss satellites in photoemission of the Ru-Si system

3.1   Abstract

The phase and composition of several transition metal silicides are challenging to identify with common surface analysis techniques such as X-ray photoelectron spectroscopy (XPS). While silicide formation is concomitant with a distinct change in electronic structure, only minute changes in the main spectral features are observed for example for the family of Ru silicides. Here, the authors combine XPS, grazing-incidence X-ray diffraction, and density functional theory calculations to demonstrate that the characteristic excitation energies of plasmons in Ru and its silicides are a sensitive and easily accessible descriptor that reflects the change in electronic structure upon the formation of specific silicides in XPS spectra. Electron energy loss satellites are reported to shift by more than 4 eV upon the formation of Ru silicide and by 1.7 eV between RuSi and Ru_2Si_3, making these changes accessible even for basic experimental equipment. In the context of literature on metal silicides and electron energy loss spectroscopy, this approach is considered promising as a general pathway to enhance the chemical sensitivity of surface spectroscopy methods.

3

3.2   Introduction

Semiconducting transition metal silicides have generated interest for potential use in optoelectronics, photovoltaics, and thermoelectrics [134,135]. In the family of ruthenium silicides, the two semiconducting compounds Ru_2Si_3 and RuSi have received most attention. Ru_2Si_3 is a direct gap material with reported band gaps between 0.44 eV and 1.08 eV [134,136,137], while the gap of the low-temperature phase of RuSi is smaller, ranging from 0.2 to 0.4 eV [138,139]. These narrow band gaps are of interest for infrared detectors[140], light-emitting diodes [141], and thermoelectric applications[142]. Moreover, Ru silicides are compatible with existing Si-based technology and are non-toxic.

Among the thermodynamically stable Ru silicides, RuSi and Ru_2Si_3 have been studied most extensively [143]. Upon deposition of Ru layers onto Si, Ru silicide has been observed to form spontaneously at the interface [144,145]. While the phase of this layer of a few unit cells is difficult to ascertain, the preferred phase of Ru_2Si_3 has been observed to form at the interface at 375°C. Annealing the Ru layers on Si at temperatures above 400°C results in further formation of Ru_2Si_3, and full conversion of the ruthenium layers is achieved at 625°C [146]. The formation of RuSi has been reported upon annealing mixtures below 475°C[146]. While the only experimentally confirmed structure of Ru_2Si_3 is orthorhombic (Pbcn) [147,148], two polymorphs have been observed for RuSi. The CsCl-type structure (Pm$\bar{3}$m, B2) forms at high temperature, whereas at low-temperature phase of RuSi assumes a FeSi-type structure (P2$_1$3, B20) [149,150]. Already small variations in composition have been reported to cause a strong structural preference for the CsCl-type structure in the case of Ru excess [138].

In the case of bulk silicide specimens or thick Ru-Si films, standard analysis tools such as simple X-ray diffraction are sufficient to confirm the formation of silicides and determine the predominant phase. A confirmation that thin Ru-Si films are converted to a silicide, on the other hand, is challenging with common surface

analysis techniques such as X-ray photoelectron spectroscopy (XPS). The characteristic XPS peaks, Ru 3d and Si 2p, show only subtle changes in peak position between the elemental materials and the silicides. Comparably small shifts are observed for other transition metal silicides,[151,152] making the determination whether a silicide is present challenging with XPS, in particular if no monochromatic X-ray source is available or different phases and contaminants such as oxygen or carbon are present. Challenges in application-oriented cases are expected for example for surfaces with oxide overlayers, layered structures of metal and Si, or Si surfaces with low admetal coverage. The reported difference between the Ru 3d XPS peak shapes of metal and silicide[144] is only of limited help without high-resolution spectra of high-purity samples.

Here, we demonstrate on the example of Ru silicides that plasmon loss peaks are well suited to identify selected compounds of different electronic structure but similar core level energies in XPS, inspired by reports of distinct differences between transition metals and their silicides in electron energy loss spectroscopy (EELS).[153,154] Upon annealing of a Ru layer on Si(100), as well as for Ru-Si multilayer stacks with compositions between RuSi and Ru_2Si_3, distinct shifts of the plasmon loss peaks by several electron volts are observed in *in situ* XPS measurements. The presence of RuSi and Ru_2Si_3 is confirmed via grazing-incidence X-ray diffraction (GI-XRD). We expect this approach to be relevant beyond the Ru-Si system, since the formation of transition metal silicides and other compounds generally affects the electron density of a metal, which is expected to change the plasmon loss energy.

3.3   Methods

Sample preparation: Ruthenium and silicon were deposited on Si(100) and Al$_2$O$_3$(0001) substrates by pulsed laser deposition (PLD) using a KrF excimer laser (Coherent Compex 201F, λ=248 nm) in 4.0x10^{-2} mbar Ar. The substrates were positioned 55 mm from the PLD-target. The depositions were performed at a laser fluence of 8.5 J/cm^2, a shot frequency of 10 Hz, and a spot size of 0.4 mm². For pure Ru and Si films on Si(100) with native oxide, 20000 deposition pulses were used ("Ru-Si(100)" and "Si-PLD", respectively). The mixed Ru-Si films were produced using 20 alternating double-layers of silicon and ruthenium deposited on Al$_2$O$_3$(0001) at 700°C. The number of deposition pulses was varied between 160, 210, and 320 for Si while it was kept constant at 600 for Ru, resulting in films of RuSi ("RuSi-PLD") and close to Ru$_2$Si$_3$ stoichiometry ("(Ru$_2$Si$_3$+RuSi)-PLD" and "(Ru$_2$Si$_3$+Si)-PLD"), respectively. The deposition of 1 nm of material requires 700 deposition pulses for ruthenium and 190 pulses for silicon. Annealing a 28nm Ru film at 550°C resulted in interdiffusion of Si to form a single Ru$_2$Si$_3$ silicide phase ("Ru$_2$Si$_3$-Si(100)")[146].

X-ray photoelectron spectroscopy: The XPS analysis was carried out with a HiPP-3 spectrometer using a monochromatic Al Kα source. The HiPP-3 analyzer is used with a 0.8 mm cone and a slit setting of 1.0 mm. XPS peak fitting is performed using KolXPD. The core level spectra were fitted using a Shirley background across the entire range shown in the figures and Voigt doublet peaks for all but the metallic Ru peak, for which a Doniach-Sunjic line shape convoluted with a Gaussian curve was employed. The plasmon loss energies were determined by fitting the loss features using Voigt doublets, restricting in the peak area ratios and peak split to be the same as in the respective core level. Atomic ratios were calculated using the peak area divided by the respective photoemission cross-section. Survey and Si 2p broad range spectra were measured at pass energy of 500 eV, Ru 3d broad range spectra at pass energy of 300 eV, and high-resolution spectra at pass energy of 100 eV. The peak positions of all samples grown on Al$_2$O$_3$(0001) have been corrected for small charge shifts using the Si 2p spectra of elemental Si and Ru$_2$Si$_3$ as reference. In the analysis,

probing depth effects due to different inelastic mean free paths of the Ru 3d and Si 2p photoelectrons were taken into account using the QUASES software package for the calculation of the inelastic electron mean free paths by the Tanuma Powell and Penn algorithm (TPP2M) [133] based on the materials parameters for Ru_2Si_3.

Grazing incidence X-ray diffraction: GI-XRD measurements were performed ex-situ using a Bruker D8 QUEST diffractometer system equipped with an Incoatec IµS 3.0 Cu Kα X-ray source (λ=1.5406 Å) and a PHOTON II Charge-integrating Pixel Array Detector (CPAD). The XRD patterns were acquired in grazing-incidence configuration to minimize the signal from the substrate. Powder diffraction diffractograms have been calculated using VESTA[155] for the phases existing in the temperature range according to the phase diagram: Si, $RuSi_2$, Ru_2Si_3, RuSi, Ru_4Si_3, and Ru. The diffractograms have been corrected for errors introduced by positioning using the peaks of the single-crystalline substrates Al_2O_3(0001) and Si(100) as reference. Small residual shifts between experimental and calculated diffraction peaks are ascribed to three-dimensional specimen displacement errors going beyond the z-correction that has been applied.

Density functional theory simulations: To obtain the theoretical loss function, the dielectric function was calculated from density functional theory (DFT) simulations performed in the GPAW code[156–158] following the methods outlined in references [159–163]. The energy cutoff and k-point mesh were after convergence tests set to 800 eV and a k-spacing of 0.07 Å^{-1}. For each phase (Si, RuSi, and Ru_2Si_3), the lowest energy structures were obtained from DFT cell optimization as implemented in the projector-augmented wave method (PAW) [156,164], with Perdew-Burke-Ernzerhof (PBE) functionals[165,166].

3.4 Results

The analysis of Ru silicide was performed on Ru-Si thin films prepared using two different approaches, based on annealing a Ru layer on Si(100) at 550°C and on the growth of multilayer stacks of alternating Si and Ru layers on Al_2O_3(0001) at 700°C. Figure 3-1 shows an overview of the GI-XRD diffractograms obtained on stacks of different composition ("RuSi-PLD", "(Ru_2Si_3+RuSi)-PLD", and "(Ru_2Si_3+Si)-PLD") and the annealed Ru layer on Si(100) ("Ru_2Si_3-Si(100)"). Diffraction signals from the Al_2O_3(0001) and Si(100) substrates are strongly suppressed at highly grazing X-ray incidence angles and hence not discernible in the data. For comparison, the calculated powder diffraction patterns of Si, Ru_2Si_3 (Pbcn), and RuSi (P2$_1$3), based on literature results[150,167,168], are shown. In agreement with literature[146], annealing of a Ru film on Si(100) was observed to result in phase-pure Ru_2Si_3, serving as reference sample for this silicide phase. Different stoichiometries were explored by depositing films of fixed Si/Ru ratios on Al_2O_3. In the case of the most Si-rich sample (Ru_2Si_3+Si)-PLD the presence of both the Ru_2Si_3 phase and elemental Si was identified. At a
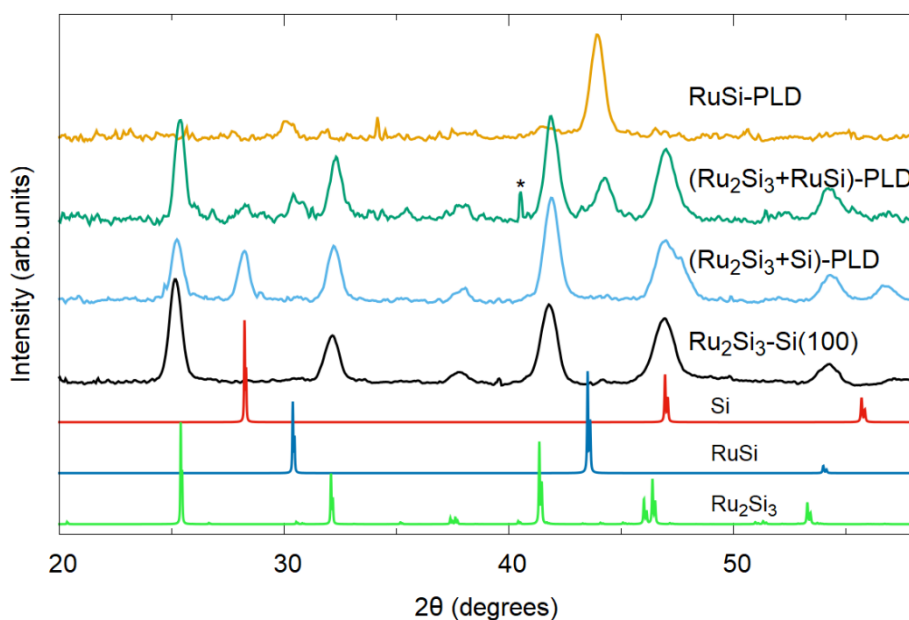

Figure 3-1 GI-XRD results of RuSi-PLD, (Ru2Si3+RuSi)-PLD, (Ru_2Si_3+Si)-PLD, and Ru_2Si_3-Si(100). Calculated powder diffraction patterns of Si, RuSi, and Ru_2Si_3. (*) artefact due to saturated pixels on the 2D detector.

decreased Si content ((Ru_2Si_3+RuSi)-PLD) the coexistence of Ru_2Si_3 and RuSi was observed. In the sample RuSi-PLD, a RuSi majority phase was observed to coexist with a small contribution from Ru_2Si_3.

The stoichiometry of the Ru and Ru silicide layers close to the surface was determined using XPS. The resulting ratios of Si/Ru are shown in Table 3-1. These values reflect the average composition in the surface region and were calculated assuming a homogeneous distribution of Ru and Si in the surface region. Variations in the probing depth due to different inelastic mean free paths of the Ru 3d and Si 2p photoelectrons were taken into account. Measurements at different probing depths indicate that the low Si/Ru ratios for Ru-rich samples are likely due to Ru-enrichment in the surface region (see Supporting Information (SI)). High-resolution XPS spectra of the Ru 3d and Si 2p regions are shown in Figure 3-2 A and B, respectively. The binding energy (BE) values are summarized in Table 3-2. Detailed fitting parameters of the Voigt doublets for the Si 2p core level spectra are provided in the Supporting Information. The ruthenium layer Ru-Si(100) shows the Ru 3d BE and the asymmetric line shape which are expected for metallic Ru. In the sample RuSi-PLD, the Ru 3d BE is shifted by +0.22 eV in relation to metallic Ru and exhibits a lower asymmetry. Even though (Ru_2Si_3+RuSi)-PLD, (Ru_2Si_3+Si)-PLD, and Ru_2Si_3-Si(100) are close in composition, their Ru 3d BEs exhibit measurable variations, which are attributed to their phase purity. The peak shapes of these Si rich samples, on the
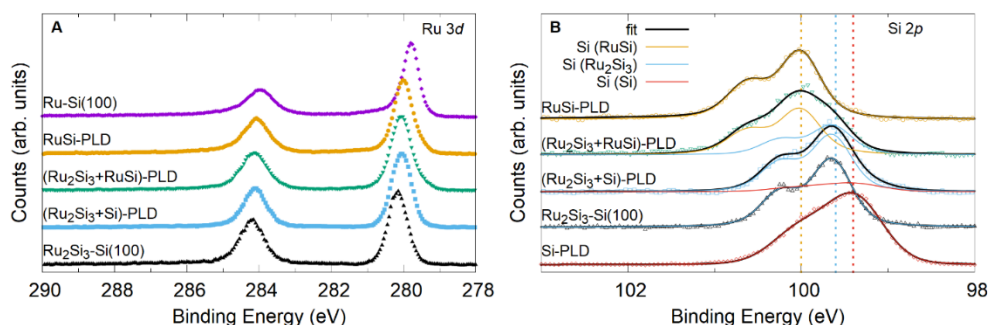
Figure 3-2 High-resolution XPS spectra of Ru silicide layers. A) Ru 3d region of Ru-Si(100), RuSi-PLD, (Ru_2Si_3+RuSi)-PLD, (Ru_2Si_3+Si)-PLD, and Ru_2Si_3-Si(100). B) Si 2p region of RuSi-PLD, (Ru_2Si_3+RuSi)-PLD, (Ru_2Si_3+Si)-PLD, Ru_2Si_3-Si(100), and Si-PLD.

other hand, are symmetric and near-identical. In Figure 3-2 B an overview of the Si 2p spectra of the samples Si-PLD, RuSi-PLD, (Ru_2Si_3+RuSi)-PLD, (Ru_2Si_3+Si)-PLD, and Ru_2Si_3-Si(100) is provided. The peak position of the Si 2p doublet of the Si-PLD sample agrees well with elemental silicon,[169] but its line width is significantly larger compared to that reported for Si single crystals. This broadening is ascribed to disorder and defectivity in the layers produced by PLD at room temperature. Also, the spectra of RuSi-PLD and Ru_2Si_3-Si(100) correspond to a single doublet, whereas the Si 2p spectra of (Ru_2Si_3+Si)-PLD and (Ru_2Si_3+RuSi)-PLD require the addition of a second species, at binding energies corresponding to elemental Si and RuSi, respectively. While the binding energy variations between the silicide species remain small, the binding energy difference between the Ru 3d and the Si 2p levels exhibits a significant step between RuSi-PLD and the two Ru_2Si_3 samples.

	Si/Ru
Ru-Si(100)	0.00
RuSi-PLD	0.78
(Ru_2Si_3+RuSi)-PLD	1.08
(Ru_2Si_3+Si)-PLD	1.58
Ru_2Si_3-Si(100)	1.48

Table 3-1 Atomic ratios determined by XPS of Ru-Si(100), RuSi-PLD, (Ru_2Si_3+RuSi)-PLD, (Ru_2Si_3+Si)-PLD and Ru_2Si_3-Si(100).

	BE Ru 3d	BE Si 2p	BE Ru 3d-Si 2p
Ru-Si(100)	279.8		
RuSi-PLD	280.0	100.0	180.0
Ru_2Si_3-PLD	280.1	99.7	180.4
Ru_2Si_3-Si(100)	280.2	99.7	180.5
Si-PLD		99.4	

Table 3-2 XPS Binding energies of Ru 3d, Si 2p, and the difference between Ru3d and Si 2p of Ru-Si(100), RuSi-PLD, Ru_2Si_3-PLD, Ru_2Si_3-Si(100), and Si-PLD.

All materials in this study present clear, characteristic plasmon loss satellites, which are located at higher apparent binding energy (lower kinetic energy) than the XPS peaks. Extended spectra of the Ru 3d and Si 2p regions for the same samples as in Figure 3-2 are shown in Figure 3-3. The locations of the energy loss peaks are summarized in Table 3-3.
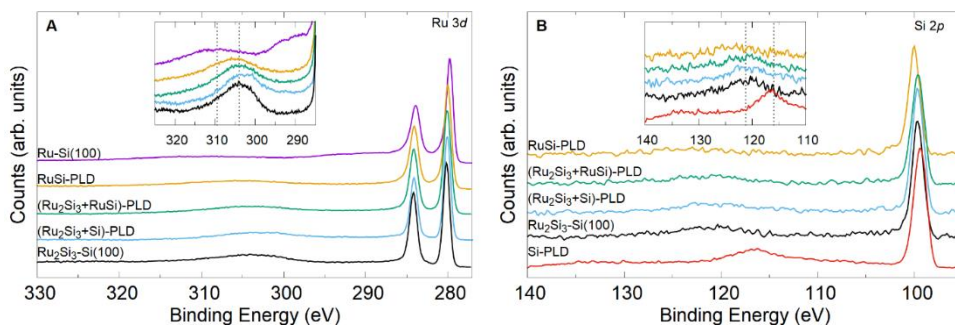
Figure 3-3 Extended-range XPS spectra. A) Ru 3d region of Ru-Si(100), RuSi-PLD, (Ru_2Si_3+RuSi)-PLD, (Ru_2Si_3+Si)-PLD, and Ru_2Si_3-Si(100). B) Si 2p region of RuSi-PLD, (Ru_2Si_3+RuSi)-PLD, (Ru_2Si_3+Si)-PLD, Ru_2Si_3-Si(100), and Si-PLD.

For Ru-Si(100), electron energy loss peaks are observed at +8.0 eV and +29.4 eV from Ru $3d_{5/2}$, in good agreement with reported values for surface and bulk plasmon

features for metallic Ru[170]. For the silicide layers, the respective plasmon loss peaks are located at distinctly different binding energies, corresponding to loss values of +23.3 eV (RuSi-PLD), +22.5 eV ((Ru$_2$Si$_3$+RuSi)-PLD), +22.2 eV (Ru$_2$Si$_3$-Si(100)), and +21.4 eV for (Ru$_2$Si$_3$+Si)-PLD. From these values we see a 1.7eV difference between the plasmon loss peaks between Ru$_2$Si$_3$ and RuSi. The extended-range Si 2p spectra in Figure 3-3 B illustrate that the plasmon loss features for all silicide samples are also observed at comparable loss energies at the Si 2p peak, albeit with poorer signal-to-noise ratio owing to the lower intensity of the Si 2p peak. Moreover, the relative peak area of the plasmon features is lower in the Si 2p region than in the Ru 3d region, indicating a higher excitation cross section of plasmons for the Ru 3d electrons (at lower kinetic energy). The elemental Si-PLD sample exhibits plasmon loss features at +17.0 eV and +34.0 eV (single and double plasmon excitation) from the Si 2p$_{3/2}$ peak. The experimentally observed trends and peak positions are furthermore in good agreement with DFT simulations of RuSi (22.55 eV), Ru$_2$Si$_3$ (21.83 eV), and bulk Si (16.67 eV), which also reproduce the decreasing plasmon loss energy with increasing Si content.

	Energy loss peak (eV)
Ru-Si(100)	+8.0 and +29.4
RuSi-PLD	+23.3
(Ru$_2$Si$_3$+RuSi)-PLD	+22.5
Ru$_2$Si$_3$-Si(100)	+22.2
(Ru$_2$Si$_3$+Si)-PLD	+21.4
Si-PLD	+17.0 and +34.0

Table 3-3 Energy loss peaks for Ru-Si(100), RuSi-PLD, (Ru$_2$Si$_3$+RuSi)-PLD, Ru$_2$Si$_3$-Si(100), (Ru$_2$Si$_3$+Si)-PLD, and Si-PLD.

3.5 Discussion

The presented X-ray diffraction, photoelectron spectroscopy, and density functional theory results connect changes in structure, stoichiometry, and electronic properties to a systematic change in the spectral features of Ru and Si in XPS. While only subtle shifts and changes in peak shape between metal and silicide are observed in the core level spectra, the apparent binding energies of the plasmon loss features present substantial changes with the formation of a silicide and changes in its stoichiometry.

The differences in the Ru 3d core level spectra of Ru metal, RuSi, and Ru_2Si_3 are subtle but discernible in high-resolution spectra with a monochromatic X-ray source and can be related to changes in electronic structure with Si content. The Ru 3d peak shapes are observed to change from asymmetric in the case of a metal layer (Ru-Si(100)) to mostly symmetric for RuSi and fully symmetric for Ru_2Si_3 samples. This observation is in agreement with the metallic character of ruthenium and the semiconducting nature of RuSi and Ru_2Si_3, and their respective density of states at the Fermi level.[110] In addition to the small changes in absolute binding energy values of Ru 3d and Si 2p, a clear change in the energy difference between the Ru 3d and Si 2p peaks was observed for the different silicide phases, from 180.4 eV and 180.5 eV for Ru_2Si_3 prepared in two different ways to 180.0 eV for RuSi. The combination of different absolute binding energies of Ru 3d and Si 2p, differences in their relative position, and systematic changes in their peak shapes provides clear evidence for a change in electronic structure between RuSi-PLD and Ru_2Si_3-PLD. However, these changes to the spectral features are subtle and should not generally serve as the basis for a reliable identification of Ru silicides.

The shifts in the apparent binding energies of the plasmon loss satellites, on the other hand, are evident already from the extended-range spectra and do not rely on high experimental resolution. The transition from elemental Ru and Si to the silicides under investigation is accompanied by a plasmon peak shift of more than 4 eV. In the compositional range between RuSi and Ru_2Si_3, the GI-XRD results show the

formation of phase mixtures. Even though the two silicide phases are expected to have a characteristic plasmon loss energy, a comparison of the respective XPS spectra reveals a gradual shift towards lower plasmon loss energies (lower apparent binding energy) with increasing Si content. This observation is interpreted as a gradual shift in intensity between two coexisting plasmon features for RuSi and Ru_2Si_3, which show a substantial energy difference but also a large line width. The plasmon loss energy thus provides an indication of the average Si content of the silicide, whereas a quantitative identification of the RuSi and Ru_2Si_3 content remains difficult. Based on the distinct shift of the plasmon loss energy with the formation of ruthenium silicide phases, however, the satellite position can be used to unambiguously separate the coexistence of elemental phases from silicides.

The rich information contained in electron energy loss processes is rarely used in photoelectron spectroscopy, partly because the XPS peak shifts already contain information about the oxidation state and chemical environment of the elements. Examples of loss features in XPS have been reported in the context of work that is material-specific to Fe silicides [153,171], while the underlying changes of the dielectric function of the material are a general phenomenon. Electron energy loss spectroscopy, on the other hand, makes use of the characteristic electron energy loss of materials as fingerprint for their composition but also their electronic structure[154]. Examples of the reliable identification of silicides include compounds of Si with Ni [154,172], Fe [153,173,174] and Cr [175], some of which also allow identifying the specific silicide species. Electron energy loss features often exhibit substantially larger peak shifts than the core level peaks in XPS and are thus promising as pathway of the chemical analysis of materials.

An identification of silicides based purely on core level peak shifts in XPS, on the other hand, is challenging for many elements.[144,151,152] The XPS literature on Ru-Si compounds reports small and subtle changes upon silicide formation [144,169,176,177], and could thus strongly benefit from an additional unambiguous probe of the change in

electronic structure induced by silicide formation. Moreover, we expect that the electron energy loss features for various metal silicides provide a clearer signature of the formation of silicide than the respective core level peak positions and shapes, thus alleviating the requirements for resolution and peak deconvolution.

3.6   Conclusions

In summary, we demonstrate on the example of Ru silicide that the energy of plasmon loss features in photoelectron spectra can serve as sensitive descriptor for the identification of compounds with different electronic structure. For Ru, which exhibits only subtle core level shifts upon silicide formation, the plasmon loss peak position changes by several electron volts compared to elemental Si and Ru, and progressively shifts with Si content. This approach to identify compounds is common in EELS but rarely used in XPS and holds potential for application to a broad range of materials.

3

3.7   Appendix

S1: GI-XRD 2D diffraction pattern of (Ru$_2$Si$_3$+RuSi)-PLD

In Figure S 3-1 the GI-XRD 2D detector image is shown of the sample (Ru$_2$Si$_3$+RuSi)-PLD. The blue outline is the detector integration area. The white arrow indicates the saturated pixels underlying the peak marked by an asterisk (*) at a diffraction angle (2θ) of 40° in Figure 3-1. The blue arrow shows the diffraction ring corresponding to the peak at a diffraction angle (2θ) of 55°.
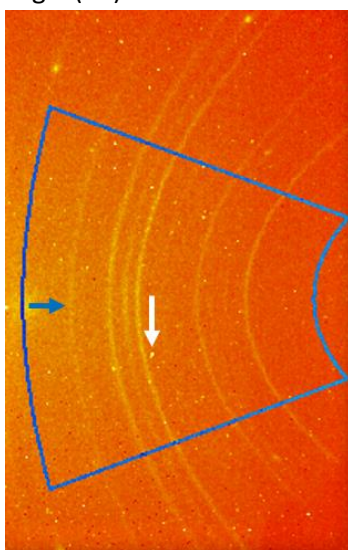
Figure S 3-1   2D diffraction pattern of (Ru$_2$Si$_3$+RuSi)-PLD. Raw data of the diffractogram reported in Figure 3-1.

3

S2: XPS Si 2p peak fitting parameters

	Si (Si 2p)	Ru$_2$Si$_3$ (Si 2p)	RuSi (Si 2p)
Pos (eV)	99.4	99.7	100.0
Lwid (eV)	0.07	0.18	0.25
Gwid (eV)	0.71	0.46	0.45
Split (eV)	0.63	0.62	0.62

Table S 3-1 Peak fitting parameters of the Si 2p species: Si, Ru$_2$Si$_3$, and RuSi, using Voigt doublets with the following parameters: binding energy position (pos), Lorentzian line width (Lwid), Gaussian line width (Gwid), spin-orbit split.

S3: Atomic ratios determination using Ru 3p, Ru 3d, and Ru 4p

The peak areas of the Ru 3p, Ru 3d, and Ru 4p core levels have been determined from XPS survey spectra for all samples. The kinetic energies of the Ru 3p$_{3/2}$, Ru 3d$_{5/2}$, and Ru 4p$_{3/2}$ photoelectrons are 1024 eV, 1206 eV, and 1443 eV, resulting in the highest probing depth for Ru 4p, followed by Ru 3d and Ru 3p. Table S 3-2 shows the measured Ru content corrected for photoemission cross section and probing depth. The values are normalized to the result for Ru 3d. The lower Ru signal for Ru 4p and higher Ru signal for Ru 3p is particularly pronounced for the samples containing the RuSi phase, indicating Ru enrichment in the surface region for these samples.

	Ru 4p	Ru 3d	Ru 3p
Ru$_2$Si$_3$-Si(100)	0,85	1,00	1,04
(Ru$_2$Si$_3$+RuSi)-PLD	0,80	1,00	1,18
RuSi-PLD	0,80	1,00	1,26
(Ru$_2$Si$_3$+Si)-PLD	0,71	1,00	0,99

Table S 3-2 Atomic ratios determined by XPS of Ru 4p, Ru 3d, and Ru 3p for the samples Ru-Si(100), RuSi-PLD, (Ru$_2$Si$_3$+RuSi)-PLD, (Ru$_2$Si$_3$+Si)-PLD and Ru$_2$Si$_3$-Si(100).

4

The Role of Cation Vacancies in the Initial Oxidation of Ru(0001)

4.1 Abstract

Understanding the active surface structure of a catalytic material at relevant operating conditions is essential for accurately predicting the activity and selectivity of a catalyst. Traditional models, based on idealized surface structures neglecting defects, often fall short in realistically depicting catalyst surfaces in operation. Even for the widely studied Ru(0001) surface, understanding of the initial oxidation kinetics beyond an adsorbed monolayer remains elusive. Challenged by resolving the atomic structure, here we identify the crucial role defects play in the growth of the first oxide layers. Using *in situ* X-ray photoelectron spectroscopy (XPS) combined with density functional theory (DFT), we uncover a two-step oxidation process of Ru(0001) and pinpoint the significant role of ruthenium vacancies in the initial oxidation of Ru(0001). Ruthenium (=cation) vacancies prove more adept at mitigating surface strain than oxygen (=anion) vacancies in the growing oxide layer. While cation vacancies are often neglected in the context of interfaces, here they provide a vector for further oxide growth. These observations reconcile the ambiguities in understanding the initial Ru(0001) oxidation and highlight the importance of cation vacancies for this process.

4

4.2 Introduction

The interplay between a material's surface structure and its response to reactive environments is decisive for its performance as a catalyst or protective coating. Variations in surface structure, composition, and electronic properties are not mere nuances; they are central to the reactivity and selectivity that define the effectiveness of a material under operating conditions. For functional oxides, the focus of mechanistic studies has traditionally been on surface oxygen vacancies and how these influence the properties of materials with broad applications such as TiO_2, MgO, or ZnO [178,179]. Recent findings, however, have unveiled the widely underestimated role of cation vacancies in defining the surface properties of transition metal oxides [180,181].

In the light of extensive discussions on the active surface structures of catalytic materials under operating conditions [182–187], the related structure search should not be confined to stoichiometric equilibrium phases known from the bulk. Especially under oxidizing conditions, critical deviations from the idealized defect-free towards defect-rich active phases have been observed for prototypical catalyst surfaces [188–190]. State-of-the-art experimental methods have recently allowed to characterize the active phase of catalytic surfaces under relevant, *in operando* conditions [52,191–194] and compare it to theoretical predictions. However, in these studies surface defects have not been explicitly included in the accompanying DFT calculations. As Ru-based materials are excellent catalysts, the Ru(0001) surface in an oxidizing environment and its defect chemistry represents a highly relevant showcase for searching the active phase: While Ru catalyzes the formation of ammonia [12,13] and Fischer-Tropsch synthesis [10,11], RuO_2 is one of the best performing catalysts for the oxygen evolution reaction [65,66]. The main surfaces of these materials have thus been studied in detail and the structures of the close-packed Ru(0001), and the RuO_2(110) surfaces are considered solved [77,78]. However, these equilibrium structures of metallic and oxidized Ru are not necessarily the most relevant ones for determining the reactivity of Ru in oxidizing reaction environments.

In the search for the active surface structure of Ru for different chemical potentials of oxygen, phases with increasing oxygen content have been investigated, as illustrated in Figure 4-1. The oxidation of Ru has been shown to proceed *via* a number of ordered structures of adsorbed oxygen (Figure 4-1a), with the (2 × 2) oxygen superstructure being most stable in terms of formation energy per oxygen atom (Figure 4-1b) [67]. This result was confirmed using low-energy electron diffraction (LEED) experiments, extending the range of ordered adsorbate structures to higher ((2 × 1) and (1 × 1)) coverages. Experimental and theoretical work provide compelling evidence that beyond the surface-adsorbed monolayer, oxidation proceeds *via* a so-called surface oxide [76,86,87,89,90,95], which is structurally and electronically different
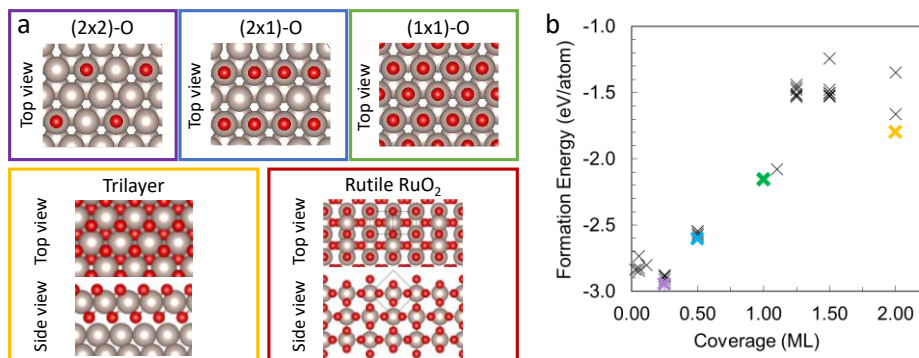
Figure 4-1 a) Illustration of the reported structures occurring during the oxidation of Ru, ranging from ordered adsorbate superstructures (purple, blue and green) to an intermediate oxide with trilayer structure (yellow) to the stable RuO$_2$ bulk oxide (red). b) These structures are most stable in terms of their formation energy per oxygen atom in different coverage regimes as indicated by the bold crosses using the same coloring scheme. Coverage is given in fraction of a monolayer (ML), whereby 1 ML is defined as one oxygen atom per Ru surface atom. This plot is based on the 68 defect-free surface structures sampled as part of this work for the defect calculations (vide infra).

from bulk rutile RuO$_2$, and is converted to the latter at a critical thickness [22,91–93]. One of the most promising models for this intermediate oxide is a metastable O-Ru-O trilayer [92], analogous to the initial oxide layers observed for Ag [195], Rh [196], Pt [197] and Ir [98]. The caveat for this Ru oxide trilayer, however, is that conclusive evidence for it could neither be obtained with diffraction techniques such as surface X-ray diffraction [76] and LEED [86], nor with real-space methods such as low-energy electron microscopy [74,88,90,94] and scanning tunneling microscopy [23,60,73–75,81,101,102]. Literature offers explanations for several intriguing aspects of the transition from a flat Ru(0001) layer to RuO$_2$(110), such as the formation of a nanostructured phase [87] and the coexistence of different facets [86]. However, fundamental details on the defect chemistry, formation and kinetics of conversion of the likely disordered or defect-dominated structure in the intermediate phase between a monolayer of oxygen and rutile RuO$_2$ remain elusive.

In this study, we delve deeper into the formation of the initial oxide layer on Ru(0001), emphasizing the instrumental role vacancies play in the forming oxide. Moreover, we demonstrate the pivotal role of surface preparation and the associated defect concentration by showing that oxide growth is impeded on flat, polished Ru(0001) surfaces. This is supported by large-scale DFT calculations, systematically sampling structural models for the oxidation of Ru(0001) as a function of coverage (Figure 4-1b) and explicitly investigating defect formation. Through this unprecedented combination of *in situ* XPS and DFT, our findings uncover new aspects regarding the oxidation of this surface, showing the interplay between strain, defect formation, and growth.

4.3   Results and Discussion

4.3.1   Initial Oxidation

As a first step, to determine the initial oxidation of Ru we performed a time-dependent study of the surface composition and oxidation state of Ru using XPS at elevated temperatures in an oxygen environment. A series of consecutive *in situ* XPS spectra were recorded while exposing an unpolished Ru(0001) single crystal to 1.2×10^{-4} mbar O_2 at constant temperatures in the range from 290°C to 470°C. Figure 2a shows the apparent thickness of the forming oxide as a function of time for selected temperatures, estimated from the Ru oxide peak intensity assuming the growth of a homogeneous flat layer. The calculated oxide thickness at long oxidation times increases monotonically with temperature, in accordance with literature [46,103]. The growth kinetics at different temperatures, however, reveal the presence of two distinct oxidation regimes. At temperatures <400°C, the thickness increases gradually, and growth slows down for long oxidation times. Above 400°C, the smooth oxidation curves begin to jump at the beginning, with an initial oxidation to approximately 0.6 nm during 10-15 minutes, followed by a rapid increase in apparent oxide thickness. After a brief period of rapid oxidation, the curve approaches saturation at a temperature-dependent value, and the rate of oxide growth markedly decreases. Regardless of oxidation temperature, the oxidation during the first 15 minutes appears uniform, showing a plateau after the onset of oxidation (Figure 4-2a and inset). It is instructive to note that the calculated thickness of 0.6 nm for the plateau of initial oxidation is in good agreement with two layers of the ruthenium oxide trilayer structure from our ab initio calculations (0.57 nm for 2 trilayers). The temperature independence of the plateau suggest that the effect is caused by growth kinetics or sample preparation. At this stage, it is thus important to untangle the role defects play in the initial oxidation. To achieve this, a polished Ru(0001) sample is used as a control, reducing the average surface roughness by more than one order of magnitude and thus changing the concentration of surface defects present at the Ru surface. In tandem DFT calculations of the vacancy formation energy as a function of O-coverage were performed to allow potential candidate defects to be identified.

4
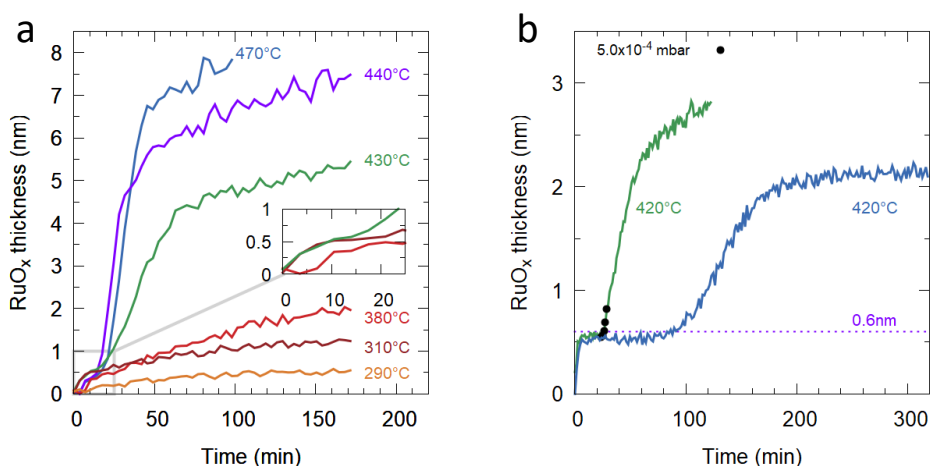
Figure 4-2 In situ oxidation curves of unpolished (a) and polished (b) Ru(0001) at different surface temperatures in 1.2 × 10⁻⁴ mbar O₂ (with thicknesses calculated assuming homogenous flat layers). a) All but the lowest-temperature oxidation curves (T=290 and 310 °C) coincide up to a thickness of 0.6 nm. At temperatures below 400°C, growth continues smoothly with gradual oxidation. The high-temperature curves are characterized by a pronounced slow-down and plateau before oxidation continues at a higher rate. The inset highlights the initial growth behavior and its agreement for different temperatures. b) On polished Ru(0001), the growth reaches a plateau close to 0.6 nm and remains stable over more than 1h (blue). A short period of exposure to higher pressure (black dots, 5.0 × 10⁻⁴ mbar O₂) initiates a transition to rapid growth (green).

Investigating the polished Ru(0001) single crystal (Figure 4-2b, blue curve) revealed a marked difference in oxidation behavior compared to the unpolished counterpart (Figure 4-2a). While in both cases, an initial oxidation plateau at 0.6 nm is observed, the thickness of this initial oxide overlayer remains constant at the polished surface for approximately 80 minutes. Even after further oxidation commences, the thickness only increases slowly. This markedly different oxidation behavior of the two samples can be rationalized by their difference in surface roughness: The reduced defect concentration in case of the polished Ru(0001) sample offers fewer reactive sites for oxygen dissociation and incorporation and thus increases the kinetic hindrance of oxide growth, in agreement with literature results on faster growth upon intentional damage to Ru oxide layers [89].

To verify this observation, defect formation energies (E_{form}) for ruthenium vacancies (V_{Ru}) in both the pristine and oxidized Ru(0001) surface were calculated via DFT, using the surface structures illustrated in Figure 4-1b as a starting point. Figure 4-3a demonstrates that V_{Ru} becomes significantly more favored at the Ru(0001) surface (1.93 eV) compared to the bulk (2.70 eV). The former is still sizable and consequently the equilibrium concentration of surface atom vacancies in the absence of external factors would be predicted to be negligible. However, in the presence of oxygen in form of commonly known on- or sub-surface adsorption structures, a further

significant reduction in $E_{form}(V_{Ru})$ is obtained (Figure 4-3b). Between 0 and 1 monolayer (ML), $E_{form}(V_{Ru})$ is reduced from 1.93 eV to 0.73 eV, resulting in an energy range where the V_{Ru} concentration cannot be readily neglected. Beyond 1 ML the formation energy decreases further, reaching a minimum at 2 ML, with a defect formation energy of –0.53 eV, driven by strain release in the forming oxide. It is important to note in the context of oxidation that the decrease in V_{Ru} formation energy is not confined to the surface layer. Vacancy formation energies in the sub-surface show a similar trend (Figure 4-3b), decreasing from 2.47 eV for pristine Ru to 0.13 eV at 2 ML of oxygen. The reduction in $E_{form}(V_{Ru})$ in both the surface and sub-surface layers indicates the likely presence of V_{Ru} in the oxide layer, offering a potential vector for the continued oxidation of Ru(0001). The formation energy for oxygen vacancies (V_O) has also been calculated for the same structures as used for the V_{Ru} calculations. As shown Figure 4-3b the results are significantly higher than
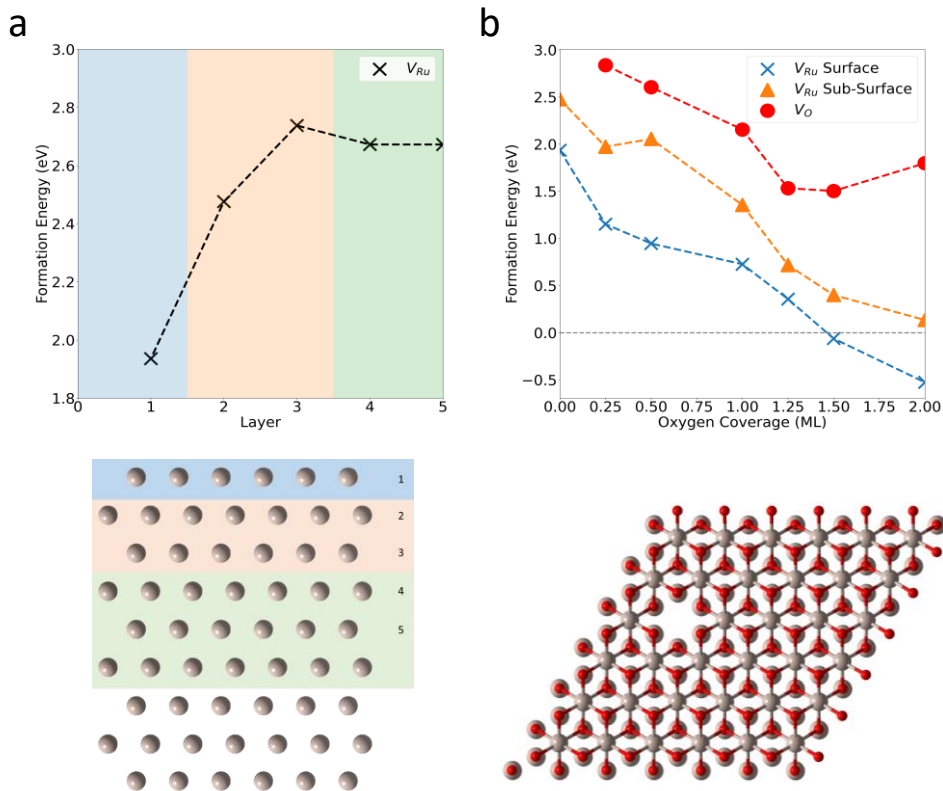
Figure 4-3 *a) Formation energy for the V_{Ru} defect in pristine ruthenium as a function of position given by the layer in which the vacancy is located, moving from the bulk (green), to the near surface (orange), and finally at the surface (blue). b) Trend in formation energy for the V_{Ru} and V_O as a function of oxygen coverage in the forming oxide. The V_{Ru} are considered both in the oxide layer (blue crosses) and directly below (orange triangles). In all cases where multiple symmetry sites are possible the lowest-energy results are reported.*

$E_{form}(V_{Ru})$ for the entire range of coverages up to 2 ML. Although oxygen vacancies are often the predominant species providing strain release and mobility, here they are unlikely to be present at significant concentrations based on their formation energy of 1.9 eV for the Ru oxide trilayer. The barriers for V_{Ru} formation on a 1 ML O-coverage surface and the 2 ML trilayer are 3.8 and 1.47 eV respectively. The corresponding barriers for recombination are approximately 2.7 and 0.5 eV lower for the 1ML and 2 ML respectively, favoring this process over the vacancy formation. The underlying nudged elastic band trajectories are provided in the SI. Consequently, the diffusion of the Ru atoms away from the formed vacancy sites is the critical process that likely limits the rate of formation and thus the density of Ru vacancies.

After the initial oxidation, a transition to a rapid oxidation rate can be achieved by increasing the O_2 partial pressure. Already increasing the pressure to 5×10^{-4} mbar for several minutes results in an oxidation curve (green in Figure 4-2b) yielding higher thicknesses than 0.6 nm, which is more similar to oxidation of the unpolished surface at 1.2×10^{-4} mbar at 430 °C. A tentative interpretation is the formation of chemically induced defects in the oxide on the low-roughness surface of the polished Ru(0001) sample. This modification in growth rate is concomitant with an overall increase in the final oxide layer thickness over the extended observation time (~2.8 nm for the green versus ~2 nm for the blue curve). The difference in the oxidation rate is at first glance consistent with literature reports attributing accelerated oxidation on RuO_2 to the differences in the (dissociative) sticking probability of O_2, changing from 0.4 for Ru metal to 10^{-6} with the formation of the first adsorbed oxygen layer [50,198], before increasing again to 0.7 for RuO_2 [198]. However, differences in local properties such as sticking coefficients alone do not explain the different oxidation kinetics of polished and unpolished Ru(0001) surfaces. The thickness plateau for polished surfaces indicates a kinetic growth limitation, which is likely to involve transport between layers, based on the faster transition for rougher surfaces of the same orientation. We speculate that a defect-free oxide trilayer hinders transport between surface and sub-surface, which is, however, required for reaching the critical layer thickness for the transition to the rutile phase. Modifying the oxygen chemical potential by changing the oxygen pressure for a time scale of minutes is sufficient to increase the defect density in the layer to a higher equilibrium value, thus generating new channels for interlayer transport. This mechanism is expected to enable a faster transition to the second growth regime and is consistent with literature results at higher pressures [103] that could not resolve the characteristic plateau upon formation of the suspected Ru oxide trilayer.

4.3.2   Subsequent oxidation towards bulk oxide

Whilst Figure 4-2 and Figure 4-3 clearly show that the thickness behavior varies with conditions and sample preparation, at this stage no link between the two phases of growth and a change in the nature of the oxide has been made. To establish this connection, we make use of the changes in electronic structure with Ru oxidation, which are not only reflected by changes in Ru core level energies [82–84] but also by the appearance of a characteristic satellite peak upon formation of rutile RuO_2 [82,84,85]. Since the satellite peak intensity is expected to scale with the amount of rutile RuO_2, it is instructive to compare its intensity to that of the peak corresponding to oxidized Ru. Figure 4-4 illustrates that during the oxidation of the polished Ru(0001) crystal at 420°C this rutile RuO_2 satellite (black curve, left axis) is absent at low oxide thicknesses (red curve, right axis) up to the previously mentioned plateau at 0.6 nm. Upon exceeding this value, the satellite peak appears and continues to grow with increasing layer thickness. This threshold thickness is observed reproducibly, also for the unpolished sample (Figure S 4-7) and upon increasing the pressure to accelerate oxidation (Figure S 4-9). The emergence of the characteristic rutile RuO_2 satellite close to two trilayer thicknesses is in good agreement with estimates of the critical thickness for conversion to the thermodynamically stable phase of RuO_2 [92]. Already at 2 nm, the peak area reaches a value close to the saturation point just above 0.3 observed for thicker oxide layers (Figure S 4-7). The knowledge of the
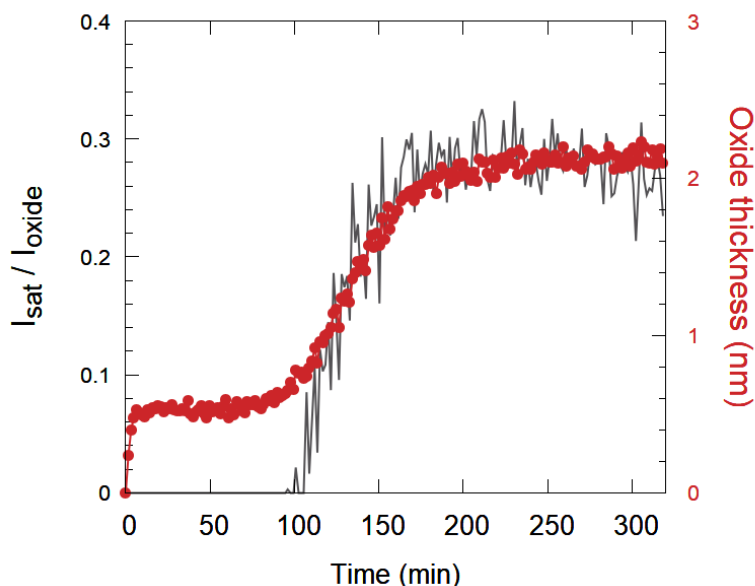

Figure 4-4 *Intensity of the rutile RuO$_2$ satellite XPS species (left axis) normalized to total Ru oxide intensity for polished Ru(0001) at 420 °C at 1.2 × 10^{-4} mbar O$_2$. No satellite is detected for the thickness below 0.6 nm. Upon exceeding 0.6 nm, the satellite intensity increases with the oxide thickness.*

characteristic satellite peak intensity for pure RuO_2 can be instrumentalized to estimate the fractions of RuO_2 in the oxide layer that correspond to rutile and the metastable intermediate oxide. The calculation, however, requires several assumptions regarding the distribution of the two types of oxides and their thicknesses. A homogeneous thickness is likely only achieved before conversion (in the plateau region) and after full conversion, followed by an extended growth time to reach a similar final thickness of RuO_2 across the surface.

4.4 Conclusions and Outlook

The results presented here show the complexity inherent to the oxidation of Ru(0001), unveiling a two-stage oxidation process. The initial oxidation to approximately 0.6 nm is demonstrated to be largely independent of sample preparation and conditions. In contrast, subsequent oxidation towards the bulk oxide (rutile RuO_2), is characterized by a rapid increase in oxide thickness and shows a dependence on both sample preparation and oxygen pressure. In agreement with the prevailing wisdom, the extensive computational search of structures with adsorbed oxygen as a function of coverage confirm that initial oxidation proceeds via several ordered structures until a full monolayer of oxygen (1 × 1 overlayer structure) has been adsorbed. Above 1 ML O-coverage, the strain in the forming oxide reaches a level that increasingly favors the formation of V_{Ru}. The V_{Ru} is shown to be the most efficient defect-mediated vector for strain release in the forming oxide. The V_O allows for negligible relaxation, and as such is a poor vector for strain release, expressed in a formation energy of 1.9 eV. This intrinsic tendency to form a defect-rich oxide film rationalizes the difficulty to quantitatively verify the structure using diffraction and imaging techniques requiring high levels of order at the surface. The close relation of intrinsic defects to both, oxygen chemical potential and transport through layers, suggests a connection between the introduction of vacancies in the forming oxide and the transition between the two regimes of oxidation. The inference is that an unpolished Ru(0001) surface provides a greater variety of surface morphologies including defects, thereby offering a range of routes for further oxidation. Furthermore, this understanding provides an explanation for the smooth transition from the initial oxidation to the bulk-like regime seen for the unpolished samples at low temperatures. Likewise, the rapid onset at high temperatures can be attributed to additional defect creation introducing additional oxidation pathways. Furthermore, this cation-vacancy-mediated oxidation explains the behavior of the polished sample, where further oxidation is inhibited unless additional ruthenium vacancies are formed by increasing the O-partial pressure, allowing the system to reach a critical oxygen content to transition from the initial regime of oxide layer formation to bulk oxidation.

The results reported and the proposed Ru-vacancy-based mechanism for the initial oxidation of Ru raise awareness of cation vacancies and their underestimated role in the surface chemistry of materials with a broad application perspective while at the same time leaving a number of tantalizing questions. Quantitative experiments on surface structure and calculations of the kinetics of oxide growth will provide a valuable extension of our work to refine structural details and determine defect densities and diffusion pathways in the initial oxide layer on Ru.

4.5   Materials and Methods

The experiments were performed on a polished and an unpolished Ru(0001) single crystal. The average root-mean square roughness of the Ru samples was 0.6 nm (polished) and 11.7 nm (unpolished), as measured by atomic force microscopy in air using a Bruker Dimension Icon system operated in tapping mode. Clean Ru(0001) surfaces were prepared by annealing at 300°C in 10^{-4} mbar O_2, followed by 700°C in UHV for one hour. The absence of contaminants and residual oxygen was confirmed using XPS. For the *in situ* experiments, the Ru(0001) crystals were stabilized at the desired temperature before introducing 1.2×10^{-4} mbar O_2 (Messer CAN-Gas O_2 5.0 (Purity 99.999%)) via a high-precision leak valve.

The XPS measurements were carried out using a Scienta Omicron HiPP-3 spectrometer with a 1.0 mm slit setting and an XM1200 monochromatic Al Kα X-ray source. Pass energies of 100 eV and 300 eV were used for high-resolution and overview spectra, respectively. The XPS peaks were fitted using KolXPD, using Doniach-Sunjic line shapes convoluted with a Gaussian for all Ru 3d components and Voigt shapes for the O 1s peaks. The background was approximated by a Shirley function. High-resolution reference spectra and detailed fitting parameters are provided in the Supporting Information (SI) in Figure S 4-1 and Table S 4-1. The relative intensities of Ru and O are corrected for photoemission cross sections [116] and inelastic mean free paths (IMFPs) derived using the QUASES software package [133]. The average oxide layer thickness is approximated from the oxidized and metallic Ru 3d peak areas, assuming a homogenous overlayer on a flat substrate [132]. Low-energy electron diffraction (LEED) was performed using an OCT Vacuum Microengineering setup with BDL600IR LEED optics and a G10 miniature electron gun.

Spin-polarized DFT calculations were performed using the CP2K code to examine the initial oxide layer formation on Ru(0001) surface, employing the DZVP-SR-MOLOPT basis sets for valence electrons and the GTH-pseudopotential for core electrons [199–205]. A plane wave cutoff of 850 Ry and a relative cutoff 60 Ry were converged to 0.1 meV per formula unit. All calculations were performed at the Γ-point using the Perdew-Burke-Ernzerhof (PBE) functional [165,206], augmented

with the D3-BJ dispersion correction [207–210]. The simulation cell was based on a 6 × 6 × 5 supercell expansion of the bulk primitive cell, containing 396 Ru atoms (and the equivalent orthogonal cell). The lattice vectors and ion positions were relaxed, employing the quasi-Newton BFGS update scheme with a max force threshold of 0.001 eV/Å. For the surface calculations, the vacuum slab was converged above 12 Å, with 27 Å used to account for all O-coverages. O-adsorption geometries were symmetrically sampled based on the previous literature approach [78,91,92,211]. Using the aforementioned computational setup, the structures and energetic orderings accord with the available literature and form the starting structures for the defect calculations (Figure 4-1).

4.6   Acknowledgements

4

4.7 Supporting Information

S1: XPS peaks and fitting parameters

In Figure S 4-1 the comparison of the Ru 3d and O 1s levels before and after exposure to 1.2 x 10^{-4} mbar O_2 at 470 °C for 95 minutes illustrates the emergence of a strong Ru oxide peak. Next to the dominant RuO_2 peak, the rutile RuO_2 satellite peaks and a small Ru metal peak were identified. The O 1s spectrum in Figure 1D can be explained using two components, an O-Ru bond and a second oxygen species which is attributed to the OH-Ru species. [13] The peak fitting parameters resolved from these experiments are shown in Table S 4-1.
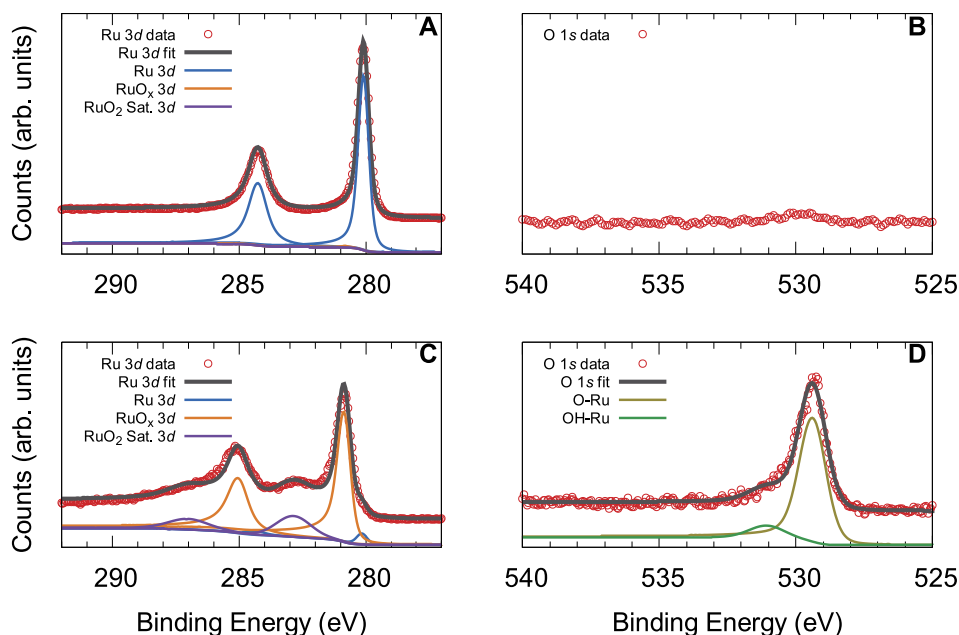
Figure S 4-1 High-resolution XPS of Ru(0001) before and after oxidation at 470 °C in 1.2×10^{-4} mbar O_2. A) Before oxidation, the Ru 3d core level shows only metallic Ru. B) O 1s before oxidation C) After oxidation the Ru 3d spectrum is dominated by a Ru oxide peak and a satellite characteristic of the bulk-

	Ru $3d_{5/2}$	Ru $3d_{3/2}$	RuO_x $3d_{5/2}$	RuO_x $3d_{3/2}$	RuO_2 satellite $3d_{5/2}$	RuO_2 satellite $3d_{3/2}$	O 1s (RuO_x)	O 1s
Peak shape	DS-G	DS-G	DS-G	DS-G	Voigt	Voigt	DS-G	Voigt
Pos (eV)	279.8	284.0	280.5	284.7	282.5	286.7	529.1	530.8
Lwid (eV)	0.19	0.70	0.20	0.70	0.20	0.70	0.13	0.13
Lasm (eV)	0.04	0.03	0.13	0.11	-	-	0.12	-
Gwid (eV)	0.37	0.37	0.47	0.47	1.50	1.50	1.02	1.86

Table S 4-1 XPS peak fitting parameters for high-resolution spectra of the Ru 3d and O 1s core levels, including the binding energy position (Pos), the Lorentzian and Gaussian line widths (Lwid, Gwid) of the Voigt profile, and the asymmetry parameter of the Doniach-Sunjic line shape.

S2: LEED pattern of clean Ru(0001)

To determine the cleanliness of the surface, low-energy electron diffraction (LEED) images were collected of the cleaned polished Ru(0001). In Figure S 4-2 the LEED pattern at different beam energies is showing the expected pattern for a clean Ru(0001) surface.

The LEED setup is operated in a chamber with a base pressure of 2×10^{-11} mbar. Introducing a sample raises the pressures to the low 10^{-9} mbar range. The electron energy is provided at top left of each image.
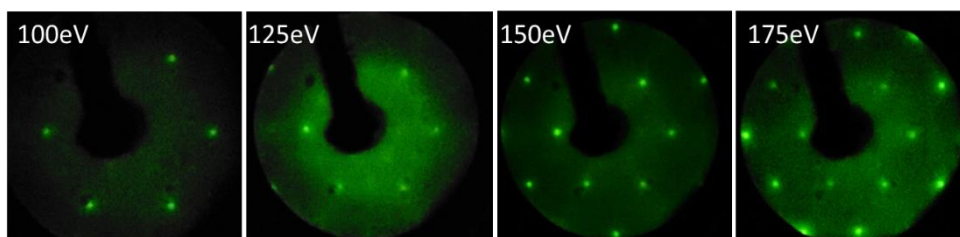
Figure S 4-2 LEED images of as-prepared Ru(0001) at different electron energies. The pattern is in agreement with the hexagonal structure of Ru and the symmetry expected at the (0001) surface. The intensity between the spots (clearest for 125 eV) is attributed to the presence of small amounts of oxygen at the surface, forming a superstructure in parts of the surface.

S3: Evolution of individual species

In support of Figure 4-4 in the main text, the individual species of the three different temperatures are shown in Figure S 4-3. The ruthenium metal intensity (blue) decreases during exposure, faster for the high temperature. The ruthenium oxide intensity (orange) increases during exposure. The rutile RuO_2 satellite species (purple) begins to emerge after approximately 30 minutes for the intermediate temperature and 10 minutes for the high temperature. The satellite species for the high-temperature graph emerges at a similar time as the RuO_x species starts its accelerated growth. From the spectra of the O 1s the O-Ru species (ochre), which are attributed to the ruthenium oxide phase, are increasing in intensity over time.
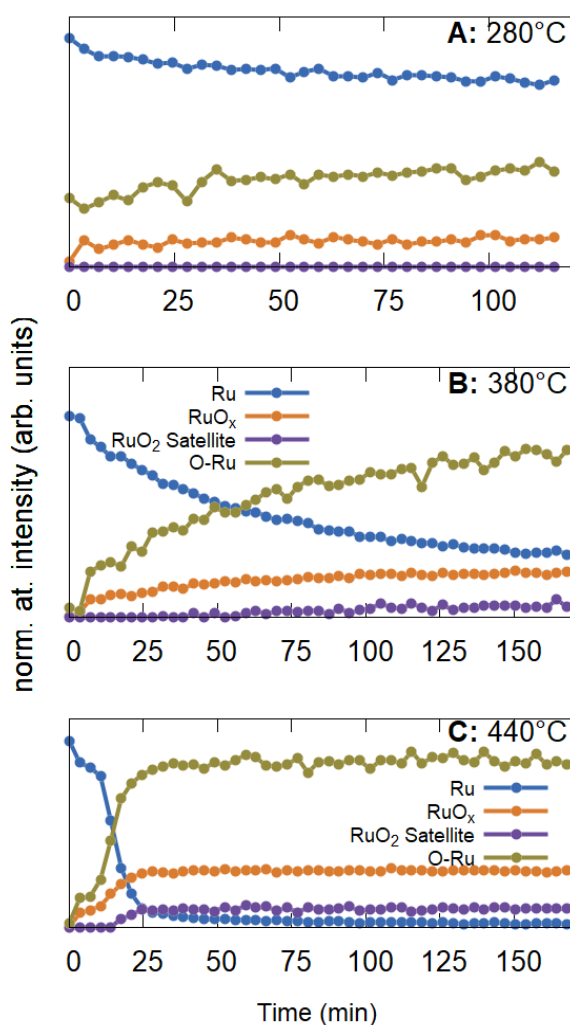
Figure S 4-3 XPS peak areas of individual species during exposure of Ru(0001) of 1.2 x 10^{-4} mbar O$_2$ at 280°C (A), 380 °C (B), and 440 °C (C) (Ru, RuO$_x$, RuO$_2$ Satellite, and O-Ru).

S4: AFM images of Ru(0001) polished and unpolished

The surface roughness of the polished and unpolished Ru(0001) is determined from atomic force microscopy (AFM) images (obtained using a Bruker Dimension Icon with PeakForce Tapping and a scanasyst-air tip). Examples are shown in Figure S 4-4. In Figure S 4-5 the optical images of the sample and AFM tip are shown for polished (A) and unpolished (B) Ru(0001). From the optical image the unpolished image shows horizontal lines, which are visible lines seen on the surface. Three different locations of each crystal were imaged using AFM images. The average RMS roughness is 0.55 nm and 11.66 nm for polished and unpolished Ru(0001), respectively. The images of the polished (A) and unpolished (B) Ru(0001) samples exhibit an RMS roughness value of 0.46nm and 4.24nm, respectively.
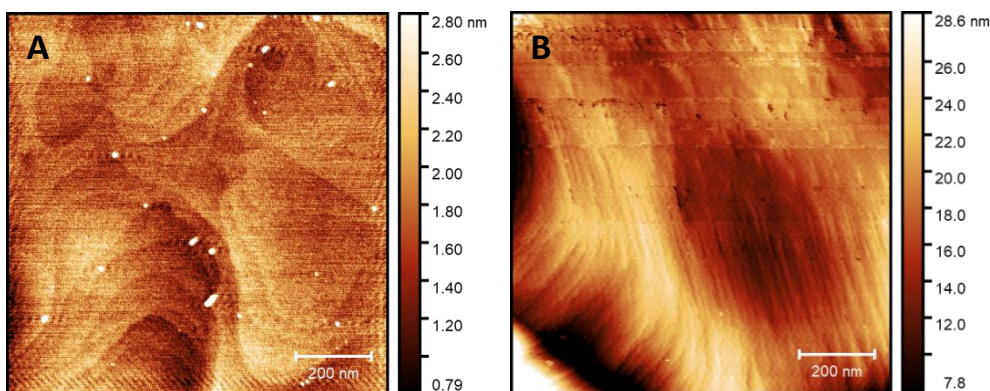
Figure S 4-4 AFM image of (A) polished Ru(0001), (B) unpolished Ru(0001).
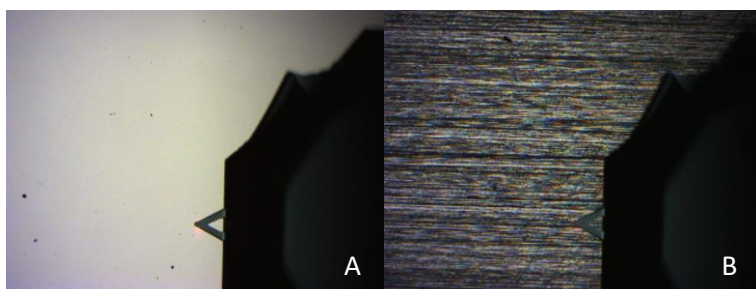
Figure S 4-5 Optical image of A) polished Ru(0001), B) unpolished Ru(0001).

S5: XPS oxide growth polished single crystal

In support of Figure 4-2b, the polished Ru(0001) sample is exposed at 340°C, 350°C, and 360°C, with temporary increases of pressure from 1.2×10^{-4} mbar to 5.0×10^{-4} mbar O_2, see Figure S 4-6. During these exposures, no increment of oxide thickness has been identified.
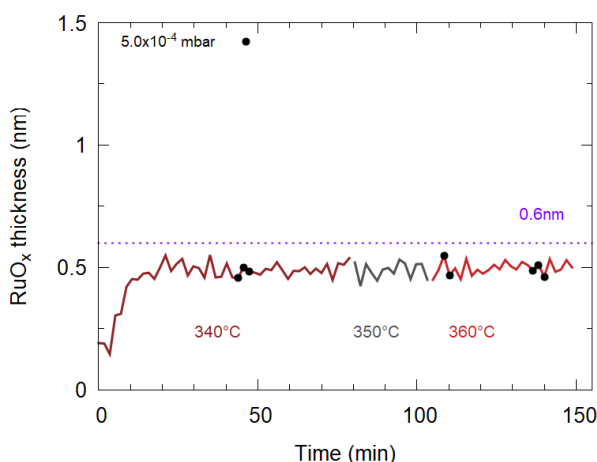
Figure S 4-6 Ruthenium oxide thickness (nm) as a function of time at different constant temperatures in 1.2×10^{-4} mbar O_2 on polished Ru(0001).

S6: XPS analysis of the rutile RuO_2 satellite for unpolished Ru(0001)

Figure S 4-7 shows for unpolished Ru(0001) that the rutile RuO_2 satellite (black curve, left axis) is absent at low oxide thicknesses and reproducibly appears at a well-defined point in the oxidation process. The satellite intensity is expected to scale with the amount of rutile RuO_2, which is part of the total oxide thickness (red curve, right axis). The purple horizontal lines highlight an oxide thickness of 0.6 nm. For 280°C in Figure S 4-7A, the oxide thickness is increasing and leveling off at approximately 0.5 nm; no rutile RuO_2 satellite is observed. At 380°C (Figure S 4-7B) the oxide layer exceeds 0.6 nm at approximately 30 min, which coincides with the first indications of the satellite emerging, shown here as a rolling average over five values with gray areas indicating the respective minima and maxima. The normalized intensity of the satellite steadily increases with growing oxide thickness and reaches a value of 0.25 after 150 min. In Figure S 4-7C, the results for 440°C show a slow growth of RuO_x up to 0.6 nm, which accelerates at 14 minutes and exceeds an oxide thickness of 4 nm in under 30 min. The appearance of the rutile RuO_2 satellite coincides with this change in oxidation rate, which occurs at an approximate oxide thickness of 0.6 nm. While the onset thickness of the satellite appearance in

71

Figure S 4-7C cannot be identified at the time resolution of the experiment, a rapid increase upon exceeding the initial thickness plateau is clearly shown. In contrast to the results at intermediate temperature, the intensity ratio of the satellite and the main Ru oxide peak approaches a saturation value at approximately 0.32.
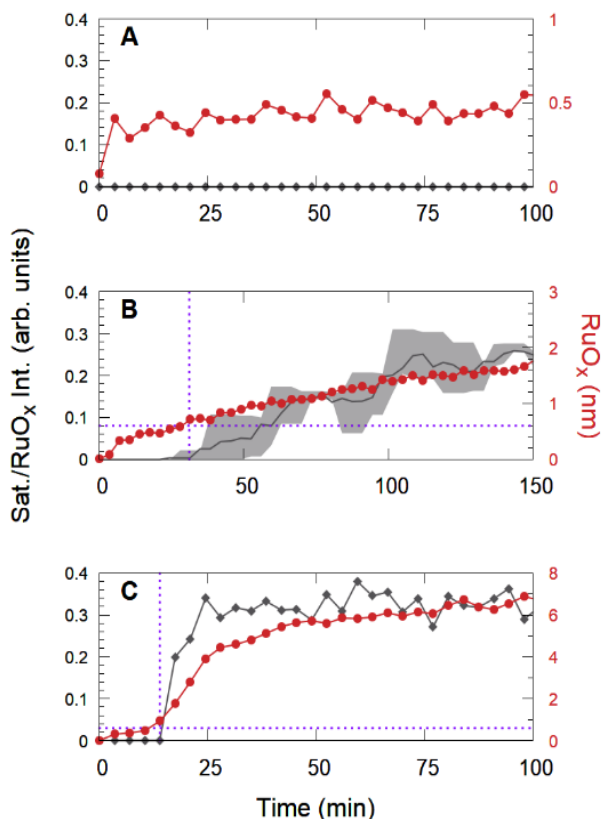
Figure S 4-7 Intensity of the rutile RuO_2 satellite XPS species (left axis) normalized to total Ru oxide for unpolished Ru(0001) in 1.2×10^{-4} mbar O_2 at 280 °C (A), 380 °C (B), and 440 °C (C). The horizontal purple dotted line marks the point of 0.6 nm oxide thickness.
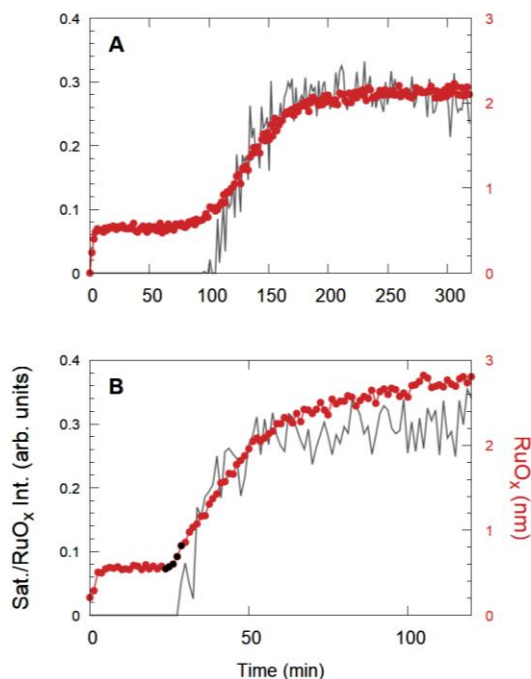
Figure S 4-9 Intensity of the rutile RuO_2 satellite XPS species (left axis) normalized to total Ru oxide for polished Ru(0001) at 420 °C at $1.2×10^{-4}$ mbar O_2 kept constant over five hours (A) and with a short increase to $5×10^{-4}$ mbar at the time points marked in black (B).
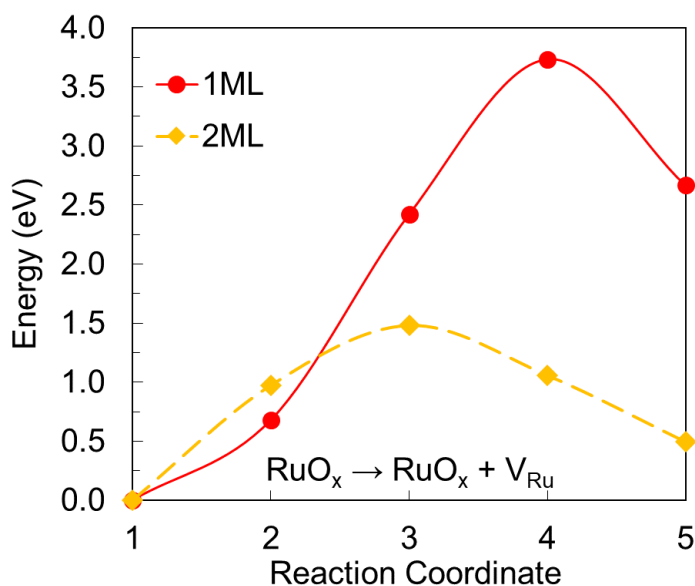
Figure S 4-8 Barriers for V_{Ru} formation on the 1 ML and 2 ML O-coverage surfaces.

5

Advanced oxidation of Ruthenium

5.1   Introduction

Metals are used in a broad range of applications for their mechanical, electrical, chemical, or catalytic properties. In many applications the metal surfaces are exposed to complex conditions such as reactive mixtures of different gases. In addition to the individual interaction of each molecule with the surface, the coexistence of different species can lead to synergy effects, making it difficult to understand the individual steps of surface-based processes such as catalytic reactions or surface degradation. One of the most common chemical reactions that results in the modification of surfaces is oxidation. The oxidation of metals has been extensively studied for a long time and a broad range of elements, both experimentally and theoretically[16,28,29,212]. Unraveling its mechanistic details often requires the use of model systems based on oriented single-crystal surfaces and high-purity gasses. Experiments at these idealized conditions provide information on the different adsorption sites and adsorption energies of oxygen at the metal surface. However, the relevance of these results to applications is sometimes questioned because they do not capture important aspects of the complexity of the material under application conditions.

The additional complexity of the conditions in industrial applications can be separated into two parts, the surface and the environment that the surface is exposed to. The surfaces in applications are usually polycrystalline, with randomly oriented crystal grains coexisting at the surface. Several different crystal planes are exposed at the surface, and each of them shows a characteristic interaction with the material's environment. Moreover, the grainy nature introduces a high density of extended defects such as step-edges and grain boundaries, which are not captured by studies on single crystalline model systems. An additional complexity is the gas environment under application conditions. While, in the example of metal oxidation, typical model studies only consider pure oxygen, the presence of other gas molecules in realistic environments complicates the single reaction to multiple simultaneously occurring reactions. One such example is water vapor, which when present can lead to the formation of hydroxides on the surface[53]. Other effects present in real environments are the interaction and reaction between multiple gasses, blocking of sites by contaminants, alternative reaction pathways, and surface modifications by different chemical reactions[17]. Therefore careful selection of experimental conditions to simulate realistic environments is necessary to assess whether the information from model studies is sufficient to understand the effects identified in application conditions[53].

In this chapter several aspects of application conditions are carefully selected to increase our understanding of their separate effect on surface oxidation. The oxidation of ruthenium is investigated with a focus on three aspects that are often

left unexplored, namely the details of XPS peak shapes in extended scan ranges, the effects of polycrystallinity on oxide thickness, and the effect of water as an alternative oxidant. The first part shows the role of loss features and background in the fitting of asymmetric peaks, improving the XPS fitting. The second part reports the oxide growth on polycrystalline ruthenium, resulting in thicker oxides than what would be expected from single crystals. And lastly, the H_2O exposure of pristine and pre-oxidized Ru single-crystal surfaces during *in situ* XPS measurements is shown, illustrating the complexity of surface oxidation and reduction with different oxidants as well as the role of radiation.

5.2   Methods

Clean Ru(0001) surfaces were prepared by annealing at 300°C in 10^{-4} mbar O_2, followed by 700°C in UHV for one hour. The absence of contaminants and residual oxygen was confirmed using XPS. The polycrystalline ruthenium films were deposited on Al_2O_3(0001) substrates by pulsed laser deposition (PLD) using a KrF excimer laser (Coherent Compex 201F, λ = 248 nm) in UHV. The substrate was positioned 55 mm from the PLD target. The depositions were performed at a laser fluence of 8.5 J/cm^2, a shot frequency of 10 Hz, and a spot size of 0.4 mm^2. With 20,000 deposition pulses a 30 nm thick ruthenium layer was deposited. After deposition, XPS showed no traces of oxygen contamination. With grazing incidence X-ray diffraction (Gi-XRD) the crystallite size was determined to be approximately 10 nm.

For the *in situ* experiments, the Ru(0001) crystals were stabilized at the desired temperature before introducing 1.2×10^{-4} mbar O_2 (Messer CAN-Gas O_2 5.0 (Purity 99.999%)) or H_2O vapor via a high-precision leak valve. The water was cleaned with three freeze-pump-thaw cycles and purity confirmed with a residual gas analyzer to confirm no contaminations from air, such as oxygen and nitrogen, were present. The XPS analysis was carried out with a HiPP-3 spectrometer using a monochromatic Al Kα source. The HiPP-3 analyzer is used with a 0.8 mm cone and a slit setting of 1.0 mm. XPS peak fitting is performed using KolXPD.

5

5.3   Results

5.3.1   XPS constraints on Ru 3d

X-ray photoelectron spectroscopy can be used to distinguish the metallic and oxidized phases of most elements, including the key element in this thesis, ruthenium. The interpretation of XPS spectra and the subsequent identification of different species rely on fitting data using suitable peak shapes and constraints. This is especially important for the asymmetric peak shape of the Doniach-Sunjic line shape [123,125], here convoluted with a Gaussian curve (DS-G), which is used for metallic materials like ruthenium and its oxide. This peak shape has a long asymmetric tail to higher binding energies. Together with electron energy loss peaks close to the main core level features (see chapter 3 starting on page 41), this tail gives rise to different approaches to set the background in XPS fits. A close look at an extended binding energy range can thus allow for the identification of additional peaks that can modify the background and thus also the total measured intensities.
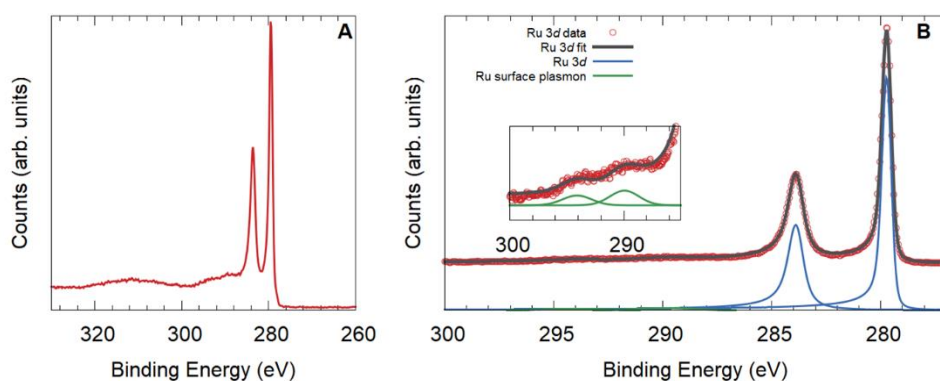
Figure 5-1 XPS spectrum of clean Ru(0001). (A) shows a large binding energy range, (B) shows the peak fitting species for Ru metal and the Ru surface plasmon.

Usually, Ru 3d spectra are reported with a binding energy range of 278 eV to 290 eV[46,82,84,103], implicitly assuming that the signal intensity at 290 eV has returned to the background level. Plasmon loss features, however, contribute to the signal at 290 eV, introducing a small discrepancy in the estimation of the background. Figure 5-1 A shows a Ru 3d spectrum of clean Ru(0001) with a binding energy range of 260 eV to 330 eV, illustrating that the background level at 290 eV is higher than at 300 eV. Figure 5-1 B shows a longer than regular region of a Ru 3d XPS spectrum of clean Ru(0001). The characteristic asymmetric peaks of Ru $3d_{5/2}$ and $3d_{3/2}$ are visible and identifiable in this figure. In the higher binding energy region in the zoomed-in inset, two additional peaks are identified at +10.2 eV from Ru $3d_{5/2}$ and $3d_{3/2}$. The peak distance is in agreement with EELS measurements on Ru, reporting a surface plasmon loss feature of 9.6 eV[170]. Acquiring the longer range of the Ru 3d region allows for fitting the background subtraction to the background at 300 eV and not

on top of these peaks at 290 eV. As the background is adjusted, the asymmetry of the ruthenium peaks can be increased without overestimating the intensity at high binding energies, leading to an improved fit. As the asymmetric tail of the peak shape extends a long range towards higher binding energies, it contributes substantially to the total area of the Ru peak. Assigning the measured intensity to the appropriate peaks can thus increase in the accuracy of the asymmetry fitting parameter and the Ru peak area.

To determine the effect on the peak fitting result of the optimized fitting parameters of the Ru 3d long range, they were compared using the same data while cropping the binding energy ranges to different values. The more commonly used short range extends from 277 eV to 290 eV, and the long range from 277 eV to 302 eV. Two sets of peak fitting parameters are defined, named "standard" and "extended" for short and long ranges, respectively. Table 5-1 shows these parameters for metallic ruthenium, ruthenium oxide annotated as RuO_x, the rutile RuO_2 satellite, and the surface plasmon of metallic ruthenium. As the main peak for the intermediate ruthenium oxide and rutile RuO_2 have been reported in the same position [82–84], they are defined as a single RuO_x peak. In contrast, the rutile RuO_2 satellite is specific for the rutile RuO_2 phase[82,84,85]. The values provided for the peak widths are their full widths at half maximum. As the extended range accounts for the presence of the surface plasmon peaks and the standard range cannot, the peak fitting parameters for the other species are deviating. The main difference for the species within both parameter sets is the asymmetry factor.

A contribution to this difference between the spectra ending at 290 eV BE and at 302 eV BE is the intensity at which the perceived background is placed. A significantly higher background intensity is present at the shorter spectrum, and the asymmetric tail of the peak shape is more prominent at the end of the short range. While the intensity of the tail is diminished with increasing distance from the main peaks, the background drops even faster because the short-range background overlaps with the additional plasmon loss peaks which are only clearly identified in the longer spectrum. As a result, a higher asymmetry parameter that better reproduces the shape of the main peak can be fitted for the extended range of data.

5

Table 5-1 XPS peak fitting parameters for extended and standard range.

	Extended				Standard		
	Ru	RuO$_x$	RuO$_2$ satellite	Surface Plasmon	Ru	RuO$_x$	RuO$_2$ satellite
Peak shape	DS-G	DS-G	Voigt	Voigt	DS-G	DS-G	Voigt
3d$_{5/2}$							
Position (eV)	279.80	280.48	282.38	290.02	279.80	280.48	282.50
Lorentzian width (eV)	0.12	0.2	0.2	0.0	0.19	0.2	0.2
Lorentzian asymmetry (eV)	0.09	0.13	-	-	0.04	0.13	-
Gaussian width (eV)	0.42	0.6	1.5	3.0	0.37	0.47	1.5
3d$_{3/2}$							
Position (eV)	283.96	284.64	286.54	294.18	283.97	284.65	286.67
Lorentzian width (eV)	0.57	0.7	0.7	0.0	0.7	0.7	0.7
Lorentzian asymmetry (eV)	0.09	0.13	-	-	0.029	0.13	-
Gaussian width (eV)	0.42	0.8	1.5	3.0	0.37	0.47	1.5

5

The increased asymmetry parameter for the extended range increases the peak area of the Ru 3d level, which can impact the relative contributions of Ru metal and oxidized components and result in different interpretations of surface composition and oxide layer thickness. Table 5-2 shows the RuO$_x$ and RuO$_2$ satellite percentages fitted with the corresponding binding energy ranges and peak fitting parameter sets. The ratios are consistent between the different parameter sets. Only for the thick oxide a higher RuO$_2$ satellite intensity is seen for the extended range parameter set. The increase of the RuO$_2$ satellite would indicate an increased presence of the RuO$_2$ in the rutile phase in relation to the quantity of the intermediate ruthenium oxide species. As the ratio between satellite to oxide peak area changes from 16.8% to 27.0%, this would need to be carefully compared with the same parameters, otherwise a factor 2 difference in rutile RuO$_2$ presence could be reported. Thus, while the differences identified using the presented peak fitting parameters are very subtle, they can significantly impact the results in specific cases, for example for questions related to the content of rutile oxide in the surface region.

Table 5-2 Ru 3d peak fitting ratios of atomic species of different parameter sets and ruthenium surfaces.

	Ru(0001)	Thin oxide	Thick oxide
Extended range	0.0% RuO$_x$	13.4% RuO$_x$	42.9% RuO$_x$ 11.6% RuO$_2$ satellite
Standard range	0.0% RuO$_x$	13.4% RuO$_x$	43.8% RuO$_x$ 7.4% RuO$_2$ satellite

While the effect of using the extended measurement range is limited for the interpretation of the details of the Ru 3d spectrum itself, the changes in background level and area of the asymmetric peaks can significantly affect the contribution of Ru to the calculated surface composition. For oxidation studies, the ratio of oxygen to ruthenium is relevant, as it reflects the stoichiometry and serves as indicator for the presence of possible additional oxygen species. Table 5-3 shows the ratio of oxygen per RuO$_x$ and RuO$_2$ satellite from the two different approaches, while accounting for cross sections. With this, a decrease is identified in the ratio of O/(RuO$_x$+RuO$_2$ satellite) for the extended range. The resulting value of the extended range is closer in stoichiometry to the expected RuO$_2$ oxide, demonstrating a clear advantage of using the extended range for characterizing surface composition.

Table 5-3 Atomic ratios of oxygen per ruthenium oxide and ruthenium oxide satellite of different parameter sets and ruthenium surfaces.

(oxygen) per (RuO$_x$+RuO$_2$ satellite)	Ru(0001)	Thin oxide	Thick oxide
Extended range	0.00	2.58	2.82
Standard range	0.00	3.32	3.44

5.3.2 Thermal oxidation of polycrystalline ruthenium

Metal surfaces in applications are often polycrystalline in nature, consisting of crystalline grains of different orientations exposing different crystallographic planes. In principle, each of the individual facets of the crystallites can be understood using knowledge from model studies on single crystals. While it is tempting to believe that the behavior of a polycrystalline surface can simply be explained as the superposition of small single crystalline contributions, most processes at polycrystalline surfaces remain more complex than that[41]. The case of oxidation of polycrystalline surfaces involves for example the effects of surface roughness, proximity of different orientations, and grain boundaries. While the Cabrera-Mott oxide growth model accounts for one-dimensional diffusion[16], the crystal orientations of polycrystalline surfaces can be slanted, resulting in one-dimensional growth at different angles to the assumed surface, which would be perceived as a thicker oxide layer by several methods measuring at a perpendicular angle. Moreover, the effects of the interfaces between different grains can result in enhanced diffusion and even dominate surface modifications, but they are difficult to investigate[30,42,213]. Additionally, measuring the oxide growth on polycrystalline material introduces complexities such as the dependence on grain sizes and preferential orientation.

Even though these complexities illustrate the importance of connecting the knowledge from single-crystalline model systems to applied materials, comparisons of oxide growth on polycrystalline materials and single crystals of the same composition are scarce. The main examples include studies on Cr[214], Fe[215], and Ni[216], which all report an increased oxide thickness for polycrystalline material in comparison to single crystal surfaces. This additional oxide growth is attributed to the presence of grains and the corresponding grain boundary diffusion leading to an increased oxygen diffusion inwards [38,215,216]. Recent studies combining large crystallite sizes and high spatial resolution allow for insights on oxidation at the level of individual grains, for example for Rh[38], Pd[40], and W[39]. In these reports the oxide growth of the individual crystal orientation of the polycrystalline material matches their oxide growth expected from their respective single crystal model systems. However, the commonly studied low-index surfaces are not necessarily the ones dominating the oxide growth in the polycrystalline case. In the case of palladium, for example, the rarely studied Pd(310) orientation has shown a significantly thicker oxide layer than is expected from the (100) and (110) orientations. This thicker oxide layer is in agreement with an increased step density of this orientation[40]. For ruthenium, the material of choice for this chapter, comparative studies are lacking but the mechanisms are expected to be similar.

The oxidation of ruthenium has been studied in great detail using various methods, often using single-crystal model systems. For single crystal ruthenium with (0001)

orientation, no oxide formation is identified below 300°C, and at 350-400°C the growth of 2.6 nm of oxide is reported from standardized thermal oxidation[76,103]. For polycrystalline ruthenium an oxide thickness of 2.5 nm was reported at 200°C [46], a significantly thicker oxide than expected for single crystal ruthenium oxide. A more in depth overview of ruthenium oxidation is shown in chapter 1.4 Oxidation of ruthenium on page 19.

In this sub-chapter, a direct comparison of the thermal oxidation of polycrystalline and single crystalline ruthenium in (0001) orientation at the same parameters is provided using *in situ* XPS measurements, following the evolution of the oxygen presence as well as the oxidation state of ruthenium. With these measurements a similar oxide growth processes and increased oxide thicknesses for polycrystalline ruthenium is identified.

5.3.2.1   XPS verification

In an initial comparison, the XPS peak shapes of Ru(0001) and polycrystalline Ru layers free of contaminants were overlapped (Figure 5-2 A) to determine if the XPS peak fitting parameters are transferable from single crystal Ru(0001) to polycrystalline Ru. The peak fitting parameters of Ru(0001) (shown for example in section 5.3.1 XPS constraints on Ru 3d in Table 5-1 on page 80) also reproduce the polycrystalline Ru spectra very well. In Figure 5-2 B a partially oxidized polycrystalline Ru spectrum of Ru 3d is shown. In this spectrum the fit components attributed to ruthenium metal, ruthenium oxide (labeled as RuO$_x$), and the rutile RuO$_2$ satellite peak are present. Upon oxidation to a comparable oxygen content, the peak shape of the Ru 3d level shows no differences between polycrystalline and single crystalline Ru. Therefore the same peak fitting parameters are used for both types of samples.
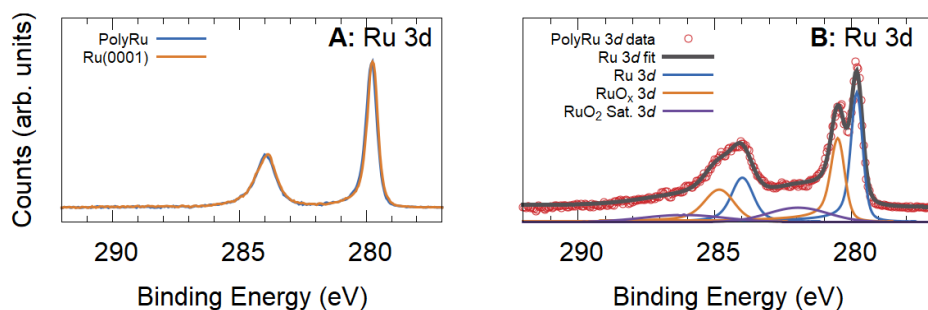
Figure 5-2 Ru 3d XPS spectrum. (A) clean polycrystalline ruthenium and single crystal Ru(0001), (B) partially oxidized polycrystalline ruthenium peak fitting with the species Ru, RuO$_x$, RuO$_2$ satellite.

5.3.2.2   Approximation for overlayers on polycrystalline surfaces

Estimating the thickness of an oxide layer on top of a polycrystalline surface spectroscopically is complex due to the conflict of simplifying approximations and imperfections of the layer, such as the surface roughness. Surface-sensitive techniques, such as XPS, are particularly affected by changes introduced by the coexistence of multiple grains of different orientations and shapes. When using XPS to calculate a layer thickness, typically a homogeneous flat layer is assumed to be grown on top of a homogeneous flat substrate, which is often suitable for single-crystal oxidation, see Figure 5-3 A. For polycrystalline layers, the approximation of a homogeneous flat oxide layer on a flat substrate may no longer provide an accurate description of the system, and a different model is needed to estimate the oxide thickness of a polycrystalline surface.

While idealized models fail to fully describe the case of an overlayer on a polycrystalline surface, they can provide limits for the maximum and minimum thickness corresponding to a measured signal. Here, two extreme overlayer models are used to determine the possible range of oxide overlayer thicknesses on a polycrystalline surface: the approximation of a flat surface and that of an assembly of core-shell particles of metal coated in oxide. While a polycrystalline surface is neither flat nor spherical, it is assumed to be rougher than a perfect plane, and flatter than an assembly of spherical nanoparticles, thus falling in between these extreme models. The core-shell approximation assumes a homogeneous oxide layer around a spherical metal core, see the image on the right side of the sketch in Figure 5-3 C[217]. The particle size decides on the relative contribution of the outer shell to the oxide-to-metal ratio. At the same measured oxide signal, smaller particles yield a thinner calculated oxide layer. The rightmost panel of Figure 5-3 D illustrates the calculated oxide thickness for different intensity ratios and particle size approximations. For larger particle sizes, the estimated oxide thickness increases, but the model is limited to nanometer to micrometer-sized particles and does not fully approach the value of the flat approximation at the maximum particle size [217].
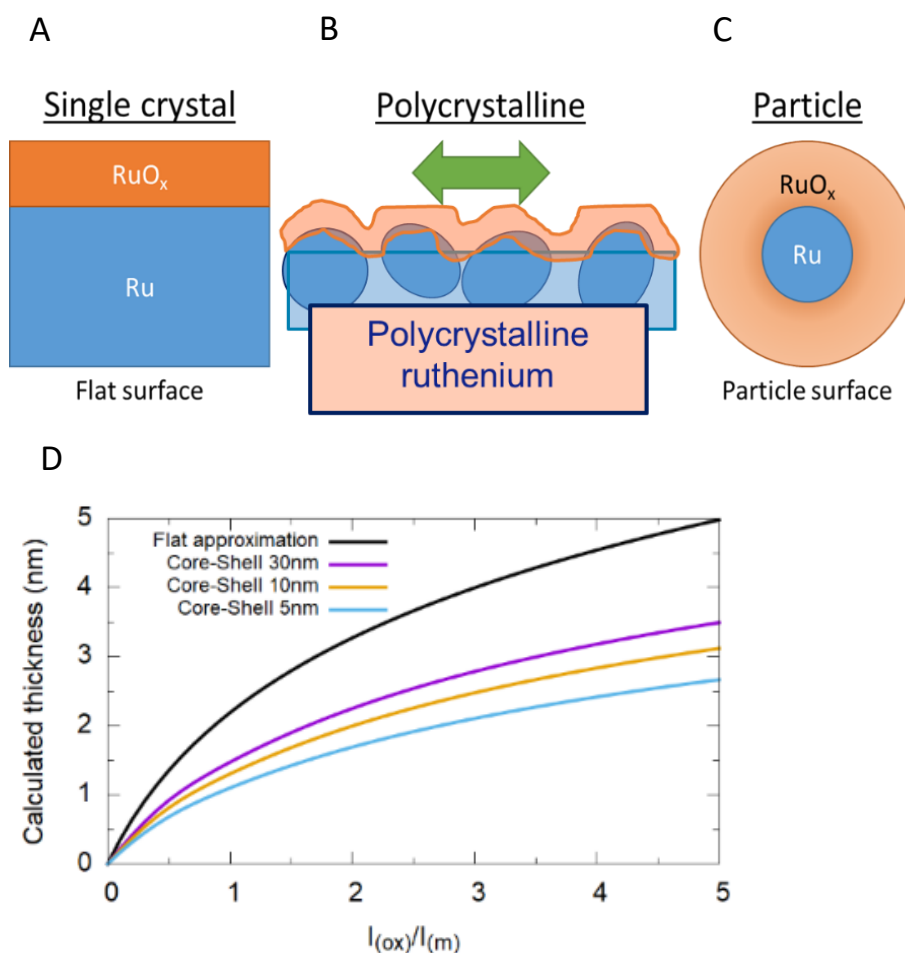
Figure 5-3 Schematic sketch of a ruthenium oxide layer on ruthenium surface (A), schematic depiction of an oxide layer on polycrystalline ruthenium (B), a core-shell oxide layer on ruthenium (C), approximated oxide thickness for different overlayer models (D).

5.3.2.3 Polycrystalline ruthenium: thermal oxidation

A time-dependent XPS study was conducted to follow the initial oxidation of polycrystalline ruthenium and compare it with results on single crystalline Ru(0001). Polycrystalline ruthenium films were deposited by pulsed laser deposition and transferred to the XPS measurement chamber without breaking vacuum. A series of consecutive *in situ* XPS spectra was recorded while exposing the polycrystalline ruthenium to 1.2×10^{-4} mbar O_2 at constant temperatures in the range from 280°C to 380°C.

The results of the thermal oxidation at 290°C are shown in Figure 5-4. Panel A shows the evolution of the ratio of oxygen per ruthenium during the exposure. An initial slow increment in the oxygen content is seen, followed by an accelerated increase in the O/Ru ratio at 20 minutes. This rapid growth of this ratio slows down after 35 minutes and approaches saturation after 70 minutes. In panel B, the respective calculated oxide thickness is shown, where the upper limit is based on the flat approximation and the lower limit is based on the core-shell approximation using an estimated particle size of 10 nm. The oxide thickness slowly increases and stabilizes between 1.5 nm and 2.5 nm after 70 minutes. In panel C the evolution of the individual species identified in XPS normalized by their corresponding cross sections are shown. For Ru 3d, the components attributed to ruthenium metal, ruthenium oxide (RuO_x), and the rutile RuO_2 satellite are identified. From the O 1s XPS spectra the oxygen in the oxide lattice is identified, Ox-Ru. A second oxygen species, commonly attributed to hydroxyl groups (OH-Ru), was observed at a low stable intensity and excluded from the graph. As the exposure to oxygen proceeds, a clear decrease of ruthenium metal is seen, and an increase of RuO_x and Ox-Ru is evident. After an initial step, the intensity of the Ox-Ru species shows a slow increment, followed by an accelerated increase after 14 minutes. At approximately 70 minutes the oxidation of ruthenium metal to ruthenium oxide is stabilized. While the ratio of Ox-Ru and RuO_x species converge to a constant value at the end, in the initial growth shows excess Ru in the oxide. The characteristic satellite feature for rutile RuO_2 emerges after 20 minutes and continues to increase until it saturates at a comparable time to the oxygen content and the RuO_x signal.

Figure 5-4 Thermal oxidation of polycrystalline ruthenium at 290°C in 1.2 × 10⁻⁴ mbar O₂. (A) atomic ratio of oxygen per ruthenium, (B) ruthenium oxide thickness approximated between thinnest (core-shell approximation) and thickest (flat surface approximation), (C) normalized intensity of species detected in XPS.

To determine the effect of temperature, the same type of polycrystalline ruthenium was exposed to 1.2×10^{-4} mbar O_2 at 340°C. Also at this higher temperature, the O/Ru ratio in Figure 5-5 A first rapidly increases to a small value that is stable for a short time, followed by a phase of accelerated growth and, finally, saturation. The respective calculated oxide thickness first reaches a brief metastable thickness plateau of 0.3 nm and 0.5 nm before growing to a final oxide thickness between 2.5 nm from the core-shell approximation and 4.5 nm from the flat approximation. The evolution of the individual Ru 3d species and the lattice oxygen Ox-Ru is shown in panel C. The oxide growth at 340°C shows a similar trend to the lower temperature, however with a higher final oxide thickness and a steeper growth curve in the initial growth phase at approximately 10 minutes. This transition from slow to fast growth is significantly more accentuated than at 290°C. Moreover, the appearance of the rutile RuO_2 satellite is more distinct, allowing for a clearer link to the evolution of the other species.

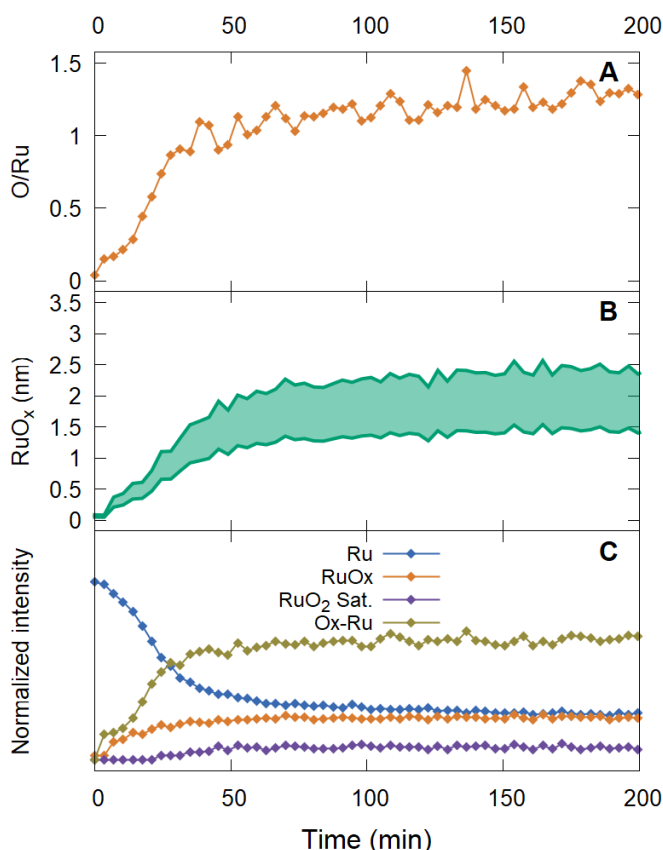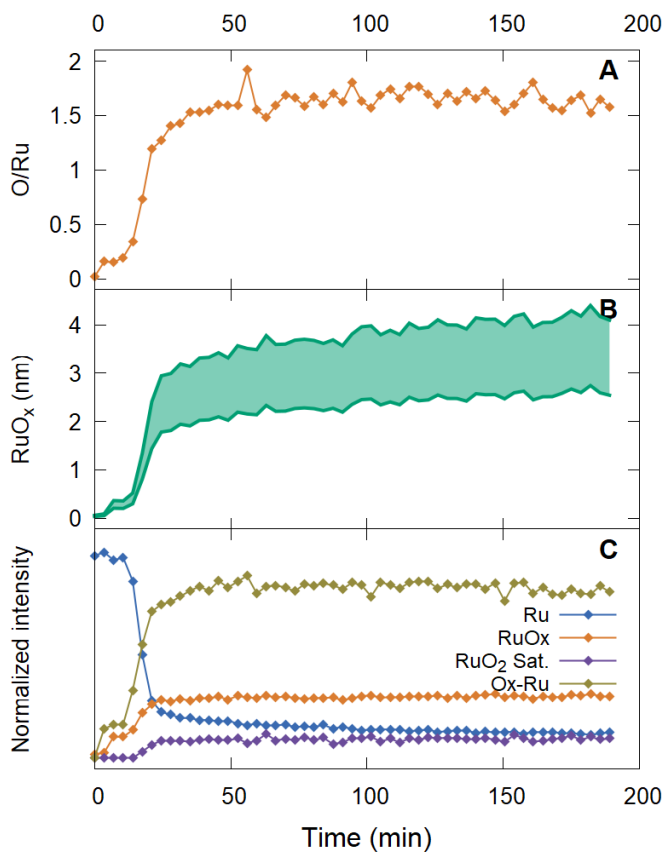*Figure 5-5 Thermal oxidation of polycrystalline ruthenium at 340°C in 1.2 × 10⁻⁴ mbar O₂. (A) atomic ratio of oxygen per ruthenium, (B) ruthenium oxide thickness approximated between thinnest (core-shell approximation) and thickest (flat surface approximation), (C) normalized intensity of species detected in XPS.*

To illustrate the similarities and differences between polycrystalline and single crystalline ruthenium, the thickness curves from Figure 5-4 and Figure 5-5 are compared to the time-dependent oxide thickness measured for a Ru(0001) single crystal surface (see also chapter 4 starting on page 57) in Figure 5-6. At both temperatures, the thinnest approximated oxide thickness for polycrystalline ruthenium is significantly thicker than the single crystal. The growth curves of the polycrystalline samples show quick growth followed by a slowed down increase in oxide thickness, whereas the single crystal oxide growth demonstrates only a slow growth process at low temperatures. However, it shows a similar growth at higher temperatures.
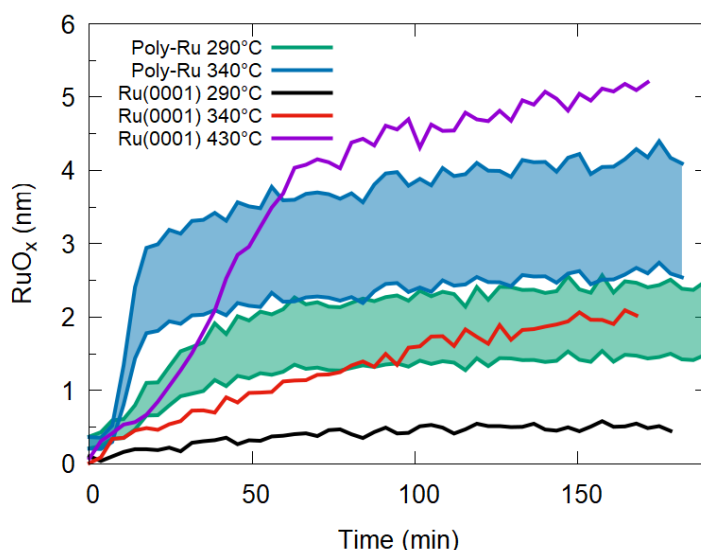
Figure 5-6 Oxide thickness compared for single crystal Ru(0001) at 290°C, 340°C, and 430°C, and polycrystalline ruthenium at 290°C and 340°C.

To obtain further insight into the phase of the forming oxide, it is instructive to relate the calculated oxide thickness to the intensity of the satellite peak at 282.4 eV, which is characteristic for RuO_2 with a rutile structure. This satellite is not observed at the onset of oxide formation and only seems to emerge upon exceeding a minimum thickness. At 290°C the RuO_2 satellite appears with an approximated thickness between 0.72 nm and 0.42 nm in the flat and core-shell approximations, respectively (see Figure 5-4). At the increased temperature of 340°C, the RuO_2 satellite intensity was first identified upon exceeding a thickness of 0.52 nm and 0.30 nm (Figure 5-5). The intensity ratio between the satellite and the oxide peak in Ru 3d in Figure 5-7 provides a measure of the degree of conversion towards rutile RuO_2. Polycrystalline ruthenium at 290°C shows the satellite peak emerging 17 minutes after starting exposure. The peak area ratio of the satellite and the main Ru oxide peak saturates

at approximately 0.3 after 40 minutes. At 340°C, processes are accelerated, shown by an initial satellite intensity after 10 minutes and a stabilized ratio of 0.3 already after 17 minutes. In comparison the conversion on the Ru single crystal is shifted to higher temperatures, showing no satellite intensity at 290°C and a slow increase after a delayed emergence at 340°C, approaching the value of 0.3 at around 150 minutes. The Ru single crystal at 430°C shows a similar increase in the satellite intensity as is seen for the polycrystalline Ru.
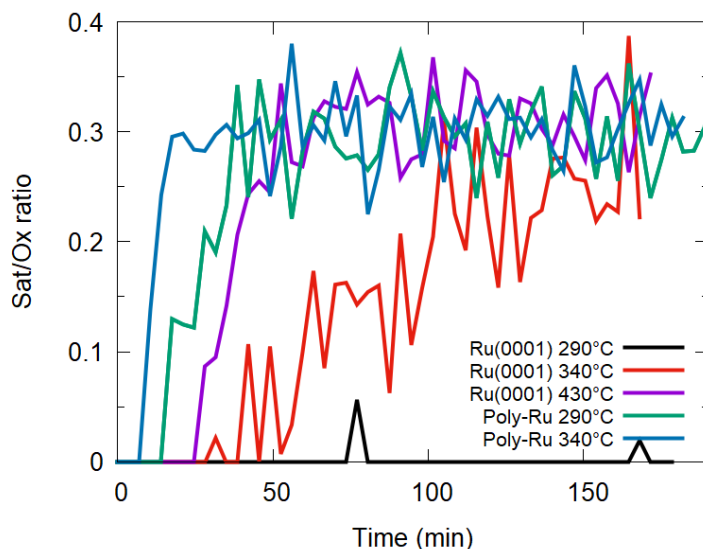
Figure 5-7 Intensity ratio of the rutile RuO₂ satellite per ruthenium oxide intensity from Ru 3d XPS spectra resolved in time for single crystalline Ru(0001) and polycrystalline ruthenium at 290°C and 340°C.

5.3.2.4 Discussion

In chapter 4 the initial oxidation of the single crystalline Ru(0001) surface is shown to follow a characteristic two-step oxide growth. In the present chapter it is demonstrated that this growth pattern also applies to polycrystalline ruthenium. First an initial oxide layer grows, followed by a slowing down of the oxide growth. After reaching a thickness threshold the oxide growth accelerates again, leading to a rapid increase in thickness before slowing down to approach saturation. This two-step oxidation indicates a kinetic hindrance of the growth at low thicknesses between approximately 0.3 and 0.7 nm, similar to the single crystalline case. This can be perceived by the same time-dependent slow-down and acceleration for the two different surfaces, even though the polycrystalline surface is not a homogeneous flat surface.

Previously reported comparisons of oxide thicknesses between polycrystalline and single crystalline materials have shown an increased oxide thickness on polycrystalline surfaces[214–216]. This matches well with our comparison for ruthenium[9,21]. The increased oxide thickness for polycrystalline Ru at the same conditions can find their origin in different properties of polycrystalline surfaces, for example the surface energy of different facets, differences in oxygen dissociation, roughness, or grain boundary diffusion. The surface energy is considered an unlikely explanation for the increased oxide thickness. The lowest surface energy plane for ruthenium is the (0001) orientation[218] which is therefore expected to be the most abundant surface for polycrystalline ruthenium. Similar oxide thicknesses have been reported for other low surface energy crystal orientations[65]. The oxide thickness can also be modified by the concentration of oxygen available for oxide formation, which is determined by the dissociation of oxygen on the surface and thus by the pressure, temperature, sticking probability, and surface area. The temperature and pressure are experimental parameters that were maintained the same for both types of samples. For the intermediate oxide phase, no dissociation of oxygen was reported in literature, however the dissociation of oxygen of this surface is expected to still occur. For the different orientations of RuO_2 the dissociation is indicated to be similar[219]. As a result, it is unlikely that the oxygen dissociation is the origin for the increased oxide thickness. Additionally, an increased surface area also results in a larger exposed area that will be oxidized. However, the real surface area is challenging to estimate, calling for approximations. For the extreme case of high surface area, the polycrystalline oxide surface is modelled with the core-shell approximation, which assumes a surface covered by spherical particles with an approximate size of 10 nm. The surface roughness of this hypothetical model is significantly higher than the experimentally obtained values for polycrystalline ruthenium films. Even in this high-roughness limit, the increased surface does not account for the thickness difference observed in Figure 5-6.

The remaining important difference between single crystals and polycrystalline surfaces is the existence of grains and grain boundaries in polycrystalline material. Grain boundaries have been reported to offer facilitated pathways of diffusion in comparison to a continuous bulk oxide[42]. The diffusion of oxygen along the boundaries proceeds with lower activation energy than the diffusion of oxygen through the oxide structure and is therefore expected to become active at lower temperatures[30]. Facilitated diffusion along the grain boundaries enables oxygen to more easily reach deeper layers to continue oxidation, which would normally be inaccessible for dense closed layers. This enhanced diffusion is a plausible explanation for the increased oxide thickness seen for polycrystalline material. The grain boundary diffusion as mechanism is well established in the literature, but quantitative characterization of the enhancement of diffusion remains elusive. Thus,

while it is a likely explanation, it is unclear if it is responsible for the full increase in oxide thickness[42,216].

5.3.3 Ruthenium and its oxides exposed to water vapor

The interaction of water with surfaces is relevant to a wide range of scientific fields, among which are electrochemistry, corrosion chemistry, heterogeneous catalysis, and physical chemistry[220]. The stability and dissociation of water molecules on surfaces, for example, is important for heterogeneous catalysis, where H_2O can take the role of a reactant or product[221]. Moreover, water can play the role of an oxidant, and its presence can affect the surface composition of materials. Furthermore, the presence of water during metal oxidation by oxygen can modify the oxidation mechanism and result in different kinetics and final oxide thicknesses[222].

One of the processes occurring in the presence of water is accelerated oxidation[53]. The differences between oxidation by oxygen and by water has been studied for a broad range of elements, for example Be[54,55], Al[56,223,224], Fe[222], Si[225] , and Pt-group metals[51]. The observed differences have been attributed to an increased initial sticking coefficient for water on beryllium which is expected to be similar for other elements[55], and a change in oxidation kinetics from inverse logarithmic in oxygen to parabolic in water. While this corresponds to a change in the oxidation mechanism from field-limited to diffusion-limited growth, both types result in the same type of oxide[54]. Aluminium exposed to water, on the other hand, forms a hydroxide layer[223]. At room temperature the oxidation of aluminium with oxygen has a limiting oxide thickness, whereas with water a parabolic oxide growth is reported[57].

Also for ruthenium, studies on the interaction of water on metal surfaces have been reported. The adsorption and dissociation of water on single crystalline ruthenium has been investigated by both experimental and theoretical studies of the Ru(0001) surface[226–229]. From DFT calculations the activation barrier for the dissociation of water on Ru(0001) is reported to be 0.8 eV/H_2O[230,231]. The precursor for dissociation is identified as rows of water absorbed along the [$2\bar{1}\bar{1}0$] crystal directions by STM with the support of DFT[232]. The dissociation products of H_2O on Ru(0001) are first OH + H, followed by additional dissociation step to form O + 2H[231]. Also XPS provides evidence of the dissociation product being OH groups[233,234]. The dissociation of water competes with its desorption from the surface and is thus deemed kinetically hindered. Additionally, beam-induced dissociation has been suggested to play a role in XPS and electron-beam-based experiments[234]. EUV-induced dissociation of water on ruthenium has also been reported[61,235].

The exposure of water to oxidized ruthenium, more specifically RuO_2, occurs during the oxygen evolution reaction. In this catalytic reaction H_2O is interacting with the surface of RuO_2 splitting water to form the product O_2. The dissociation of H_2O on RuO_2 is an important step in this reaction, which was calculated using DFT to understand the effect of the different orientations of rutile RuO_2 [219,236] as well as different surface coverages of water[237]. These studies have shown that the dissociation of water can occur at two active sites, namely the coordinatively unsaturated Ru site, and the oxygen bridge site, O_{br}. Since the surface density of these active sites differs for different crystallographic orientations, the tendency to dissociate water varies between facets of RuO_2, with a maximum for the (101) surface followed by the (110), (001), and (100) surface[219,236,237]. The dissociation ratio of water on rutile RuO_2 is calculated to be 50%, where 50% of the H_2O molecules is deprotonated and the nearest undercoordinated O_{br} site is protonated, forming $H_3O_2^-$ species resulting from deprotonation of two water molecules[238]. Evidence of water dissociation has been obtained using STM images, showing dimers of water readily deprotonating into rows of dissociated H_2O + OH[239]. However, according to Lobo *et al.*[240], defects are required to dissociate water and no dissociation is expected on perfect rutile RuO_2. When RuO_2 is exposed simultaneously to oxygen and water, the oxygen can hinder the dissociation of water[241].

Moreover, the presence of ionizing radiation during exposure to water vapor has been found to affect the oxidation of pristine ruthenium[242]. In an environment of 10^{-7} mbar H_2O with a localized electron beam, exposure resulted in an oxide thickness of 1-2 nm inside the beam area, whereas only 0.5 nm oxide thickness was reported outside this area[58,64,242]. The water dissociates under ionizing radiation and forms OH and H products with a small fraction of atomic oxygen[235]. The dissociation of water on ruthenium under ionizing radiation is suggested to be similar to electrochemical dissociation of oxygen on a ruthenium surface showing oxide growth[101]. Despite these studies on the interaction of water with surfaces, there are still open questions. In the thermal oxidation of ruthenium, for example, it is unclear how the presence of oxygen on the surface and different stoichiometry of oxygen/ruthenium films affect the oxidation.

In this sub-chapter, an *in situ* study of ruthenium and its oxides exposed to water vapor provides insight into the redox surface chemistry of water vapor on Ru(0001) surfaces with different levels of oxidation. NAP-XPS measurements of Ru(0001) in water pressures up to 1.2×10^{-4} mbar demonstrate a different response of different oxides to water exposure and a high sensitivity to small amounts of hydrogen during the dosing of water. The comparison to pre- and post-exposure XPS measurements without X-ray irradiation during water dosing show a significant effect of ionizing radiation.

5.3.3.1 Exposure of ruthenium to water vapor

To explore the effect of water on ruthenium, a clean Ru(0001) surface was exposed to 1.2×10^{-4} mbar H_2O (with a H_2 content corresponding to approximately 10^{-7} mbar). Figure 5-8 A and B show a comparison of the Ru $3d_{5/2}$ and O 1s XPS spectra of pristine Ru(0001) after cleaning, after water exposure at room temperature for 30 minutes, and at 300°C for 30 minutes during *in situ* XPS measurements. From the XPS spectra of clean Ru(0001) measured at room temperature, in red, the ruthenium metal peaks and no oxygen species are identified. After exposure to H_2O for 30 minutes at room temperature, Figure 5-8 A and B in blue, neither the formation of ruthenium oxide nor the emergence of oxygen species was identified.
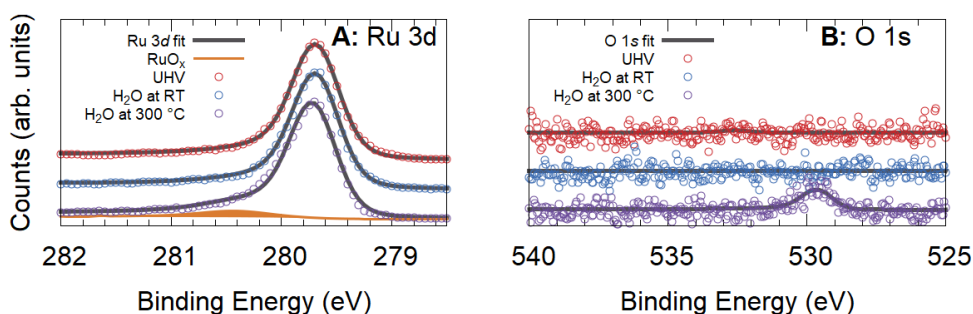
Figure 5-8 XPS spectra of Ru $3d_{5/2}$ (A) with fit results highlighting the emergence of the RuO$_x$ species in orange and O 1s (B) for Ru(0001) in its pristine state (red) and after exposure to 1.2×10^{-4} mbar H_2O at room temperature (blue, total dose of 2.2×10^5 Langmuir) and elevated temperature (purple).

Increasing the temperature to 300°C to identify possible thermal effects results in an increase in the oxygen content and a small oxide peak, shown in Figure 5-8 A and B in purple. The O/Ru ratio increased from 0.00 to 0.10. The peak positions of the new components in the O 1s and the Ru 3d regions correspond to the binding energies of ruthenium oxide (RuO$_x$, marked in orange in the Ru 3d region). This intensity of the Ru oxide peak corresponds to a calculated oxide thickness of 0.3 nm, using the approximation of a flat, homogeneous layer.

A possible explanation for this oxidation could be X-ray induced dissociation of water during the *in situ* XPS measurement, forming active oxygen species on the surface. To estimate the effect of X-rays, a reference experiment with similar exposure of Ru(0001) to 1.2×10^{-4} mbar H_2O at 340°C for 2 hours without X-rays has been conducted. In Figure 5-9 A and B, the Ru 3d and O 1s before and after exposure are shown, green and ochre, respectively. The O/Ru ratio increased from 0.03 to 0.05, but in the O 1s spectrum, no significant presence of the Ru oxide peak (530 eV) was detected. The other species at higher binding energy can be explained by adsorbed oxygen species on the surface. The post-exposure spectrum also shows finite intensity at 530.5 eV, but placing an additional component there in the peak fitting

process did not result in a component of finite intensity reproducing the datapoints. The signal to noise ratio in this spectrum is insufficient to reliably determine whether one or two peaks are present, which is why a single Voigt peak was used to obtain an estimate of the total intensity. From the Ru 3d spectra, no increase of RuO_x species was identified.
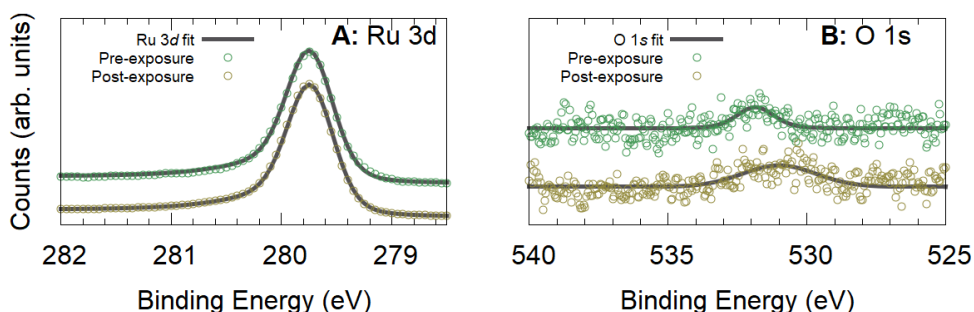
Figure 5-9 XPS spectra of Ru 3d (A) and O 1s (B) comparing unexposed Ru(0001) and H_2O exposed at elevated temperatures for an extended time without X-ray irradiation during H_2O exposure.

5.3.3.2   *In situ exposure of Ru(0001) to water vapor*

To evaluate the effect of water exposure as a function of temperature, Figure 5-10 shows the evolution of the O/Ru ratio (A), approximate Ru oxide thickness (C), and the oxygen peak components (D), following a temperature profile with a ramp from room temperature to 300°C, and a stepwise increase to approximately 700°C (B). During the ramp from 200°C to 300°C, a sharp increase in the O/Ru ratio was seen. This change was accompanied by the emergence of an oxide component in the Ru 3d spectra, corresponding to an increase in the calculated oxide thickness to 0.3 nm RuO_x. The increase of the corresponding lattice oxygen species in the O 1s region, Ox-Ru, coincides with the increase of RuO_x. As the temperature was increased above 400°C, a decrease of the O/Ru ratio was observed, which was also borne out by a small decrease in the calculated oxide thickness. The ratio of the Ox-Ru species to the RuO_x species, however, is maintained at the same value. As the temperature ramp reached 700°C, no difference was identified from the O/Ru ratio. However, the Ru oxide signal in the Ru 3d region decreased, leading to a drop in the calculated RuO_x thickness to <0.1 nm.
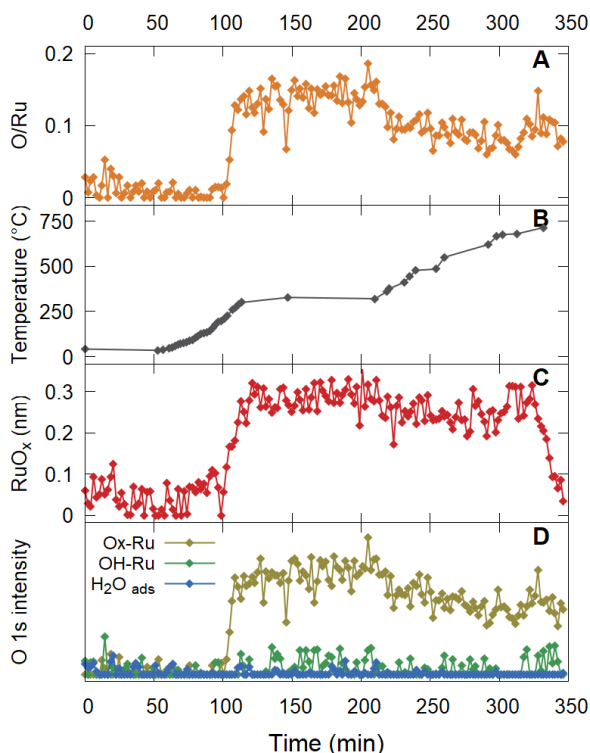
Figure 5-10 Time-dependent surface properties of single crystal Ru(0001) exposed to 1.2 × 10⁻⁴ mbar H₂O during a temperature ramp. (A) atomic ratio of oxygen per ruthenium, (B) temperature ramp of the sample, (C) ruthenium oxide thickness, (D) normalized intensity of O 1s species in XPS

5.3.3.3 Thin RuOₓ exposure to water vapor

Once a finite oxide layer thickness has been achieved on ruthenium, the further growth of Ru oxide is known to proceed autocatalytically with oxygen[243]. This peculiar behavior makes it particularly interesting to also test the interaction of oxidized Ru surfaces with a different oxidant such as water. In Figure 5-11 a thin oxide layer of 0.5 nm was grown on Ru(0001) in 1.2×10^{-4} mbar O_2. The time at this condition is indicated by the purple background, followed by pumpdown to UHV (white background) and exposure to 1.2×10^{-4} mbar H_2O (blue background). The individual panels display the evolution of the O/Ru ratio (A), the temperature (B), the approximate oxide thickness (C), and the intensities of the individual O 1s species (D). During the oxygen exposure, the O/Ru ratio, RuOₓ thickness, and Ox-Ru species show an initial increment and stabilize at values corresponding to a 0.5 nm thick RuOₓ layer. When changing from the exposure gas of 1.2×10^{-4} mbar O_2 to UHV, no change was identified in the oxide. However, after starting the H_2O exposure, a decrease was seen in the O/Ru ratio, reflecting a lower intensity of the Ox-Ru peak in the O 1s region. The oxide signal in the Ru 3d region also decreased, corresponding to a

change in the RuO$_x$ thickness from 0.5 nm to 0.3 nm. A reference experiment exposing this RuO$_x$ thickness to 10^{-6} mbar H$_2$ (corresponding to the upper limit of the increased H$_2$ background identified while dosing H$_2$O) at a comparable temperature shows the full reduction of the Ru oxide. The remaining oxide thickness after the water exposure is comparable to the oxide grown on pristine Ru in water vapor (Figure 5-10), showing that the system prefers this thickness for different starting points of the water exposure.

Figure 5-11 Time-dependent surface properties of single crystal Ru(0001) exposed to 1.2 × 10^{-4} mbar O$_2$ (purple region) growing approximately 0.5nm RuO$_x$, followed by 1.2 × 10^{-4} mbar H$_2$O (blue region). (A) atomic ratio of oxygen per ruthenium, (B) temperature of the sample, (C) ruthenium oxide thickness, (D) normalized intensity of O 1s species in XPS.

5.3.3.4   Thick RuO₂ exposure to water vapor

The thin oxide film is shown to reduce in H_2O vapor where trace amount of H_2 is present. The different structure and electronic properties of thicker Ru oxide layers discussed in Chapter 4 make it interesting to also investigate the interaction with water at a higher layer thickness. A Ru(0001) surface is exposed at 380°C to 1.2×10^{-4} mbar O_2, growing an approximately 2.4 nm thick oxide film, highlighted in Figure 5-12 by the purple background. The growth in oxygen is followed by pumpdown to UHV and exposure to 1.2×10^{-4} mbar H_2O at 150°C (blue background). The panels show the O/Ru ratio (A), the sample temperature (B), the approximated RuO_x thickness (C), and the intensity of the individual O 1s species (D) followed by XPS. Upon the exposure of Ru(0001) to O_2 at 380°C, an increment in the O/Ru ratio is seen and the calculated RuO_x thickness increases to 2.4 nm. From the O 1s XPS spectra, the majority of the oxygen measured is Ox-Ru. No change in the sample is apparent after returning to UHV. The temperature of the sample was decreased to 150°C to replicate the H_2O exposure for the thinner oxide. During 100 minutes of

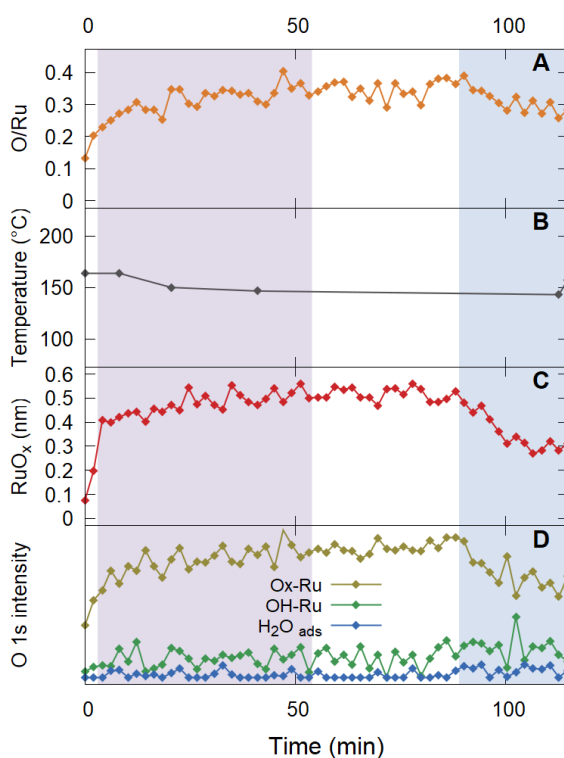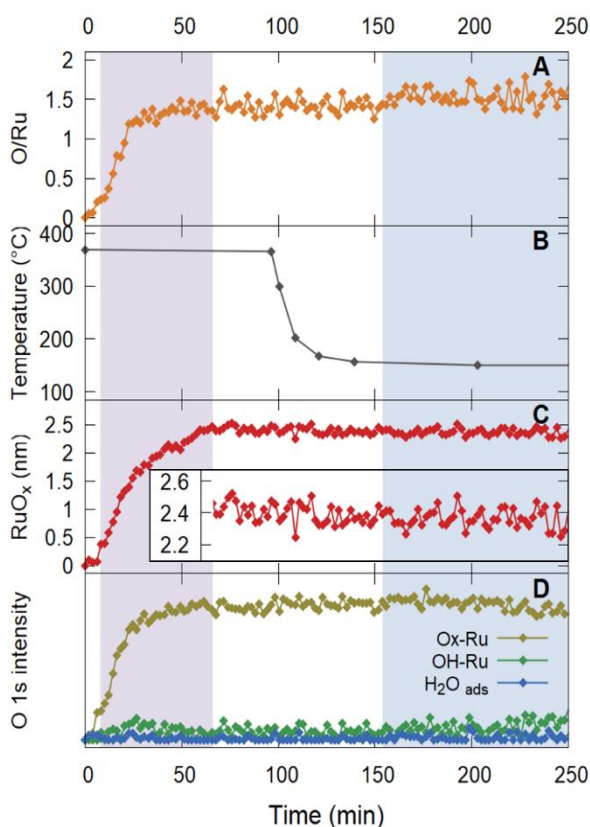*Figure 5-12 Time-dependent surface properties of single crystal Ru(0001) exposed to 1.2 × 10⁻⁴ mbar O₂ (purple region) growing approximately 2.4 nm RuOₓ, followed by 1.2 × 10⁻⁴ mbar H₂O (blue region). (A) atomic ratio of oxygen per ruthenium, (B) temperature of the sample, (C) ruthenium oxide thickness, (D) normalized intensity of O 1s species in XPS.*

H$_2$O exposure, no change was seen in the O/Ru, RuO$_x$ thickness, and the distribution of the individual O 1s species.

5.3.3.5   Discussion

The presented results on the effect of water vapor on Ru(0001) and two different types of ruthenium oxide overlayers on this surface confirm previous reports of weak interactions between ruthenium and water[101,237]. When exposing pristine Ru to water, a thin oxide layer is only observed to grow during simultaneous irradiation of the surface with X-rays. A thin Ru oxide layer was observed to partially reduce in water with a low hydrogen content, whereas a layer that is several nanometers thick appears stable during exposure to the same conditions. Reduction experiments at comparable pressures of pure hydrogen lead to a strong reduction of the thin Ru oxide layer.

X-rays have a clear enhancing effect on the oxidation of ruthenium in the presence of water, with no ruthenium oxide formation occurring without the additional activation by radiation. During irradiation of the sample, photoelectrons with characteristic energy and a large number of secondary electrons at lower energy are exiting from the surface. These electrons interact strongly with matter and can excite and activate the molecules in the sample's environment and facilitate their sticking and dissociation on the surface[234,244]. It has been previously reported that an electron beam or EUV light enhances the break-down of water and resulted in the oxidation of ruthenium[58,235,245]. The effects seen in electron-beam and EUV-based experiments are much stronger than those identified with X-ray radiation resulting in a thicker oxide layer[58]. However, part of this difference likely stems from the increased oxide thickness expected for a polycrystalline surface in comparison to the single crystal in our experiment. Further investigation on the difference between the X-ray-assisted oxidation of single crystalline and polycrystalline ruthenium surfaces would give additional insights into this effect.

In contrast to the weak oxidation of Ru metal by water, which follows reports from the literature, the reduction of a thin layer of ruthenium oxide in water vapor is an unexpected observation. While the *in situ* XPS data is clear and shows reduction of Ru in the Ru 3d spectra, together with a decrease in the oxygen content, this effect cannot be unambiguously assigned to water. From a residual gas analyzer measurement during the water exposures a H$_2$ partial pressure in the 10^{-7} mbar-range was identified. Exposure to pure hydrogen at the same temperature in 10^{-6} mbar led to full reduction of a comparable oxide layer, in line with literature reports on full reduction of 2.2 nm Ru oxide in 40 minutes at 10^{-6} mbar H$_2$ and

200°C[246]. Concluding from these experiments and literature examples the reduction of ruthenium oxide most likely originates from the hydrogen presence.

While the reduction in pure hydrogen indicates that water does not play a direct role in the reduction of the thin Ru oxide layer, the different stability for different oxide thicknesses is an intriguing observation, especially as no change is identified in UHV at the same temperatures. A possible explanation for the preferential reduction of the thin oxide compared to the thick oxide could be the difference in the oxide phase. The oxidation of ruthenium to rutile RuO_2 proceeds via the formation of an intermediate oxide, which converts to rutile RuO_2 oxide upon exceeding a critical thickness[22,73,103]. These two oxides can be distinguished in XPS spectra via a characteristic satellite peak for rutile RuO_2[85]. The relative contribution of this satellite peak to the total RuO_x signal provides an indication of the relative contents of intermediate oxide and bulk-like RuO_2. For the thin oxide films, no rutile RuO_2 satellite peak was present, indicating it to be predominantly in the intermediate oxide phase. Meanwhile, the thick oxide has a stable ratio of the rutile RuO_2 satellite peak to the RuO_x peak, matching to the values for the rutile RuO_2 oxide phase in chapter 4 for single crystalline and in Figure 5-7 for polycrystalline ruthenium. Reports of a metastable configuration as intermediate oxide[89,91,103] and a lower stability of disordered ruthenium oxide[52] are in line with the lower stability observed for the thin oxide layer. Even though the observed reduction is likely due to hydrogen rather than a direct effect of water, it highlights the changes that the initial RuO_2 layer undergoes as a function of thickness and their consequences for the stability of the oxide layers, which is also of interest for industrial applications[100].

The reduction of the thin oxide films exhibits peculiar features in itself, for example its slow-down after reaching an approximate thickness of 0.3nm, in contrast to the full reduction observed in pure hydrogen. The interplay between the water and the low hydrogen pressure could explain the stagnation of this reduction. A possible explanation for the limit of 0.3nm oxide thickness is the oxidation by water seen in the experiments in this sub-chapter. When no oxide is present the conditions cause oxidation to this level but not beyond. If this oxidation process is continuously on-going, also a simultaneous reduction process will not affect the final thickness significantly, provided that the oxidation is substantially faster.

At the highest temperature in Figure 5-10 the ruthenium oxide is reduced during water exposure. While the signature of RuO_2 disappears completely from the Ru 3d spectrum, surprisingly, the oxygen signal remains almost unchanged. No other elements are observed in survey spectra, making the possibility of an oxidized contaminant unlikely. Also the effect of changing peak shapes were considered, but the expected broadening at high temperature would rather result in an increased

5

RuO$_x$ intensity fitted which is contrary to the change witnessed. Adsorbed oxygen on the surface is also unlikely due to its desorption temperature from Ru(0001) between room temperature and 280°C[198,243] and the higher XPS binding energy expected for this species. The quantity of O/Ru would be in the approximate values of complete surface coverage by oxygen. In this O 1s spectrum, the oxide species are situated at the binding energy corresponding to the lattice oxide. Another possibility is the formation of a phase with a different oxidation state of Ru, such as ruthenium hydroxide. However, literature reports on ruthenium hydroxide place its Ru 3d$_{5/2}$ peak at 282.3 eV, where no intensity is identified, and other higher oxidation states are also not detected[82].

The present *in situ* study of the interaction of single crystalline ruthenium with water confirms general trends from the literature, reveals interesting differences between oxidized Ru surfaces, and points out challenges of experiments with water vapor. The weakly oxidizing nature of water makes experiments highly susceptible to trace amounts of other gas, which can affect the oxidation process and the equilibrium oxide thickness in water exposure. In agreement with prior reports, the presence of ionizing radiation, here X-rays, can result in dissociation of water and enhance the oxidizing properties of water. The exposure of ruthenium oxide layers of 0.5 nm and 2.4 nm reveals thickness-dependent differences in stability and supports the different nature of the oxide structure with thickness reported in Chapter 4. The results, however, leave several questions unanswered. For a more thorough understanding of the response of ruthenium and its oxides to water, the study would benefit from exposure at additional temperatures, generating deeper understanding of the reaction kinetics at the surface. Moreover, a thorough study of ruthenium hydroxides and ways to differentiate them from ruthenium metal and ruthenium oxides using surface science methods would be beneficial for the interpretation of the effects of water. In particular identifying characteristic features within XPS spectra, or with another technique that is applicable during the NAP-XPS measurements could help resolve the question whether a hydroxide is formed during the water exposure.

5.4   Conclusion

In conclusion, three less commonly studied aspects of the surface chemistry of ruthenium have been investigated to broaden the understanding of surface processes governing Ru oxidation and build a bridge between model systems and applications. In the first sub-chapter, the importance of the XPS measurement range and peak fitting parameters for improved determination of the chemical ratios and composition is pointed out. The second part compares the initial oxidation of polycrystalline and single crystalline ruthenium, and makes use of two approximations to emphasize that the higher oxide thicknesses for polycrystalline ruthenium is more than an effect of geometry. Finally, the investigation of water vapor as alternative oxidant for ruthenium single crystal surfaces in the third part confirms the expectation of weak interaction and reveals a complex dependence of the stable oxide thickness on gas composition and the oxide phase present at the surface.

5

Bibliography

1.   Cahan, D. *From Natural Philosophy to the Sciences*. (2003).

2.   D'Amore, J. J., Al-Abed, S. R., Scheckel, K. G. & Ryan, J. A. Methods for Speciation of Metals in Soils. *J Environ Qual* **34**, 1707–1745 (2005).

3.   Fu, N., Liu, Y., Ma, X. & Chen, Z. EUV Lithography: State-of-the-Art Review. *Journal of Microelectronic Manufacturing* **2**, 19020202 (2019).

4.   Fallica, R. *et al.* Absorption coefficient of metal- containing photoresists in the extreme ultraviolet. *Journal of Micro/Nanolithography, MEMS and MOEMS,* **17(2)**, 023505 (2018).

5.   Henke, B. L., Gullikson, E. M. & Davis, J. C. X-ray interactions: Photoabsorption, scattering, transmission, and reflection at E = 50-30, 000 eV, Z = 1-92. *At Data Nucl Data Tables* **54**, 181–342 (1993).

6.   Louis, E., Yakshin, A. E., Tsarfati, T. & Bijkerk, F. Nanometer interface and materials control for multilayer EUV-optical applications. *Prog Surf Sci* **86**, 255–294 (2011).

7.   Kanjilal, A., Catalfano, M., Harilal, S. S., Hassanein, A. & Rice, B. Time dependent changes in extreme ultraviolet reflectivity of Ru mirrors from electron-induced surface chemistry. *J Appl Phys* **111**, 063518 (2012).

8.   Narasimhan, A. *Mechanisms of EUV Exposure: Electrons and Holes*. (2017).

9.   Dolgov, A. *et al.* Comparison of H_2 and He carbon cleaning mechanisms in extreme ultraviolet induced and surface wave discharge plasmas. *J Phys D Appl Phys* **47**, 065205 (2014).

10.   King, D. L. A Fischer-Tropsch study of supported ruthenium catalysts. *J Catal* **51**, 386–397 (1978).

11.   Filot, I. A. W., Van Santen, R. A. & Hensen, E. J. M. The optimally performing Fischer-Tropsch catalyst. *Angewandte Chemie - International Edition* **53**, 12746–12750 (2014).

12.   Honkala, K. *et al.* Ammonia synthesis from first-principles calculations. *Science (1979)* **307**, 555–558 (2005).

13.   Hinrichsen, O., Rosowski, F., Muhler, M. & Ertl, G. The microkinetics of ammonia synthesis catalyzed by cesium-promoted supported ruthenium. *Chem Eng Sci* **51**, 1683–1690 (1996).

14. Bernasconi, R. & Magagnin, L. Review—Ruthenium as Diffusion Barrier Layer in Electronic Interconnects: Current Literature with a Focus on Electrochemical Deposition Methods. *J Electrochem Soc* **166**, D3219–D3225 (2019).

15. Wagner, C. Beitrag zur Theorie des Anlaufvorgangs. *Zeitschrift für Physikalische Chemie* **21B**, 25–41 (1933).

16. Cabrera, N. & Mott, N. F. Theory of the oxidation of metals. *Rep. Prog. Phys.* **12**, 163–184 (1949).

17. Fromhold, A. T. & Fromhold, R. G. Chapter 1 An Overview of Metal Oxidation Theory. *Comprehensive Chemical Kinetics* **21**, 1–117 (1984).

18. Atkins, P. & Paula, J. de. *Physical Chemistry*. *9th edition* (2010).

19. Smeltzer, W. W. & Young, D. J. Oxidation properties of transition metals. *Progress in Solid State Chemistry* **10**, 17–54 (1975).

20. Ribera, R. C. *Growth and Thermal Oxidation of Ru and ZrO$_2$ Thin Films as Oxidation Protective Layers*. (2017).

21. Dirksen, J. A. & Ring, T. A. Fundamentals of crystallization: Kinetic effects on particle size distributions and morphology. *Chem Eng Sci* **46**, 2389–2427 (1991).

22. Flege, J. I. & Grinter, D. C. In situ studies of oxide nucleation, growth, and transformation using slow electrons. *Prog Surf Sci* **93**, 21–45 (2018).

23. Herd, B., Knapp, M. & Over, H. Atomic scale insights into the initial oxidation of Ru(0001) using molecular oxygen: A scanning tunneling microscopy study. *Journal of Physical Chemistry C* **116**, 24649–24660 (2012).

24. Dignam, M. J. *The Kinetics of the Growth of Oxides*. *Electrochemical Materials Science* (1981).

25. Fromhold, a. T. Kinetics of Oxide film Growth on Metal Crystals: Electron Tunneling and Ionic Diffusion. *Physical Review* **158**, 600–612 (1967).

26. Martin, M. *Diffusion in Oxides*. *Diffusion in Condensed Matter: Methods, Materials, Models* (2005).

27. Gesmundo, F. The role of point defects in oxide scales in oxidation behaviour: A review. *Materials Science and Engineering* **87**, 243–250 (1987).

28.   Khanna, A. S. *High Temperature Oxidation*. *Handbook of Environmental Degradation of Materials: Second Edition* (Elsevier Inc., 2012).

29.   Gleeson, B. *Thermodynamics and Theory of External and Internal Oxidation of Alloys*. *Shreir's Corrosion* (2010).

30.   Atkinson, A. Transport processes during the growth of oxide films at elevated temperature. *Rev Mod Phys* **57**, 437–470 (1985).

31.   Xu, Z., Rosso, K. M. & Bruemmer, S. Metal oxidation kinetics and the transition from thin to thick films. *Physical Chemistry Chemical Physics* **14**, 14534–14539 (2012).

32.   Cai, N., Zhou, G., Müller, K. & Starr, D. E. Temperature and pressure dependent Mott potentials and their influence on self-limiting oxide film growth. *Appl Phys Lett* **101**, 171605 (2012).

33.   Zhou, G. & Yang, J. C. Initial oxidation kinetics of Cu(100), (110), and (111) thin films investigated by in situ ultra-high-vacuum transmission electron microscopy. *J Mater Res* **20**, 1684–1694 (2005).

34.   Shi, S. *et al.* Ambient Pressure X-ray Photoelectron Spectroscopy Study of Oxidation Phase Transitions on Cu(111) and Cu(110). *ChemPhysChem* **24**, e202300543 (2023).

35.   Reichel, F., Jeurgens, L. P. H. & Mittemeijer, E. J. The effect of substrate orientation on the kinetics of ultra-thin oxide-film growth on Al single crystals. *Acta Mater* **56**, 2897–2907 (2008).

36.   Bakradze, G., Jeurgens, L. P. H. & Mittemeijer, E. J. Oxide-film growth kinetics on Zr(0001) and Zr(1010) single-crystal surfaces. *Surface and Interface Analysis* **42**, 588–591 (2010).

37.   Bonfrisco, L. P. & Frary, M. Effects of crystallographic orientation on the early stages of oxidation in nickel and chromium. *J Mater Sci* **45**, 1663–1671 (2010).

38.   Trzcinski, M., Balcerowska-Czerniak, G. & Bukaluk, A. XPS studies of the initial oxidation of polycrystalline rh surface. *Catalysts* **10**, 617 (2020).

39.   Schlueter, K. & Balden, M. Dependence of oxidation on the surface orientation of tungsten grains. *Int J Refract Metals Hard Mater* **79**, 102–107 (2019).

40. Pfaff, S. *et al.* A Polycrystalline Pd Surface Studied by Two-Dimensional Surface Optical Reflectance during CO Oxidation: Bridging the Materials Gap. *ACS Appl Mater Interfaces* **16**, 444–453 (2024).

41. Kamins, T. I. & MacKenna, E. L. Thermal oxidation of polycrystalline silicon films. *Metallurgical and Materials Transactions B* **2**, 2292–2294 (1971).

42. Bastl, Z., Židů, J. & Roháček, K. Determination of the diffusion coefficient of aluminum along the grain boundaries of gold films by the surface accumulation method. *Thin Solid Films* **213**, 103–108 (1992).

43. Nánai, L., Vajtai, R. & George, T. F. Laser-induced oxidation of metals: State of the art. *Thin Solid Films* **298**, 160–164 (1997).

44. Tsuchiya, M., Sankaranarayanan, S. K. R. S. & Ramanathan, S. Photon-assisted oxidation and oxide thin film synthesis: A review. *Prog Mater Sci* **54**, 981–1057 (2009).

45. Ramanathan, S., Chi, D., McIntyre, P. C., Wetteland, C. J. & Tesmer, J. R. Ultraviolet-Ozone Oxidation of Metal Films. *J Electrochem Soc* **150**, F110 (2003).

46. Stilhano Vilas Boas, C. R., Sturm, J. M., van den Beld, W. T. E. & Bijkerk, F. Oxidation kinetics of transition metals exposed to molecular and atomic oxygen. *Materialia (Oxf)* **20**, 101203 (2021).

47. Zhukov, V., Popova, I. & Yates, J. T. Electron-stimulated oxidation of Al(111) by oxygen at low temperatures: Mechanism of enhanced oxidation kinetics. *Phys Rev B Condens Matter Mater Phys* **65**, 195409 (2002).

48. Gourrier, S. & Bacal, M. Review of Oxide Formation in a Plasma. *Plasma Chemistry and Plasma Processing* **1**, 217–232 (1981).

49. Kwon, M. S. & Lee, J. Y. O_2 plasma oxidation of sputter-deposited Cu thin film during photo resist ashing. *Appl Surf Sci* **135**, 101–106 (1998).

50. Böttcher, A. & Niehus, H. Formation of subsurface oxygen at Ru(0001). *Journal of Chemical Physics* **110**, 3186–3195 (1999).

51. Luo, H., Park, S., Yeung, H., Chan, H. & Weaver, M. J. Surface oxidation of platinum-group transition metals in ambient gaseous environments: Role of electrochemical versus chemical pathways. *Journal of Physical Chemistry B* **104**, 8250–8258 (2000).

52. Deka, N. *et al.* On the Operando Structure of Ruthenium Oxides during the Oxygen Evolution Reaction in Acidic Media. *ACS Catal* **13**, 7488–7498 (2023).

53. Saunders, S. R. J., Monteiro, M. & Rizzo, F. The oxidation behaviour of metals and alloys at high temperatures in atmospheres containing water vapour: A review. *Prog Mater Sci* **53**, 775–837 (2008).

54. Zalkind, S., Polak, M. & Shamir, N. The initial interactions of beryllium with O_2 and H_2O vapor at elevated temperatures. *Surf Sci* **601**, 1326–1332 (2007).

55. Zalkind, S., Polak, M. & Shamir, N. The adsorption of H_2O vs O_2 on beryllium. *Surf Sci* **385**, 318–327 (1997).

56. Zhu, D. *et al.* Effect of water vapor on high-temperature oxidation of NiAl alloy. *Corros Sci* **177**, 108963 (2020).

57. Ebinger, H. & Yates, J. Electron-impact-induced oxidation of Al(111) in water vapor: Relation to the Cabrera-Mott mechanism. *Phys Rev B Condens Matter Mater Phys* **57**, 1976–1984 (1998).

58. Bajt, S. *et al.* Oxidation resistance of Ru-capped EUV multilayers. *Emerging Lithographic Technologies IX* **5751**, 118–127 (2005).

59. He, Y. B. *et al.* Oxidation and reduction of ultrathin nanocrystalline Ru films on silicon: Model system for Ru-capped extreme ultraviolet lithography optics. *Journal of Physical Chemistry C* **111**, 10988–10992 (2007).

60. Over, H. *et al.* Long-term stability of Ru-based protection layers in extreme ultraviolet lithography: A surface science approach. *Journal of Vacuum Science & Technology B: Microelectronics and Nanometer Structures* **25**, 1123–1138 (2007).

61. Hollenshead, J. & Klebanoff, L. Modeling extreme ultraviolet∕H_2O oxidation of ruthenium optic coatings. *Journal of Vacuum Science & Technology B: Microelectronics and Nanometer Structures* **24**, 118–130 (2006).

62. Dolgov, A. *et al.* Plasma-assisted oxide removal from ruthenium-coated EUV optics. *J Appl Phys* **123**, 153301 (2018).

63. Bajt, S. *et al.* Design and performance of capping layers for extreme-ultraviolet multilayer mirrors. *Appl Opt* **42**, 5750 (2003).

64. Bajt, S. *et al.* Oxidation resistance and microstructure of ruthenium-capped extreme ultraviolet lithography multilayers. *Journal of Microlithography, Microfabrication and Microsystems* **5(2)**, 023004 (2006).

65. Over, H. Surface chemistry of ruthenium dioxide in heterogeneous catalysis and electrocatalysis: From fundamental to applied research. *Chem Rev* **112**, 3356–3426 (2012).

66. McCrory, C. C. L. *et al.* Benchmarking Hydrogen Evolving Reaction and Oxygen Evolving Reaction Electrocatalysts for Solar Water Splitting Devices. *J Am Chem Soc* **137**, 4347–4357 (2015).

67. Wintterlin, J. *et al.* Real-time STM observations of atomic equilibrium fluctuations in an adsorbate system: O/Ru(0001). *Surf Sci* **394**, 159–169 (1997).

68. Cai, J. Q., Luo, H. J., Tao, X. M. & Tan, M. Q. Initial Subsurface Incorporation of Oxygen into Ru(0001): A Density Functional Theory Study. *ChemPhysChem* **16**, 3937–3948 (2015).

69. Kim, Y. D., Seitsonen, A. P. & Over, H. Atomic geometry of oxygen-rich Ru(0001) surfaces: Coexistence of (1×1)O and RuO_2(110) domains. *Surf Sci* **465**, 1–8 (2000).

70. Orent, T. W. & Hansen, R. S. The interactions of nitric oxide and oxygen with Ru(10Ī0). *Surf Sci* **67**, 325–350 (1977).

71. Zhang, H. J., Lu, B., Li, H. Y., Bao, S. N. & He, P. Scanning tunneling microscopy and ultraviolet photoemission spectroscopy studies of oxygen adsorption on Ru(1 0 Ī 0). *Surf Sci* **556**, 63–68 (2004).

72. Blume, R., Niehus, H., Conrad, H. & Böttcher, A. Oxide-free oxygen incorporation into Ru(0001). *Journal of Chemical Physics* **120**, 3871–3879 (2004).

73. Herd, B. & Over, H. Atomic scale insights into the initial oxidation of Ru(0001) using atomic oxygen. *Surf Sci* **622**, 24–34 (2014).

74. Goritzka, J. C. *et al.* Insights into the gas phase oxidation of Ru(0001) on the mesoscopic scale using molecular oxygen. *Physical Chemistry Chemical Physics* **17**, 13895–13903 (2015).

75. Over, H., Seitsonen, A. P., Lundgren, E., Schmid, M. & Varga, P. Experimental and simulated STM images of stoichiometric and partially reduced RuO_2(1 1 0) surfaces including adsorbates. *Surf Sci* **515**, 143–156 (2002).

76. He, Y. B., Knapp, M., Lundgren, E. & Over, H. Ru(0001) model catalyst under oxidizing and reducing reaction conditions: In-situ high-pressure surface X-

ray diffraction study. *Journal of Physical Chemistry B* **109**, 21825–21830 (2005).

77. Over, H. *et al.* Atomic-scale structure and catalytic reactivity of the RuO$_2$(110) surface. *Science (1979)* **287**, 1474–1476 (2000).

78. Reuter, K. & Scheffler, M. Composition, structure, and stability of RuO$_2$(110) as a function of oxygen pressure. *Phys Rev B* **65**, 035406 (2001).

79. Kim, Y. D., Schwegmann, S., Seitsonen, A. P. & Over, H. Epitaxial Growth of RuO$_2$(100) on Ru(10$\bar{1}$0): Surface Structure and Other Properties. *J Phys Chem B* **105**, 2205–2211 (2001).

80. Zhang, H. J. *et al.* Growth of RuO2 thin layer on Ru(1 0 $\bar{1}$ 0) studied by scanning tunneling microscopy. *Surf Sci* **601**, 2297–2301 (2007).

81. Over, H. *et al.* Visualization of atomic processes on ruthenium dioxide using scanning tunneling microscopy. *ChemPhysChem* **5**, 167–174 (2004).

82. Morgan, D. J. Resolving ruthenium: XPS studies of common ruthenium materials. *Surface and Interface Analysis* **47**, 1072–1079 (2015).

83. Ernst, M. A. & Sloof, W. G. Unraveling the oxidation of Ru using XPS. *Surface and Interface Analysis* **40**, 334–337 (2008).

84. Foelske, A., Barbieri, O., Hahn, M. & Kötz, R. An X-ray photoelectron spectroscopy study of hydrous ruthenium oxide powders with various water contents for supercapacitors. *Electrochemical and Solid-State Letters* **9**, 268–272 (2006).

85. Over, H., Seitsonen, A. P., Lundgren, E., Smedh, M. & Andersen, J. N. On the origin of the Ru-3d$_{5/2}$ satellite feature from RuO$_2$(110). *Surf Sci* **504**, L196–L200 (2002).

86. Flege, J. I. *et al.* Nanoscale Origin of Mesoscale Roughening: Real-Time Tracking and Identification of Three Distinct Ruthenium Oxide Phases in Ruthenium Oxidation. *ACS Nano* **9**, 8468–8473 (2015).

87. Goriachko, A. & Over, H. The Nanostructuring of Atomically Flat Ru(0001) upon Oxidation and Reduction. *Nanoscale Res Lett* **11**, 534 (2016).

88. Böttcher, A., Krenzer, B., Conrad, H. & Niehus, H. Mesoscopic-scale growth of oxygen-rich films on Ru(0001) investigated by photoemission electron microscopy. *Surf Sci* **504**, 42–58 (2002).

89. Blume, R. *et al.* Identification of subsurface oxygen species created during oxidation of Ru(0001). *Journal of Physical Chemistry B* **109**, 14052–14058 (2005).

90. Flege, J. I., Hrbek, J. & Sutter, P. Structural imaging of surface oxidation and oxidation catalysis on Ru(0001). *Phys Rev B Condens Matter Mater Phys* **78**, 165407 (2008).

91. Reuter, K., Ganduglia-Pirovano, M. V., Stampfl, C. & Scheffler, M. Metastable precursors during the oxidation of the Ru(0001) surface. *Phys Rev B Condens Matter Mater Phys* **65**, 165403 (2002).

92. Reuter, K. & Scheffler, M. Atomistic description of oxide formation on metal surfaces : the example of ruthenium. *Chem Phys Lett* **352**, 311–317 (2002).

93. Knop-Gericke, A. *et al. Chapter 4 X-Ray Photoelectron Spectroscopy for Investigation of Heterogeneous Catalytic Processes*. *Advances in Catalysis* vol. 52 (Elsevier Inc., 2009).

94. Böttcher, A., Krenzer, B., Conrad, H. & Niehus, H. Mesoscopic-scale pattern formation induced by oxidation of Ru(0001). *Surf Sci* **466**, L811–L820 (2000).

95. Böttcher, A. *et al.* Spectral and spatial anisotropy of the oxide growth on Ru(0001). *Journal of Chemical Physics* **117**, 8104–8109 (2002).

96. Blume, R. *et al.* Monitoring in situ catalytically active states of Ru catalysts for different methanol oxidation pathways. *Physical Chemistry Chemical Physics* **9**, 3648–3657 (2007).

97. Blume, R., Christen, W. & Niehus, H. Reactivity of oxide precursor states on Ru(000l). *Journal of Physical Chemistry B* **110**, 13912–13919 (2006).

98. Y. B. He *et al.* Oxidation of Ir(111): From O-Ir-O Trilayer to Bulk Oxide Formation. *Journal of Physical Chemistry C* **112**, 11946–11953 (2008).

99. Weaver, J. F. Surface chemistry of late transition metal oxides. *Chem Rev* **113**, 4164–4215 (2013).

100. Shaikhutdinov, S. & Freund, H. J. Ultrathin oxide films on metal supports: Structure-reactivity relations. *Annu Rev Phys Chem* **63**, 619–633 (2012).

101. Herd, B., Goritzka, J. C. & Over, H. Room temperature oxidation of ruthenium. *Journal of Physical Chemistry C* **117**, 15148–15154 (2013).

102.   Kim, S. H. & Wintterlin, J. Morphology of RuO_2 (110) oxide films on Ru(0001) studied by scanning tunneling microscopy. *Journal of Chemical Physics* **131**, 064705 (2009).

103.   Diulus, J. T., Tobler, B., Osterwalder, J. & Novotny, Z. Thermal oxidation of Ru(0001) to RuO_2(110) studied with ambient pressure x-ray photoelectron spectroscopy. *J Phys D Appl Phys* **54**, 244001 (2021).

104.   Ernst, M. A. UV and electron-assisted oxidation of Al and Ru. (2009).

105.   Li, Z. *et al.* Flatband voltage shift of ruthenium gated stacks and its link with the formation of a thin ruthenium oxide layer at the ruthenium/dielectric interface. *J Appl Phys* **101**, 034503 (2007).

106.   Oura, K., Lifshits, V. G., Saranin, A. A., Zotov, A. V. & Hatayama, M. *Surface Science - An Introduction*. (2003).

107.   Stevie, F. A. & Donley, C. L. Introduction to x-ray photoelectron spectroscopy. *Journal of Vacuum Science & Technology A: Vacuum, Surfaces, and Films* **38**, 063204 (2020).

108.   Baer, D. R. *et al.* Introduction to topical collection: Reproducibility challenges and solutions with a focus on guides to XPS analysis. *Journal of Vacuum Science & Technology A: Vacuum, Surfaces, and Films* **39**, 021601 (2021).

109.   Moulder, J. F., Stickle, W. F., Sobol, P. E. & Bomben, K. D. *Handbook of X-Ray Photoelectron Spectroscopy*. (1992).

110.   Hofmann, S. *Auger- and X-Ray Photoelectron Spectroscopy in Materials Science*. (2013).

111.   Matsuda, H. & Matsui, F. 90°-deflection imaging electron analyzer for measuring wide 2D angular distribution and perpendicular spin texture. *J Electron Spectros Relat Phenomena* **245**, 147001 (2020).

112.   Seah, M. P. & Dench, W. A. Quantitative electron spectroscopy of surfaces: A standard data base for electron inelastic mean free paths in solids. *Surface and Interface Analysis* **1**, 2–11 (1979).

113.   Shokr, Y. *Interaction Mechanisms and Magnetization Dynamics in Ultrathin Antiferromagnetic Films and Their Correlation with Structure and Morphology*. *Thesis* (2016).

114.   Powell, C. J. Practical guide for inelastic mean free paths, effective attenuation lengths, mean escape depths, and information depths in x-ray

photoelectron spectroscopy. *Journal of Vacuum Science & Technology A: Vacuum, Surfaces, and Films* **38**, 023209 (2020).

115. Shard, A. G. Practical guides for x-ray photoelectron spectroscopy: Quantitative XPS. *Journal of Vacuum Science & Technology A: Vacuum, Surfaces, and Films* **38**, 041201 (2020).

116. Yeh, J. J. & Lindau, I. Atomic subshell photoionization cross sections and asymmetry parameters: $1 \leqslant Z \leqslant 103$. *At Data Nucl Data Tables* **32**, 1–155 (1985).

117. Greczynski, G. & Hultman, L. X-ray photoelectron spectroscopy: Towards reliable binding energy referencing. *Prog Mater Sci* **107**, 100591 (2020).

118. Bagus, P. S., Nelin, C. J. & Brundle, C. R. Chemical significance of x-ray photoelectron spectroscopy binding energy shifts: A Perspective. *Journal of Vacuum Science & Technology A* **41**, 068501 (2023).

119. Måtensson, N. & Nilsson, A. On the origin of core-level binding energy shifts. *J Electron Spectros Relat Phenomena* **75**, 209–223 (1995).

120. Fuggle, J. C. & Alvarado, S. F. Core-level lifetimes as determined by x-ray photoelectron spectroscopy measurements. *Phys Rev A (Coll Park)* **22**, 1615–1624 (1980).

121. Krause, M. O. & Oliver, J. H. Natural widths of atomic K and L levels, Ka X-ray lines and several KLL Auger lines. *J Phys Chem Ref Data* **8**, 329–338 (1979).

122. Omicron NanoTechnology. *EA 125 Energy Analyser User's Guide*. vol. 49 (2002).

123. Major, G. H. *et al.* Practical guide for curve fitting in x-ray photoelectron spectroscopy. *Journal of Vacuum Science & Technology A: Vacuum, Surfaces, and Films* **38**, 061203 (2020).

124. Olivero, J. J. & Longbothum, R. L. Empirical Fits to the Voigt Line Width. *J. Quant. Spectrosc. Radiat. Transfer* **17**, 233–236 (1977).

125. Doniach, S. & Sunjic, M. Many-electron singularity in X-ray photoemission and X-ray line spectra from metals. *Journal of Physics C: Solid State Physics* **3**, 285–291 (1970).

126. Biesinger, M. C. Advanced analysis of copper X-ray photoelectron spectra. *Surface and Interface Analysis* **49**, 1325–1334 (2017).

112

127. Grosvenor, A. P., Kobe, B. A., Biesinger, M. C. & McIntyre, N. S. Investigation of multiplet splitting of Fe 2p XPS spectra and bonding in iron compounds. *Surface and Interface Analysis* **36**, 1564–1574 (2004).

128. Engelhard, M. H., Baer, D. R., Herrera-Gomez, A. & Sherwood, P. M. A. Introductory guide to backgrounds in XPS spectra and their impact on determining peak intensities. *Journal of Vacuum Science & Technology A: Vacuum, Surfaces, and Films* **38**, 063203 (2020).

129. Salmeron, M. & Schlögl, R. Ambient pressure photoelectron spectroscopy: A new tool for surface science and nanotechnology. *Surf Sci Rep* **63**, 169–199 (2008).

130. Ogletree, D. F. *et al.* A differentially pumped electrostatic lens system for photoemission studies in the millibar range. *Review of Scientific Instruments* **73**, 3872 (2002).

131. Kim, Y. J., Gao, Y. & Chambers, S. A. Core-level X-ray photoelectron spectra and X-ray photoelectron diffraction of RuO_2(110) grown by molecular beam epitaxy on TiO_2(110). *Appl Surf Sci* **120**, 250–260 (1997).

132. Jablonski, A. & Zemek, J. Overlayer thickness determination by XPS using the multiline approach. *Surface and Interface Analysis* **41**, 193–204 (2009).

133. Tanuma, S., Powell, C. J. & Penn, D. R. Calculations of electron inelastic free paths. *Surface and Interface Analysis* **21**, 165–176 (1994).

134. Burkov, A. T. Silicide Thermoelectrics: Materials for Energy Harvesting. *Physica Status Solidi (A) Applications and Materials Science* **215**, 1800105 (2018).

135. Tomczak, J. M. Thermoelectricity in correlated narrow-gap semiconductors. *Journal of Physics Condensed Matter* **30**, 183001 (2018).

136. Lenssen, D. *et al.* Structural, electrical and optical characterization of semiconducting Ru2Si3. *Microelectron Eng* **50**, 243–248 (2000).

137. Susz, C. P., Muller, J., Yvon, K. & Parthé, E. Diffusionless phase transformations of Ru_2Si_3, Ru_2Ge_3 and Ru_2Sn_3 II: electrical and magnetic properties. *Journal of The Less-Common Metals* **71**, P1–P8 (1980).

138. Buschinger, B. *et al.* RuSi: Metal-semiconductor transition by change of structure. *J Alloys Compd* **262–263**, 238–242 (1997).

139. Vescoli, V. *et al.* The optical properties of RuSi: Kondo insulator or conventional semiconductor? *Solid State Commun* **105**, 367–370 (1998).

140. Melngailis, I. Small bandgap semiconductor infrared detectors. *J Lumin* **7**, 501–523 (1973).

141. Lenssen, D. *et al.* Growth and structural characterization of semiconducting Ru_2Si_3. *J Lumin* **80**, 461–465 (1999).

142. Souptel, D., Behr, G., Ivanenko, L., Vinzelberg, H. & Schumann, J. Floating zone growth and characterization of semiconducting Ru_2Si_3 single crystals. *J Cryst Growth* **244**, 296–304 (2002).

143. Borisenko, V. E. *Semi-Conducting Silicides*. (2000).

144. Pasquali, L., Mahne, N., Montecchi, M., Mattarello, V. & Nannarone, S. Formation and distribution of compounds at the Ru-Si(001) ultrathin film interface. *J Appl Phys* **105**, 044304 (2009).

145. Coloma Ribera, R., Van De Kruijs, R. W. E., Sturm, J. M., Yakshin, A. E. & Bijkerk, F. In vacuo growth studies of Ru thin films on Si, SiN, and SiO_2 by high-sensitivity low energy ion scattering. *J Appl Phys* **120**, 065303 (2016).

146. Petersson, C. S., Baglin, J. E. E., Dempsey, J. J., D'Heurle, F. M. & la Placa, S. J. Silicides of ruthenium and osmium: Thin film reactions, diffusion, nucleation, and stability. *J Appl Phys* **53**, 4866–4883 (1982).

147. D.J. Poutcharovsky & E. Parthe. The Orthorhombic Crystal Structure of Ru_2Si_3, Ru_2Ge_3, Os_2Si_3 and Os_2Ge_3. *Acta Cryst.* **B30**, 2692–2696 (1974).

148. Chang, Y. S. & Chu, J. J. The structure identification of epitaxial Ru_2Si_3 on (111) Si. *Mater Lett* **5**, 67–71 (1987).

149. Buschinger, B. *et al.* Preparation and low temperature properties of FeSi-type RuSi. *J Alloys Compd* **256**, 57–60 (1997).

150. Göransson, K., Engström, I. & Noläng, B. Structure refinements for some platinum metal monosilicides. *J Alloys Compd* **219**, 107–110 (1995).

151. Tam, P. L., Cao, Y. & Nyborg, L. XRD and XPS characterisation of transition metal silicide thin films. *Surf Sci* **606**, 329–336 (2012).

152. Calandra, C., Bisi, O. & Ottaviani, G. Electronic properties on silicon-transition metal interface compounds. *Surf Sci Rep* **4**, 271–364 (1985).

153. Egert, B. & Panzner, G. Bonding state of silicon segregated to -iron surfaces and on iron silicide surfaces studied by electron spectroscopy. *Phys Rev B* **29**, 2091–2101 (1984).

154. Verleysen, E., Bender, H., Richard, O., Schryvers, D. & Vandervorst, W. Characterization of nickel silicides using EELS-based methods. *J Microsc* **240**, 75–82 (2010).

155. Momma, K. & Izumi, F. VESTA 3 for three-dimensional visualization of crystal, volumetric and morphology data. *J Appl Crystallogr* **44**, 1272–1276 (2011).

156. Mortensen, J. J., Hansen, L. B. & Jacobsen, K. W. Real-space grid implementation of the projector augmented wave method. *Phys Rev B Condens Matter Mater Phys* **71**, 035109 (2005).

157. Enkovaara, J. *et al.* Electronic structure calculations with GPAW: A real-space implementation of the projector augmented-wave method. *Journal of Physics Condensed Matter* **22**, 253202 (2010).

158. Yan, J., Mortensen, J. J., Jacobsen, K. W. & Thygesen, K. S. Linear density response function in the projector augmented wave method: Applications to solids, surfaces, and interfaces. *Phys Rev B Condens Matter Mater Phys* **83**, 245122 (2011).

159. David, D. G. F., Godet, C., Johansson, F. O. L. & Lindblad, A. Quantitative analysis of plasmon excitations in hard x-ray photoelectron spectra of bulk black phosphorus. *Appl Surf Sci* **505**, 144385 (2020).

160. Liu, X. & Fan, H. Q. Theoretical studies on electronic structure and optical properties of Bi_2WO_6. *Optik (Stuttg)* **158**, 962–969 (2018).

161. Azam, S. *et al.* DFT study of the electronic and optical properties of ternary chalcogenides AlX_2Te_4. *Mater Res Express* **6**, 116314 (2019).

162. Prytz, Løvvik, O. M. & Taftø, J. Comparison of theoretical and experimental dielectric functions: Electron energy-loss spectroscopy and density-functional calculations on skutterudites. *Phys Rev B Condens Matter Mater Phys* **74**, 245109 (2006).

163. Hjorth Larsen, A. *et al.* The atomic simulation environment—a Python library for working with atoms. *Journal of Physics: Condensed Matter* **29**, 273002 (2017).

164. Blöchl, P. E. Projector augmented-wave method. *Phys Rev B* **50**, 17953–17979 (1994).

165. Perdew, J. P., Burke, K. & Ernzerhof, M. Generalized gradient approximation made simple. *Phys Rev Lett* **77**, 3865–3868 (1996).

166. Kurth, S., Perdew, J. P. & Blaha, P. Molecular and solid-state tests of density functional approximations: LSD, GGAs, and meta-GGAs. *Int J Quantum Chem* **75**, 889–909 (1999).

167. Hubbard, C. R., Swanson, H. E. & Mauer, F. A. A silicon powder diffraction standard reference material. *J Appl Crystallogr* **8**, 45–48 (1975).

168. Migas, D. B., Miglio, L., Shaposhnikov, V. L. & Borisenko, V. E. Structural, Electronic and Optical Properties of Ru_2Si_3, Ru_2Ge_3, Os_2Si_3 and Os_2Ge_3. *physica status solidi (b)* **231**, 171–180 (2002).

169. Jelenković, E. v., To, S., Blackford, M. G., Kutsay, O. & Jha, S. K. XPS and TEM study of deposited and Ru-Si solid state reaction grown ruthenium silicides on silicon. *Mater Sci Semicond Process* **40**, 817–821 (2015).

170. Surnev, L., Rangelov, G., Bertel, E. & Netzer, F. P. EELS studies of oxygen and sodium adsorption and coadsorption on Ru(001). *Surf Sci* **184**, 10–24 (1987).

171. Alvarez, J., Hinarejos, J. J., Michel, E. G., Castro, G. R. & Miranda, R. Electronic structure of iron silicides grown on Si(100) determined by photoelectron spectroscopies. *Phys Rev B* **45**, 14042–14051 (1992).

172. Asayama, K., Hashikawa, N., Kawakami, M. & Mori, H. High Accuracy and Resolution for the Separation of Nickel Silicide Polymorphs by Improved Analyses of EELS Spectra. *Microscopy of Semiconducting Materials 2007* **120**, 329–332 (2008).

173. Gallego, J. M., Alvarez, J., Hinarejos, J. J., Michel, E. G. & Miranda, R. The growth and characterization of iron silicides on Si(100). *Surf Sci* **251–252**, 59–63 (1991).

174. Parshin, A. S., Igumenov, A. Y., Mikhlin, Y. L., Pchelyakov, O. P. & Zhigalov, V. S. Reflection electron energy loss spectroscopy of structures based on silicon and transition metals. *IOP Conf Ser Mater Sci Eng* **255**, 012019 (2017).

175. Plusnin, N. I., Galkin, N. G., Lifshits, V. G. & Lobachev, S. A. Formation of interfaces and templates in the Si(111)-Cr system. *Surface Review and Letters* **2**, 439–449 (1995).

176. Fouda, A. N. & Eid, E. A. Effect of High-Temperature Annealing on Epitaxially Grown Ru Silicide Thin Films. *Silicon* **12**, 2387–2393 (2020).

116

177. Lizzit, S. *et al.* Transfer-free electrical insulation of epitaxial graphene from its metal substrate. *Nano Lett* **12**, 4503–4507 (2012).

178. Diebold, U., Li, S. C. & Schmid, M. Oxide surface science. *Annu Rev Phys Chem* **61**, 129–148 (2010).

179. Wöll, C. The chemistry and physics of zinc oxide surfaces. *Prog Surf Sci* **82**, 55–120 (2007).

180. Bliem, R. *et al.* Subsurface cation vacancy stabilization of the magnetite (001) surface. *Science (1979)* **346**, 1215–1218 (2014).

181. Zhang, J. *et al.* Cation vacancy stabilization of single-atomic-site $Pt_1/Ni(OH)_x$ catalyst for diboration of alkynes and alkenes. *Nat Commun* **9**, 1002 (2018).

182. Vogt, C. & Weckhuysen, B. M. The concept of active site in heterogeneous catalysis. *Nat Rev Chem* **6**, 89–111 (2022).

183. Kim, Y. D., Over, H., Krabbes, G. & Ertl, G. Identification of RuO_2 as the active phase in CO oxidation on oxygen-rich ruthenium surfaces. *Top Catal* **14**, 95–100 (2000).

184. Greeley, J. P. Active Site of an Industrial Catalyst. *Science (1979)* **336**, 810–811 (2012).

185. Jacques, S. D. M. *et al.* Dynamic X-Ray Diffraction Computed Tomography Reveals Real-Time Insight into Catalyst Active Phase Evolution. *Angewandte Chemie International Edition* **50**, 10148–10152 (2011).

186. Teschner, D. *et al.* Understanding Palladium Hydrogenation Catalysts: When the Nature of the Reactive Molecule Controls the Nature of the Catalyst Active Phase. *Angewandte Chemie International Edition* **47**, 9274–9278 (2008).

187. Kondrat, S. A. & van Bokhoven, J. A. A Perspective on Counting Catalytic Active Sites and Rates of Reaction Using X-Ray Spectroscopy. *Top Catal* **62**, 1218–1227 (2019).

188. Favaro, M., Xiao, H., Cheng, T., Goddard, W. A. & Crumlin, E. J. Subsurface oxide plays a critical role in CO_2 activation by Cu(111) surfaces to form chemisorbed CO_2, the first step in reduction of CO_2. *Proc Natl Acad Sci U S A* **114**, 6706–6711 (2017).

189.   Boden, D., Groot, I. M. N. & Meyer, J. Elucidating the Initial Oxidation of Pt(111) Using Large-Scale Atomistic Thermodynamics: A ReaxFF Study. *Journal of Physical Chemistry C* **126**, 20020–20027 (2022).

190.   Van Spronsen, M. A., Frenken, J. W. M. & Groot, I. M. N. Observing the oxidation of platinum. *Nat Commun* **8**, 429 (2017).

191.   Mistry, H. *et al.* Enhanced Carbon Dioxide Electroreduction to Carbon Monoxide over Defect-Rich Plasma-Activated Silver Catalysts. *Angewandte Chemie International Edition* **56**, 11394–11398 (2017).

192.   Matera, S. *et al.* Evidence for the Active Phase of Heterogeneous Catalysts through In Situ Reaction Product Imaging and Multiscale Modeling. *ACS Catal* **5**, 4514–4518 (2015).

193.   Huang, X. *et al.* Phase Coexistence and Structural Dynamics of Redox Metal Catalysts Revealed by Operando TEM. *Advanced Materials* **33**, 2101772 (2021).

194.   Jiang, D. *et al.* Dynamic and reversible transformations of subnanometre-sized palladium on ceria for efficient methane removal. *Nat Catal* **6**, 618–627 (2023).

195.   Michaelides, A., Bocquet, M.-L., Sautet, P., Alavi, A. & King, D. A. Structures and thermodynamic phase transitions for oxygen and silver oxide phases on Ag{1 1 1}. *Chem Phys Lett* **367**, 344–350 (2003).

196.   Gustafson, J. *et al.* Self-limited growth of a thin oxide layer on Rh(111). *Phys Rev Lett* **92**, 10–13 (2004).

197.   Miller, D. J. *et al.* Oxidation of Pt(111) under near-ambient conditions. *Phys Rev Lett* **107**, 195502 (2011).

198.   Böttcher, A. & Niehus, H. Oxygen adsorbed on oxidized Ru(0001). *Phys Rev B Condens Matter Mater Phys* **60**, 14396–14404 (1999).

199.   Kühne, T. D. *et al.* CP2K: An electronic structure and molecular dynamics software package -Quickstep: Efficient and accurate electronic structure calculations. *Journal of Chemical Physics* **152**, 194103 (2020).

200.   Hutter, J., Iannuzzi, M., Schiffmann, F. & Vandevondele, J. Cp2k: Atomistic simulations of condensed matter systems. *Wiley Interdiscip Rev Comput Mol Sci* **4**, 15–25 (2014).

201. Vandevondele, J. *et al.* Quickstep: Fast and accurate density functional calculations using a mixed Gaussian and plane waves approach. *Comput Phys Commun* **167**, 103–128 (2005).

202. VandeVondele, J. & Hutter, J. Gaussian basis sets for accurate calculations on molecular systems in gas and condensed phases. *Journal of Chemical Physics* **127**, 114105 (2007).

203. Hartwigsen, C., Goedecker, S. & Hutter, J. Relativistic separable dual-space Gaussian pseudopotentials from H to Rn. *Phys Rev B* **58**, 3641–3662 (1998).

204. Goedecker, S. & Teter, M. Separable dual-space Gaussian pseudopotentials. *Phys Rev B Condens Matter Mater Phys* **54**, 1703–1710 (1996).

205. Krack, M. Pseudopotentials for H to Kr optimized for gradient-corrected exchange-correlation functionals. *Theor Chem Acc* **114**, 145–152 (2005).

206. Perdew, J. P., Burke, K. & Ernzerhof, M. Generalized Gradient Approximation Made Simple. *Phys Rev Lett* **78**, 1396–1396 (1997).

207. Becke, A. D. Density-functional thermochemistry. III. The role of exact exchange. *J Chem Phys* **98**, 5648–5652 (1993).

208. Grimme, S., Ehrlich, S. & Goerigk, L. Effect of the damping function in dispersion corrected density functional theory. *J Comput Chem* **32**, 1456–1465 (2011).

209. Grimme, S., Antony, J., Ehrlich, S. & Krieg, H. A consistent and accurate ab initio parametrization of density functional dispersion correction (DFT-D) for the 94 elements H-Pu. *Journal of Chemical Physics* **132**, 154104 (2010).

210. Grimme, S., Antony, J., Schwabe, T. & Mück-Lichtenfeld, C. Density functional theory with dispersion corrections for supramolecular structures, aggregates, and complexes of (bio)organic molecules. *Org Biomol Chem* **5**, 741–758 (2007).

211. Todorova, M. *et al.* Role of Subsurface Oxygen in Oxide Formation at Transition Metal Surfaces. *Phys Rev Lett* **89**, 96103 (2002).

212. Zhang, X., Zheng, P., Ma, Y., Jiang, Y. & Li, H. Atomic-scale understanding of oxidation mechanisms of materials by computational approaches: A review. *Mater Des* **217**, 110605 (2022).

213. Samal, S. *Discussion on the Mechanism of High-temperature Oxidation*. *High-Temperature Oxidation of Metals* (2016).

214. Hussey, R. J., Mitchell, D. F. & Graham, M. J. The growth and structure of oxide films formed on single crystal (100) and polycrystalline Cr between 550 and 900 °C. *Materials and Corrosion* **38**, 575–583 (1987).

215. Hussey, R. J., Caplan, D. & Graham, M. J. The growth and structure of oxide films on Fe. II. Oxidation of polycrystalline Fe at 240-320°C. *Oxidation of Metals* **15**, 421–435 (1981).

216. Payne, B. P., Grosvenor, Andrew. P., Biesinger, M. C., Kobe, B. A. & McIntyre, N. S. Structure and growth of oxides on polycrystalline nickel surfaces. *Surface and Interface Analysis* **39**, 582–592 (2007).

217. Shard, A. G. A straightforward method for interpreting XPS data from core-shell nanoparticles. *Journal of Physical Chemistry C* **116**, 16806–16813 (2012).

218. Lin, H., Lin, H., Liu, J. X., Fan, H. & Li, W. X. Compensation between Surface Energy and hcp/fcc Phase Energy of Late Transition Metals from First-Principles Calculations. *Journal of Physical Chemistry C* **124**, 11005–11014 (2020).

219. Rao, R. R. *et al.* Surface Orientation Dependent Water Dissociation on Rutile Ruthenium Dioxide. *Journal of Physical Chemistry C* **122**, 17802–17811 (2018).

220. Thiel, P. A. & Madey, T. E. The interaction of water with solid surfaces: Fundamental aspects. *Surf Sci Rep* **7**, 211–385 (1987).

221. Henderson, M. The interaction of water with solid surfaces: fundamental aspects revisited. *Surf Sci Rep* **46**, 1–308 (2002).

222. Pujilaksono, B., Jonsson, T., Halvarsson, M., Svensson, J. E. & Johansson, L. G. Oxidation of iron at 400-600 °C in dry and wet O_2. *Corros Sci* **52**, 1560–1569 (2010).

223. Liu, Q., Tong, X. & Zhou, G. H_2O Dissociation-Induced Aluminum Oxide Growth on Oxidized Al(111) Surfaces. *Langmuir* **31**, 13117–13126 (2015).

224. Mitchell, W. J., Chung, C. H., Yi, S. I., Hu, E. L. & Weinberg, W. H. Oxidation of AlAs films under ultrahigh vacuum conditions: Interaction of H_2O and O_2 with the AlAs(001) surface. *Surf Sci* **384**, 81–93 (1997).

225. Opila, E. J. Variation of the oxidation rate of silicon carbide with water-vapor pressure. *Journal of the American Ceramic Society* **82**, 625–636 (1999).

226. Tatarkhanov, M. *et al.* The structure of mixed H_2O-OH monolayer films on Ru(0001). *Journal of Chemical Physics* **129**, 154109 (2008).

227. Thiel, P. A., DePaola, R. A. & Hoffmann, F. M. The vibrational spectra of chemisorbed molecular clusters: H_2O on Ru(001). *J Chem Phys* **80**, 5326–5331 (1984).

228. Pirug, G., Ritke, C. & Bonzel, H. P. Adsorption of H_2O on Ru(001). *Surf Sci* **241**, 289–301 (1991).

229. Kim, Y., Moon, E. S., Shin, S. & Kang, H. Acidic water monolayer on ruthenium(0001). *Angewandte Chemie - International Edition* **51**, 12806–12809 (2012).

230. Michaelides, A., Alavi, A. & King, D. A. Different surface chemistries of water on Ru{0001}: From monomer adsorption to partially dissociated bilayers. *J Am Chem Soc* **125**, 2746–2755 (2003).

231. Zhao, P. *et al.* Adsorption and dissociation of H_2O and CO_2 on the clean and O-pre-covered Ru(0001) surface. *Appl Catal A Gen* **540**, 31–36 (2017).

232. Maier, S., Stass, I., Cerdá, J. I. & Salmeron, M. Unveiling the mechanism of water partial dissociation on Ru(0001). *Phys Rev Lett* **112**, 1–5 (2013).

233. Weissenrieder, J., Mikkelsen, A., Andersen, J. N., Feibelman, P. J. & Held, G. Experimental evidence for a partially dissociated water bilayer on Ru{0001}. *Phys Rev Lett* **93**, 3–6 (2004).

234. Andersson, K., Nikitin, A., Pettersson, L. G. M., Nilsson, A. & Ogasawara, H. Water dissociation on Ru(001): An activated process. *Phys Rev Lett* **93**, 196101 (2004).

235. Liu, F., Sturm, J. M., Lee, C. J. & Bijkerk, F. Extreme UV induced dissociation of amorphous solid water and crystalline water bilayers on Ru(0001). *Surf Sci* **646**, 101–107 (2016).

236. Sun, Q., Reuter, K. & Scheffler, M. Effect of a humid environment on the surface structure of RuO_2(110). *Phys Rev B Condens Matter Mater Phys* **67**, 205424 (2003).

237. Heras-Domingo, J., Sodupe, M. & Solans-Monfort, X. Interaction between Ruthenium Oxide Surfaces and Water Molecules. Effect of Surface Morphology and Water Coverage. *Journal of Physical Chemistry C* **123**, 7786–7798 (2019).

238.   González, D. *et al.* Water Adsorption on MO_2 (M = Ti, Ru, and Ir) Surfaces. Importance of Octahedral Distortion and Cooperative Effects. *ACS Omega* **4**, 2989–2999 (2019).

239.   Mu, R. *et al.* Dimerization induced deprotonation of water on RuO_2(110). *Journal of Physical Chemistry Letters* **5**, 3445–3450 (2014).

240.   Lobo, A. & Conrad, H. Interaction of H_2O with the RuO_2(1 1 0) surface studied by HREELS and TDS. *Surf Sci* **523**, 279–286 (2003).

241.   Nguyen, M. T. *et al.* Dynamics, Stability, and Adsorption States of Water on Oxidized RuO_2(110). *Journal of Physical Chemistry C* **121**, 18505–18515 (2017).

242.   Müller, R., Yulin, S., Naujok, P., Kaiser, N. & Tünnermann, A. Optical properties and oxidation resistance of different transition metals for soft X-ray and EUV applications. *Thin Solid Films* **624**, 1–6 (2017).

243.   Over, H. & Seitsonen, A. P. Oxidation of Metal Surfaces. *Science's Compass* **297**, 2003–2005 (2003).

244.   Morgan, D. J. XPS insights: Sample degradation in X-ray photoelectron spectroscopy. *Surface and Interface Analysis* **55**, 331–335 (2023).

245.   Maksyutenko, P., Rizzo, T. R. & Boyarkin, O. V. A direct measurement of the dissociation energy of water. *Journal of Chemical Physics* **125**, 4–7 (2006).

246.   Ugur, D., Storm, A. J., Verberk, R., Brouwer, J. C. & Sloof, W. G. Kinetics of reduction of a RuO_2(110) film on Ru(0001) by H_2. *Journal of Physical Chemistry C* **116**, 26822–26828 (2012).

Summary

In this thesis, the surface chemistry of ruthenium is investigated to understand its chemical reactions with silicon, oxygen, and water. CHAPTER 1 establishes the context for the research and its motivation in nanolithography technology, followed by an introduction on the basics of metal oxidation. It is made clear that even seemingly simple reactions like oxidation are not single-step processes but involve a sequence of individual steps from the reactants to the final product. The complementary role of thermodynamics, indicating whether a product is favorable to form, and kinetics, determining the reaction rates of the individual steps, are outlined and connected to metal oxidation. Depending on the reaction conditions the oxidation of a metal can have different rate-limiting steps and growth kinetics. For the thin oxide layers studied in this thesis, the model by Cabrera and Mott is applicable, describing growth based on ion diffusion driven by an electric field created inside the layer. This model is discussed in the context of the oxidation of the element of choice for this thesis, ruthenium, which oxidizes via a thin intermediate oxide to ruthenium dioxide of a rutile crystal structure.

Experimentally following the evolution of surfaces during chemical reactions requires surface-sensitive measurement techniques. The method at the core of this thesis, X-ray photoelectron spectroscopy (XPS), is introduced in detail in CHAPTER 2. This technique is based on the photoelectric effect, the emission of electrons from a material upon irradiation with light of sufficient energy. The kinetic energy of the resulting photoelectrons is characteristic for the emitting element and its oxidation state. Electrons in the typical energy range for XPS interact strongly with matter and typically scatter and lose all relevant information if they travel through the solid for more than a few nanometers. Specific XPS setups designed for operation at near-ambient pressures allow for measurements during gas exposures, providing insight into reaction kinetics.

The challenges of peak fitting to identify phases with similar XPS spectra are the starting point of the study on Ru silicides in CHAPTER 3. The binding energy shift between metal and silicide is small in the case of Ru, making it challenging to distinguish the two species by their peak position. In this chapter, an electron energy loss feature caused by the excitation of plasmons in the solid is identified as clear indicator of silicide formation in the Ru-Si system. The deposition of thin layers with different Ru:Si ratios allowed for the observation of a gradual shift of these plasmon loss features. Confirming the crystal structure with X-ray diffraction, the peak positions of the plasmon loss features were attributed to different $RuSi_x$ phases.

The interaction of single crystal ruthenium with oxygen and the formation of the initial layers of ruthenium oxide is investigated in CHAPTER 4. NAP-XPS experiments provide time-resolved information on ruthenium oxidation and help identify a two-step oxidation process limited by kinetics in the first nanometer of oxide growth. Experiments varying the surface roughness and the oxygen pressure give indications that defects and the stoichiometry of the layer both play an important role in this peculiar growth. Density functional theory calculations provide evidence that ruthenium vacancies are the predominant defect in the initial oxide layer, influencing this two-step oxidation process.

The understanding gained in the simple model system of single crystalline ruthenium in pure oxygen environment is taken to a next level in CHAPTER 5, which connects it to more complex and less frequently studied aspects of oxidation. This part of the thesis termed "advanced oxidation" encompasses the role of plasmon features in the interpretation of Ru XPS spectra, oxidation of polycrystalline Ru layers, and the oxidation of Ru single crystals by water exposure. The first subsection shows that surface plasmon loss features are present at the high-binding-energy end of the typical scan range of the characteristic Ru 3d region, complicating peak fitting. These plasmon loss features change the background intensity of the spectrum, leading to an incorrect estimate of the peak asymmetry and thus a different measured peak area of ruthenium. The second subsection establishes a connection between model studies on single crystals and thin-film applications, where typically polycrystalline layers are employed. The polycrystalline ruthenium shows a two-step oxidation processes similar to the one observed for single crystals in CHAPTER 4 at a similar threshold thickness. The final subchapter is devoted to the interaction of ruthenium and its oxides with water, a common contaminant in vacuum chambers and reactors in industrial applications. In the presence of water vapor a thin oxide layer grows on Ru metal at elevated temperatures during *in situ* XPS measurements, whereas no oxidation is observed without X-ray irradiation. During water exposures of pre-grown oxide layers of sub-nanometer thickness, a slight reduction in oxide content is identified, likely originating from an increased hydrogen gas background pressure during the water exposures. Slightly thicker oxide layers of a few nanometers appear to not oxidize or reduce during thermal exposure to water at the same conditions.

In conclusion, this thesis contributes to the understanding of surface chemistry of ruthenium. *In situ* studies and detailed analysis of the spectral features in XPS provide new insights on the formation of compounds with silicon and on the intricacies of oxide growth at ruthenium surfaces that have been thoroughly studied over decades. Moreover, the fundamental insights on the evolution of ruthenium surfaces close to realistic conditions can lead to improvements of their performance and lifetime in industrial applications.

Samenvatting

In dit proefschrift wordt de oppervlakte chemie van ruthenium met silicium, zuurstof, en water onderzocht om de chemische reacties te begrijpen. In HOOFDSTUK 1 wordt de context van het onderzoek en de motivatie voor de nanolithografie technologie behandeld. Dit wordt gevolgd door een introductie over de basisconcepten over metaaloxidatie. Deze oxidatie is geen enkele reactie, maar bestaat uit meerdere individuele stappen om de uiteindelijke oxide te vormen. De complementaire rol van thermodynamica, die aangeeft of een product gunstig is om te vormen, en reactiekinetiek, die de reactiesnelheden van afzonderlijke stappen bepaald, worden geschetst en verbonden met metaaloxidatie. Afhankelijk van de reactieomstandigheden kan de oxidatie van een metaal verschillende reactiesnelheid beperkende stappen en groeikinetiek hebben. Voor de dunne oxide lagen die in dit proefschrift worden bestudeerd is het Cabrera-Mott model van toepassing. Het CM model beschrijft de groei van een oxide laag op de basis van een veld geïnduceerde ion diffusie. Dit model wordt besproken in de context van de oxidatie van ruthenium, en hoe ruthenium oxideert via een dunne intermediaire oxidelaag naar de uiteindelijke rutheniumdioxide met een rutiel kristalstructuur.

De oppervlakte reacties tijdens chemische reacties experimenteel volgen vereist oppervlakte gevoelige meet technieken. De voornaamst toegepaste methode in dit proefschrift is rontgen foto-elektron spectroscopy (XPS), en wordt in detail geïntroduceerd in HOOFDSTUK 2. Deze techniek is gebaseerd op het foto-elektrische effect, waar de emissie van de foto-elektron uit een materiaal komen tijdens de excitatie door fotonen van hoog genoege energie. De kinetische energie van de ontstane foto-elektronen is karakteristiek van het element en de oxidatietoestand van het beschenen materiaal. De elektronen in het typische energiebereik van deze techniek interacteren sterk met materie, waardoor deze verstrooien en dus de relevante informatie verliezen wanneer ze door enkele nanometers materiaal gaan. De XPS die is gebruikt in dit proefschrift is ontwikkeld om te kunnen meten in gasdrukken die de druk benaderen van tijdens chemische reacties. Hiermee kan inzicht verkregen worden over de individuele reacties.

De uitdagingen van piek identificatie van verschillende fasen met vergelijkbare XPS spectra is het startpunt voor het onderzoek naar Ru silicides in HOOFDSTUK 3. Het bindingsenergie verschil tussen ruthenium metaal en silicide is klein, en maakt het zeer uitdagend om deze te differentiëren gebaseerd op hun piek posities. In dit hoofdstuk de elektron energieverlies eigenschap, welke veroorzaakt wordt door de excitatie van een plasmon in het materiaal, gebruikt als een duidelijke indicator van silicide vorming het Ru-Si systeem. Door dunne lagen van verschillende verhouding

Ru:Si te meten, is een geleidelijke verschuiving van deze plasmon verlies eigenschap te identificeren. De kristalstructuur is geverifieerd met röntgendiffractie, waar de piek posities van de plasmon verlies eigenschappen zijn geverifieerd met de verschillende RuSix fasen.

De interactie van een mono kristal ruthenium met zuurstof en de formatie van de eerste lagen ruthenium oxide is onderzocht in HOOFDSTUK 4. Met behulp van NAP-XPS experimenten is tijdsafhankelijke informatie naar de oxidatie van ruthenium mogelijk gemaakt. Deze informatie is ondersteunend naar het identificeren van de twee staps oxidatieproces, waarin een kinetische limiet zit in de eerste paar nanometer van de oxide groei. In de experimenten met veranderde oppervlakteruwheid en veranderde zuurstofdruk gaf indicatie dat materiaal defecten en de stoichiometrie van de oppervlakte lagen een belangrijke rol zijn voor deze oxide groei. Met behulp van simulaties en theorie, is er extra bewijs en indicaties dat ruthenium defecten een belangrijk effect zijn voor de eerste laag oxide, en specifiek voor de twee staps oxidatie.

Met het verkregen begrip van het simpele model systeem mono kristallijn ruthenium met puur zuurstof, wordt er in HOOFDSTUK 5 gekeken naar complexere omstandigheden die minder vaak worden onderzocht. Dit gedeelte van de thesis is "geavanceerde oxidatie" genoemd en bevat de volgende aspecten, hoe plasmon eigenschappen invloed hebben op Ru XPS spectra, de oxidatie van polykristallijn ruthenium lagen, en de reactie van mono kristallijn ruthenium met water in zijn gasvorm. De eerste subsectie laat zien dat er een oppervlakte plasmon piek aanwezig is in de hoge energie kant van het typische meetbereik voor Ru 3d, wat de piek identificatie en bepaling gecompliceerd. Deze plasmon piek beïnvloed het achtergrondsignaal, wat kan resulteren in een incorrecte asymmetrie van de ruthenium pieken gevolgd door een verandering in totaal oppervlak van de rutheniumpiek. De tweede subsectie gaat over de connectie tussen model studies van monokristallijn ruthenium en dunne-laag applicaties. In deze applicaties worden vaak polykristallijne lagen gebruikt. Ook voor polykristallijn ruthenium is een twee staps oxidatieproces gezien, welke vergelijkbaar is met het monokristallijn ruthenium dat gezien is in HOOFDSTUK 4. Eenzelfde dikte voor deze twee staps reacties is gezien in beide gevallen. De laatste subsectie gaat over de interactie van ruthenium en zijn oxides met water. Water is een algemene verontreiniging in vacuümkamers en reactoren in industriële toepassingen. Tijdens het blootstellen van gasvormig water aan ruthenium groeit er een dunne laag oxide bij verhoogde temperatuur tijdens de XPS metingen. Als datzelfde experiment zonder röntgenstraling wordt gedaan, vormde er geen oxide laag. Tijdens de blootstelling van water aan vooraf gegroeide ruthenium oxides van onder de nanometer dik, werd er een kleine reductie van de hoeveelheid oxide gemeten. Deze reductie kan

mogelijk veroorzaakt zijn door de verhoogde waterstof achtergrond gas tijdens de water blootstellingen. Een dikkere oxide laag van enkele nanometers lijkt verder niet te oxideren of reduceren tijdens de blootstelling aan gasvormig water onder dezelfde omstandigheden.

Metingen tijdens reacties, en gedetailleerde analyse van de spectroscopische eigenschappen van XPS grafieken geven nieuwe inzichten in de formatie van componenten met silicium en de ingewikkeldheden van oxide groei op ruthenium oppervlakken die afgelopen decennia nauwkeurig zijn onderzocht. Bovendien zijn er fundamentele inzichten over de reacties op ruthenium oppervlakken dicht bij realistische eigenschappen onderzocht, welke tot verbeteringen in de toepassing en levensduur in industriële toepassingen kan zorgen.

Acknowledgements

The journey to achieve a PhD has been a long one. Every step along my way through the different educations, it was every time uncertain if the next step would be achievable. Through support of the people around me, fellow students, colleagues, friends, and family, this thesis has been made possible. With all the support of these people at various stages of my life, this thesis has been made possible, thank you.

I would like to thank Roland Bliem for letting me join your group: Materials and Surface Science for EUVL at ARCNL. Thank you for the trust and opportunity that you have given me. The countless discussion and conversations have always been very helpful and constructive to me. And I am very happy that I joined your group. Without a doubt, I would choose this same path again with the knowledge that I have acquired during my time.

I am very grateful to my promotor, Paul Planken, and all the other members of the committee: Klaasjan van Druten, Emilia Olsson, Fred Brouwer, Marcelo Ackermann, and Daniele Stradi. Thank you for reading and evaluating my thesis and taking time out of your schedules.

Part of my chapters are made possible with the help of collaborators: Alessandro Troglia, Emilia Olsson, Jörg Meyer, Jon Cottom. Alessandro, thank you for the XRD measurements supporting my work to differentiate between the silicides. Emilia, Jörg, and Jon, thank you for the many discussions and the explanations on how DFT works and how it supports my experimental results. I would also like to thank the other projects I have been involved in and collaborated with. Thank you for introducing me your science and the fruitful discussions.

I would like to thank my colleagues during my time in the Materials and Surface Science for EUVL group at ARCNL: Roland Bliem, Alessandro Troglia, Tadé Hogenelst, Ester Pérez Penco, Cristiane Stilhano Vilas Boas, Christoph Morscher, Luka Babic, Jan Verhoeven, Ibrahim El Wakil, Mike van de Poll, Ruben Visser, Arend-Jan van Calcar, and Bartjan Spaanderman. The many hours of discussion, research, experiments, maintenance, and bake-outs are happy memories. The group has always felt as a very friendly and good place to work and grow.

An institute like ARCNL is only possible by the people that are working at it. I would like to thank former ARCNL director Joost Frenken, intitute manager Marjan Fretz, and the present ARCNL director Wim van der Zande for their support. Additionally, Wim, thank you for how you have supported the progression of the thesis after I left ARCNL, I appreciate how you and Roland together kept in contact and kept

motivating me to finish the thesis. Another important group of people at ARCNL/AMOLF are the support staff. Among this are the mechanical, electrical, software, and ICT departments, as well as the AMOLF workshop and Nanolab. Whatever idea I have come up with to improve the setup or had problems with experiments, it has always been very helpful and fruitful to visit these departments. Besides these specific groups I would also like to thank the people at ARCNL, the atmosphere has always been friendly, constructive, and helpful.

The people that have been close to me during my time at ARCNL are also my paranymphs, Alessandro and Ester. Alessandro, thank you for all the good times we have had when we were the two PhD's in Roland his group. The many Fridays spend on maintenance and bakeout were at the time annoying, but looking back it is a good memory of time well spend. Ester, it has been a wonderful journey with you walking along. The many questions you have asked, also resulting in me reflecting how much I actually know, have been very helpful. Thank you both for the good environment around me during me time, as well as all the help you have given me.

To Froukje, thank you for the years you are supporting me during my education and PhD work. Having you next to me has been very helpful and allowed me to push forward.

To the many groups of friends from different hobbies and sports over the years. With all these groups I have always felt supported and allowed me to relax and reset before I started focusing on my research again. Thank you for the time, joy, and conversations you have given me.

Even before I started my PhD, my family has always supported and helped me achieve my goals. During the many years of several studies, I have always felt supported by you. I am grateful to all the opportunities that have been made possible by my father Willem, mother Marjon, brother Remko, and sister Ilonka.

Curriculum Vitae

Stefan Willem Johannes van Vliet

12-02-1992 born in Vinkeveen, the Netherlands

Stefan van Vliet is a scientist working on surface chemistry. His doctoral work at ARCNL in the group of Materials and Surface Science for EUVL explores the surface reactions of ruthenium using near-ambient pressure X-ray photoelectron spectroscopy (NAP-XPS), atomic force microscopy (AFM), and thin-film growth. Besides his doctoral work, he has contributed with his XPS measurements to multiple collaborations leading to joint publications with groups at AMOLF and the UvA. He holds a MSc in Nanomaterials from Utrecht University, a BSc in Organic Chemistry from Hogeschool Utrecht, and MBO in Laboratory Chemistry from ROCMN. On this education path, he has gained experience in the fields of inorganic chemistry, catalysis, and polymer chemistry.

Education

2004-2008	Secondary school
	VLC Vinkeveen, VMBO-T
2008-2012	MBO chemical laboratory analyst
	ROCMN Utrecht
2012-2015	Bachelor of applied science, organic chemistry
	Hogeschool Utrecht
2015-2016	Pre-master Chemistry
	Utrecht University
2016-2019	Master of Science, Nanomaterials
	Utrecht University
2019-2024	PhD student researcher, surface chemistry
	ARCNL
2024-present	Researcher
	XUV optics, University of Twente